TRAJECTORY MEASUREMENT OF COSMIC DUST

by

JIANFENG XIE

B.S., Physics,

University of Science and Technology of China, Hefei, China, 2007

A thesis submitted to the

Faculty of the Graduate School of the

University of Colorado in partial fulfillment

of the requirements for the degree of

Doctor of Philosophy

Department of Physics

2012

This thesis entitled:
Trajectory Measurement of Cosmic Dust
written by Jianfeng Xie
has been approved for the Department of Physics

_____

Mihály Horányi

_____

Zoltan Sternovsky

_____

Sascha Kempf

_____

Tobin Munsat

_____

David Brain

Date_____

The final copy of this thesis has been examined by the signatories, and we find that both the content and the form meet acceptable presentation standards of scholarly work in the above mentioned discipline.

Xie, Jianfeng (Ph.D., Physics)

Trajectory Measurement of Cosmic Dust

Thesis directed by Assistant Professor Zoltan Sternovsky

Cosmic dust is abundant in space and, depending on the source, can represent the primordial building blocks of planetary formation. Over the past decades, dust research has contributed significantly to the understanding of our Solar System and a number of ongoing dynamical and geological processes. The in-situ measurement of dust particle trajectories in space allows the determination of their origin and interaction with space and planetary environments. The Dust Trajectory Sensor (DTS) instrument has been developed for the accurate measurement of the velocity vector and charge of individual cosmic dust particles with sizes down to the submicron range. The DTS works by detecting the induced charges on an array of wire electrodes created from charged dust particles passing by, and reconstructing trajectory from the induced charge signals. This work presents the method of analyzing DTS data and results from a parametric study performed to evaluate the accuracy of the measurements. A laboratory version of the DTS instrument has been constructed and tested with particles in the velocity range of 2–5 km/s using the dust accelerator facility in Heidelberg, Germany. Both the numerical study and the experimental data show that the accuracy of the DTS instrument is better than 1% in speed and 1 degree in trajectory direction. The Electrostatic Lunar Dust Analyzer (ELDA) instrument is a specific application of the DTS concept and designed for the measurement of slow-moving (1–100 m/s) charged dust particles mobilized near the lunar surface. In this case, the mass of each charged dust particle is calculated from the deflection of the trajectory using strong electrostatic fields within the instrument. The full prototype of ELDA has also been constructed and tested in the laboratory. The instrument is tested using particles

with a narrow size distribution. The experimental results and the error analyses show that ELDA can measure the mass of individual particles within a factor of two even for very low signal to noise ratios.

Contents

TABLES

Tables

FIGURES

Figures

1. Introduction

1.1 Cosmic Dust

Various kinds of cosmic dust can be seen by naked eye on Earth, such as zodiacal dust in the ecliptic plane and dense interstellar dust clouds located in the plane of our Galaxy, which causes dark belts across the splendid Milky Way. In ancient times, cosmic dust particles used to be an annoyance to astronomers because they obscure the luminous bodies in the night sky. When the field of infrared astronomy began, dust particles were found to be significant constituents of the Universe and vital components of many astrophysical processes, such as stellar outflows and supernovae. Cosmic dust, or space dust, consists of microscopic solid particles floating in space. Definition of dust particle is very loose, and the size range can be from several molecules (few nm) to several hundred μm. Studying dust origins, motion, chemical composition, and interaction with the space environment helps us to understand the formation and evolution of the solar system and other planetary systems. For example, dust can drive the mass loss that occurs when a star is nearing the end of its life (Salpeter, 1974). These particles are essential parts of the early stages of star formation, and they form planets around other stars. In our own solar system, dust causes the zodiacal light in the ecliptic plane (Leinert *et al*., 1998) and plays a major role in the outer diffuse planetary rings at Jupiter and Saturn (Hamilton and Burns, 1993; Hillier *et al*., 2007), the resonant dust ring with the Earth (Jackson and Zook, 1989), and the overall behavior of comets (Delsemme, 1973). Cosmic dust can be divided into several categories by its astronomical location and dynamics features, such as near-surface and planetary (circumplanetary) dust, interplanetary dust, and interstellar dust. The distinction between different kinds of dust particles is not strict. For example, stream particles originating from a planetary system can be expelled into interplanetary space by electromagnetic forces (Grün *et al*.,

1993; Graps *et al*., 2000). Secondary ejecta dust particles, produced on the surface of an airless body, can go into space at high speed. Dust particles are irregularly shaped with porosity ranging from fluffy to compact. The structure, chemical composition, size, and other properties vary radically between different kinds of dust particles and depend on where the dust is found.

1.1.1 Charging Process and Dust Dynamics

In most space environments, dust particles carry electrostatic charges because of exposure to plasma and UV radiation (Horányi, 1996; Zook *et al*., 1996). The time evolution of the electrical charge Q of a dust grain in a plasma environment is described by the current balance equation:

$$\frac{dQ}{dt} = J_e + J_i + J_{sec} + J_v \,, \qquad (1.1)$$

where J_e and J_i represent the electron and ion collection currents from the ambient plasma while J_{sec} and J_v resent the secondary electron and photoelectron emission currents. The secondary electrons are produced by ionization of the material of the grain by bombardment of other particles, such as ions and electrodes from the plasma. All the currents are affected by the plasma characteristics (composition, density, temperature, and energy distribution) and dust particle properties (size, composition, velocity, and surface roughness, et al.).

For most objects in planetary systems, the gravity of the central body is the dominant force, causing the object to move on Keplerian orbits. For cosmic dust grains of low mass, radiation pressure and electromagnetic forces can be significant or even dominate to their dynamics. The gravitational force is proportional to the mass, or the volume of the dust particle, while force from radiation pressure is proportional to the cross-section, radius squared. The charge on the particle, on the other hand, is proportional to the radius for a fixed surface potential.

The gravitational force, $\boldsymbol{F}_g$, acting on the dust particle with mass m, can be expressed as:

$$\boldsymbol{F}_g = -\sum_i \frac{GM_i m}{R_i^3}\boldsymbol{R}_i \,, \tag{1.2}$$

where G is the gravitational constant, M_i is the mass of the Sun or planet, and the R_i is the distance between the dust particle and M_i. In most situations, we only have to consider the gravity from the Sun or the nearest celestial body.

The force from radiation pressure is due to the reflection, scattering, and absorption of photons. The solar radiation force F_R can be expressed as:

$$F_R = \frac{L}{4\pi R^2 c} A \,, \tag{1.3}$$

where L is the solar luminosity, R is the distance to the Sun, c is the speed of light, and A is the cross-section. The scattering cross-section is a function of the wavelength, shape, and optical properties of the particle. When size of the particle is much greater than the wavelength, scattering cross-section is close to the geometrical cross-section.

The radiation force from the Sun can decelerate the particles and cause them to spiral into the Sun, in which case it is referred to as sporadic meteoroids (Grün and Zook, 1980). This is known as the Poynting-Roberson effect, which is caused by isotropical radiation from the particle in the particle's reference frame. The non-radial component of the radiation pressure force acting on a particle with velocity $\boldsymbol{v}$ is of order of v/c, and can be written as (Burns *et al*., 1979)

$$\boldsymbol{F}_{PR} = F_{PR}[\left(1 - \frac{\boldsymbol{v}\cdot\boldsymbol{R}}{c}\right)\frac{\boldsymbol{R}}{R} - \frac{\boldsymbol{v}}{c}] \,. \tag{1.4}$$

This force is opposite to the velocity vector of the dust, dissipates angular momentum, and causes the dust to spiral inward to the Sun. Micron sized dust particles need a few thousand years to get from 1 AU to the Sun. Some smaller sized particle can be ejected from the Solar system in unbound orbits when the repelling force from the solar radiation is of the same order of magnitude as solar gravity. These dust particles are called β-meteoroids (Grün and Zook, 1980).

The in-situ detection of β-meteoroids was reported for the first time by Berg and Grün (1973), and later by Zook and Berg (1975). These dust particles can be produced from collisions of larger meteoroids as well as from the sublimation of dust particles near the Sun (Mukai, 1985, 1996; Schwehm, 1977). The orbital parameters for the particle depend on the exact conditions at the time of the production. Simulations suggest that dust particles less than 0.5 microns in radius around several AU will be ejected from the Solar system in unbound orbits (Krivov *et al*., 1998).

The electromagnetic force acting on a dust particle with charge q and velocity $\boldsymbol{v}$ is expressed as

$$\boldsymbol{F}_L = q\boldsymbol{v} \times \boldsymbol{B} + \boldsymbol{E}q \ , \qquad (1.5)$$

where $\boldsymbol{B}$ is the magnetic field vector at the location of the dust grain and $\boldsymbol{E}$ is the electric field. In interplanetary space $\boldsymbol{E}$ is usually small and can be ignored (Krivov *et al*., 1998), while strong E field (~ 10 V/ m) can be present near the surfaces of airless bodies (Colwell *et al*., 2007). The magnetic field can be from a planet or the solar wind plasma. The solar wind within the heliosphere carries the spiral shaped Interplanetary Magnetic Field (IMF). The Lorentz force acting on dust particle moving through the IMF will change the semi-major axis and eccentricity of its elliptical orbit, and orbit's inclination to the ecliptic plane (Morfill and Grün, 1979; Wallis and Hassan, 1985). Sub-micron sized dust particles can be accelerated outward from the system by the strong Lorentz force when they reach close (2 AU) to the Sun (Hamilton *et al*., 1996; Mann *et al*., 2004). The dynamics of high speed nanometer-size stream particles in jovian and saturnian system are dominated by the Lorentz force.

The relative importance of these various forces depends on the ambient environment as well as dust particles' properties, which makes the dust dynamics complex. Take the dynamic of the micron-sized particles in Saturn's E ring for example; the gravity, the radiation pressure, and

the electromagnetic force are roughly comparable in magnitude but acting in different directions (Horányi, 1992), which makes the dust particles spread in a wide range.

1.1.2 Near-surface and Planetary Dust

A planetary ring consists of cosmic dust and other blocks orbiting around a planet in a flat disc-shaped region. The most notable planetary rings in the Solar System are those around Saturn. Unlike the other rings of Saturn, the E Ring consists of dust particles instead of macroscopic particles. The E Ring is the widest and outermost ring of Saturn, beginning at the orbit of Mimas and ending somewhere around the orbit of Rhea. The flyby of Cassini also suggested that the saturnian moon Rhea may have its own tenuous ring system, which would make it the only moon known to possess a ring system (Jones *et al*., 2008).

Dust particles can be ejected from underneath of the surface of the celestial bodies by volcanic eruption, as is the case for the plumes of Io. Volcanic activity on Io was discovered in 1979 by Voyager 1 (Morabito *et al*., 1979). Due to Io's low gravity and low atmospheric pressure, dust and gas ejected from volcanic vents rises to great heights (~ 500 km) before falling back to the surface. The plume of Enceladus, moon of Saturn, was also found by Cassini in 2005. Enceladus orbits in the densest part of Saturn's diffuse E ring. The measurement of the particle in E ring by the Cassini cosmic dust analyzer (CDA) in 2004 shows that the particles are predominantly water ice, with minor contributions from possible combinations of silicates, carbon dioxide, ammonia, molecular nitrogen, and hydrocarbons (Hillier *et al*., 2007). This discovery supports the conclusion that Enceladus is the main source of particles for this ring (Spahn *et al*., 2006).

The volcanically active moon Io is the source of 10-nanometer sized planetary stream particles from Jupiter, as discovered by the dust detector on the Ulysses spacecraft in 1992 (Grün

et al., 1993). These particles are leaving the Jovian system as a collimated beam with velocities greater than 100 km/s, and the acceleration is provided by the co-rotating electric field of the jovian magnetosphere (Graps *et al*., 2000). Stream particles in saturnian systems was predicted by Horányi (2000) based on the plasma model derived from the Voyager data. This prediction was confirmed by the discovery of saturnian stream particles during Cassini's Saturn approach in 2004 (Kempf *et al*., 2005).

1.1.3 Lunar Dust

The continuous bombardments of micrometeoroids create secondary ejecta dust particles on the airless bodies. A dust cloud around Ganymede, a moon of Jupiter, was detected in-situ by the detector onboard the Galileo spacecraft (Krüger *et al*., 1999, 2000, 2003). Tenuous dust clouds at other Galilean moons, Europa, and Callisto were also detected (Krüger *et al*., 2003). On the other hand, all airless bodies are directly exposed to both solar radiation and ambient plasmas. Dust grains can interact with the local plasma environment and transport on the body surface.

The same processes also happen on the Moon (Grün *et al*., 2011). The understanding of dust mobilization is of great engineering importance for future lunar missions as lunar fines pose a hazard to both equipment and astronauts. The continual bombardment of the lunar surface by micrometeoroids can release dust particles from the surface (Hoffmann *et al*., 1975; Allison and McDonnell, 1981; Zook *et al*., 1984) and may produce dust clouds. However, ejecta clouds around the Moon have not been observed yet due to the lack of dust detectors on past missions or insufficient sensitivity. The Lunar Dust EXperiment (LDEX) instrument is scheduled for launch onboard the Lunar Atmosphere and Dust Environment Explorer (LADEE) mission in 2013 (Horányi *et al*., 2009). LADEE will characterize the Moon's dust environment from orbit with

occasional dips down to 30 km altitude. The LDEX instrument is designed for high sensitivity and is capable of detecting sub-micron-sized dust particles from obit.

The possibility of the electrostatic lofting, levitation, and transport of lunar dust has been indicated from the observations of the lunar horizon glow (Figure 1.1) by the Surveyor landers (McCoy and Criswell, 1974; McCoy, 1976; Zook and McCoy, 1991) and the dust events recorded near sunrise and sunset by the Lunar Ejecta And Meteorites (LEAM) instrument left behind by Apollo 17 (Berg *et al*., 1973, 1974). Photoelectron and plasma sheaths formed above the lunar surface and the dust dynamics in the sheaths were theoretically studied and simulated (Nitter and Havnes, 1992; Nitter *et al*., 1998; Colwell *et al*., 2009; Poppe and Horányi, 2010; Poppe *et al*., 2011). These studies showed that micron-sized dust particles can be levitated to as high as several meters, depending on the size and plasma parameters. An analytical model of dust launching on the Moon and asteroid surfaces was recently developed by taking into account cohesive forces between dust particles (Hartzell and Scheeres, 2011). The model showed that the electric field strength required for dust particle launching was dominated by the cohesive force for micron-sized dust particles. Laboratory experiments have been also conducted to investigate the physics of electrostatic dust transport on the lunar surface. Charged dust particles were levitated in a plasma sheath due to the electrostatic force balancing the gravitational force (Sickafoose *et al*., 2002). Dust grains were also released from surfaces exposed to plasma in the presence of an electron beam (Sheridan *et al*., 1992; Flanagan and Goree, 2006). Dust transport on various surfaces in plasma were demonstrated and studied, including: a) the dust spreading and hopping on a surface that repels electrons and collects ions (Wang *et al*., 2009, 2011a), b) the dust transport as a consequence of differential charging on surfaces that have different secondary electron yields (Wang *et al*., 2010), and c) the dust movement near the topography-

induced electron beam impact/shadow boundaries (Wang *et al*., 2011b). In spite of the progress made in both theory and experiment, the charging of dust grains and their subsequent mobilization and transport on the lunar surface still remain elusive.

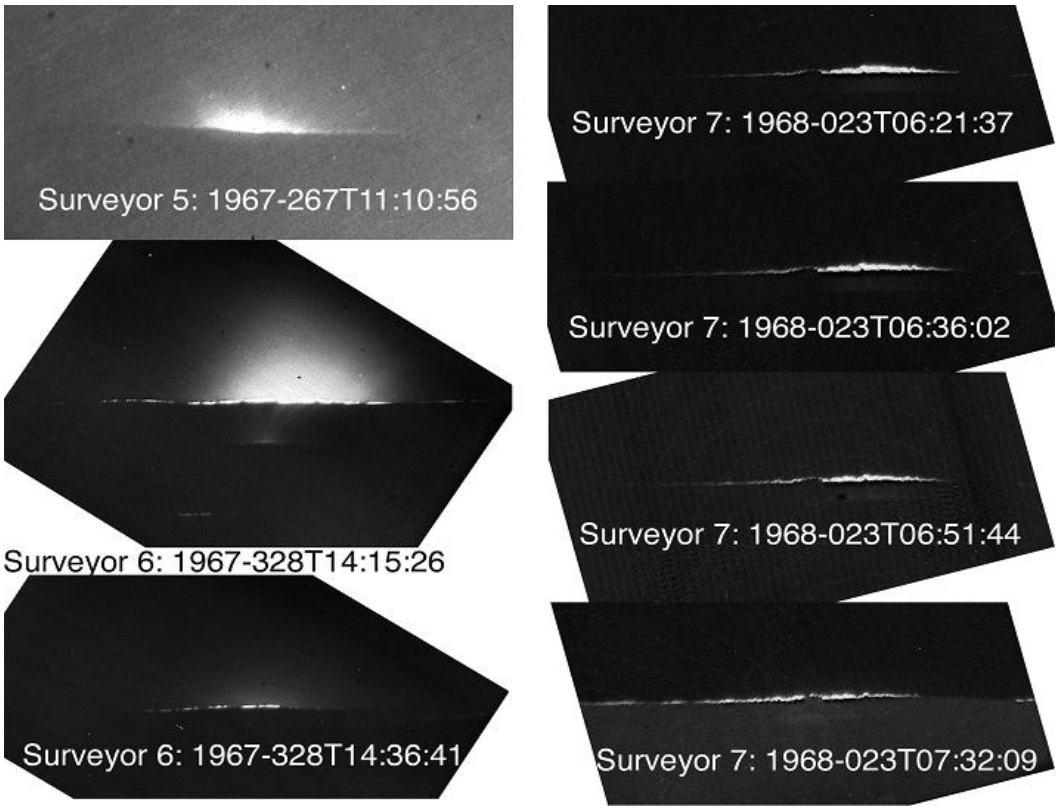

Figure 1.1: Surveyor horizon glow images taken by Surveyor landers (NASA photos). The horizon glow is interpreted as forward-scattered sunlight from a cloud of levitated dust particles above the surface near the terminator.

Regardless of the release mechanism (ejecta particles or electrostatic lofting), only a small fraction of the particles will reach high altitudes to be detected by instruments on orbit, e.g. LDEX on LADEE. Most of the particles released by micrometeoroid impacts have a velocity below 100 m/s (Krüger *et al*., 2000), which corresponds to an altitude of 3 km (310 m/s to 30 km). In simplistic models for electrostatic lofting, unrealistically large charge on the dust and

surface potentials are needed to elevate dust particles to high altitude. Therefore, it is necessary to detect and analyze dust particles on or near the surface.

1.1.4 Interplanetary Dust Particles (IDPs)

Interplanetary dust particles (IDPs) pervade the space between planets in the solar system and in other planetary systems. Their nature, origin, dynamics, and the relationship to larger bodies have been studied for many years to better understand our solar system. The sources of IDPs include at least: comet dust, asteroid collisions, dust from Kuiper Belt, and interstellar medium passing through our solar system (Mann *et al*., 2010). The main mechanisms for destruction of interplanetary dust particles include: expulsion by radiation pressure, Poynting-Robertson (PR) radiation drag inducing drift toward the Sun, electromagnetic effects from the solar wind, mutual collisions, sublimation, and the dynamical effects of planets (Figure 1.2). The average density of stratospherically-captured IDPs is about 2.0 g/cm^3 and most of them are in a range 1-3 g/cm^3 (Love *et al*., 1994).

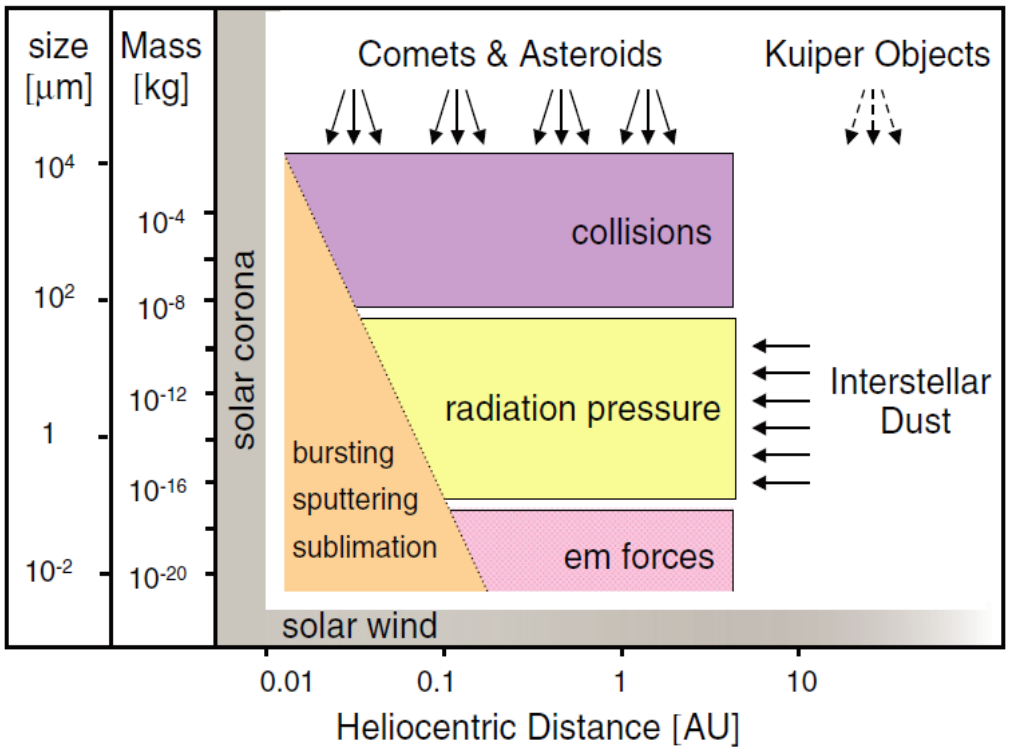

Figure 1.2: Sources and sinks of the solar system dust cloud. The interplanetary dust comes from comet dust, collisions of the asteroids, dust from Kuiper objects, and also interstellar dust. They are affected by gravity, radiation pressure, solar wind, and electromagnetic force. Interplanetary dust can be destroyed by bursting, sputtering, and sublimation (from Mann *et al*., 2010).

The presence of IDPs in the inner solar system is exhibited through the zodiacal light. The zodiacal light is a faint diffuse white glow seen in the night sky that extends up from vicinity of the Sun along the ecliptic, which is caused by scattering sunlight by the interplanetary dust in tenuous disk (zodiacal cloud) orbiting within the inner part of the solar system (Leinert *et al*., 1998). The zodiacal cloud extends out to about 5 AU and these dust particles are between 10 and 300 microns in diameter, with most mass around 150 microns (Bernhard and Birger, 2001). The lifetimes of particles in the zodiacal cloud are determined by the Poynting-Robertson effect rather than by mutual collisions. The zodiacal light decreases in intensity with distance from the Sun which may be roughly explained by the inward migration due to this effect. The

lifetimes of these dust particles are very short compared to the lifetime of the Solar System. Therefore, the grains would be "later-generation" dust and all primordial grains from the Solar system's formation were removed long ago. The zodiacal cloud is fed erratically by the disintegration of comets close to the Sun, and by dust from collisions in the asteroid belt.

1.1.5 Interstellar Dust (ISD)

Interstellar dust presents in the space between the star systems in a galaxy. It obscures the stars, which makes regions in the Milky Way appear dark from Earth. The obscuration tends to be greater at shorter wavelengths because of Rayleigh scattering; thus, the obscured stars look "reddened". Interstellar dust, containing no more than one or two percent of the mass of the interstellar medium (ISM), has a dramatic effect upon the physical conditions and processes taking place within the Universe. Interstellar dust reradiates the absorbed energy in the far-infrared (FIR) part of the spectrum. The FIR radiation from dust removes the gravitational energy of collapsing clouds, allowing star formation to occur (Ciolek, 1995). Study of these grains will help understand the creation and evolution of the stars. The sources of interstellar dust include at least: dying stars, supernova, and collisions of the astronomical bodies (Wang, 1991). Explosions, evaporation, sputtering, and grain-grain collisions are destroying mechanisms, which also have a major influence on the grain size distribution.

The local interstellar medium surrounding the solar system includes a component of interstellar dust (Holzer, 1989). Interstellar dust particles originating from the Local Interstellar Cloud (LIC) move on hyperbolic trajectories through the solar system. Interstellar dust in solar system was first discovered by dust detectors on the Ulysses spacecraft in 1992 (Grün *et al.*, 1993) and later confirmed by the Galileo mission (Baguhl *et al.*, 1995; Altobelli *et al.*, 2005). These dust particles in the inner solar system have been identified as a stream from a direction of

252 ° and 2.5 ° ecliptic longitude and latitude, respectively. Ulysses detected particles in the interstellar dust stream with size up to 1 μm at high ecliptic latitudes between 3 and 5 AU. On average, their impact velocities exceed the local solar system escape velocity, even if radiation pressure effects are neglected (Grün *et al*., 1994). The grains were found to have a speed of 26 km/s. (Baguhl *et al*., 1995; Witte *et al*., 1996; Frisch *et al*., 1999). Interstellar dust is ubiquitous in the solar system: dust measurements between 0.3 and 3 AU in the ecliptic plane exist also from Helios, Galileo, and Cassini. However, its density is very low. In-situ measurements indicate that interstellar dust surface density is only of order 0.1% of interplanetary dust density at 1 AU (Grogan *et al*., 1996).

The dynamics of the interstellar dust in the solar system is very complicated. The distance-dependent alteration of the interstellar dust stream were caused by radiation pressure, gravitational focusing, and electromagnetic interaction with the time-varying interplanetary magnetic field which also depends on grain size (Altobelli *et al*., 2003; Altobelli *et al*., 2005; Mann and Kimura, 2000; Landgraf, 2000; Czechowski and Mann, 2003). As a result, the size distribution and fluxes of grains measured inside the heliosphere are strongly modified (Landgraf *et al*. 1999; Landgraf *et al*., 2003).

1.2 Observations and Instruments

1.2.1 Remote Observations

Dust in space can be studied via remote sensing or in-situ measurements, and laboratory analysis are only available for collected dust particles. Remote observations measure the electromagnetic radiation scatted or emitted by the dust particles. The observation of zodiacal light provides information on properties of dust particles averaged over many particles and long distances. These properties include spatial distribution, number density, size, structure, and

material. Most of these observations are made from the Earth and others are achieved in space by detectors on satellites or spacecraft.

1.2.2 Sample Collection

An average of 40 tons per day of interplanetary dust falls into the Earth atmosphere (Leinert and Grün, 1990). The modern era of laboratory study of these particles began with the stratospheric collection flights in the 1970s using balloons and then aircraft. High-flying aircraft collect cosmic dust particles of size range from 5 to 50 microns in the stratosphere. Cosmic dust particle residues are also collected from Antarctic ice and Greenland ice samples as well as from the ocean floor. These stratospheric and polar ice melt interplanetary dust particles are then examined in the laboratory and have typically size of 20 microns to 1 mm (Maurette *et al*., 1991; Kurat *et al*., 1994).

The Stardust mission was a dedicated space mission to capture cometary dust particles and return them back to the Earth (Brownlee *et al*., 2003). The particles were captured using a low-density, inert, micro porous aerogel as the spacecraft passed through the coma of comet Wild 2. After sample collection was complete, the collector receded into the Sample Return Capsule and was dropped into the Earth's atmosphere. It also captured samples of interstellar dust travelling in our solar system. The interstellar dust detected by Ulysses and Galileo spacecrafts is general less than 1 μm and are very difficult to collect at Earth by current techniques.

1.2.3 In-situ Measurement

For in-situ measurement, dust detectors have to be on board spacecraft flown to various planetary systems or in interplanetary space. Depending on the properties (size, speed, and charge) of the dust particles and ambient environment, different methods are employed for dust

measurements, like the penetration detector on Pioneer 11(Humes *et al*., 1980), optical detection (Colangeli *et al*., 2007), acoustic signal used in BepiColombo mission (Takechi *et al*., 2009), momentum transfer, and impact ionization (Auer and Sitte, 1968). Interplanetary dust particles can be collected in the stratosphere and intact star dust particles can be captured by low density silica aerogel and sent back by spacecraft (Zolensky *et al*., 1994). Figure 1.3 shows the applicable size/mass range for different detection methods for near earth dust particles.

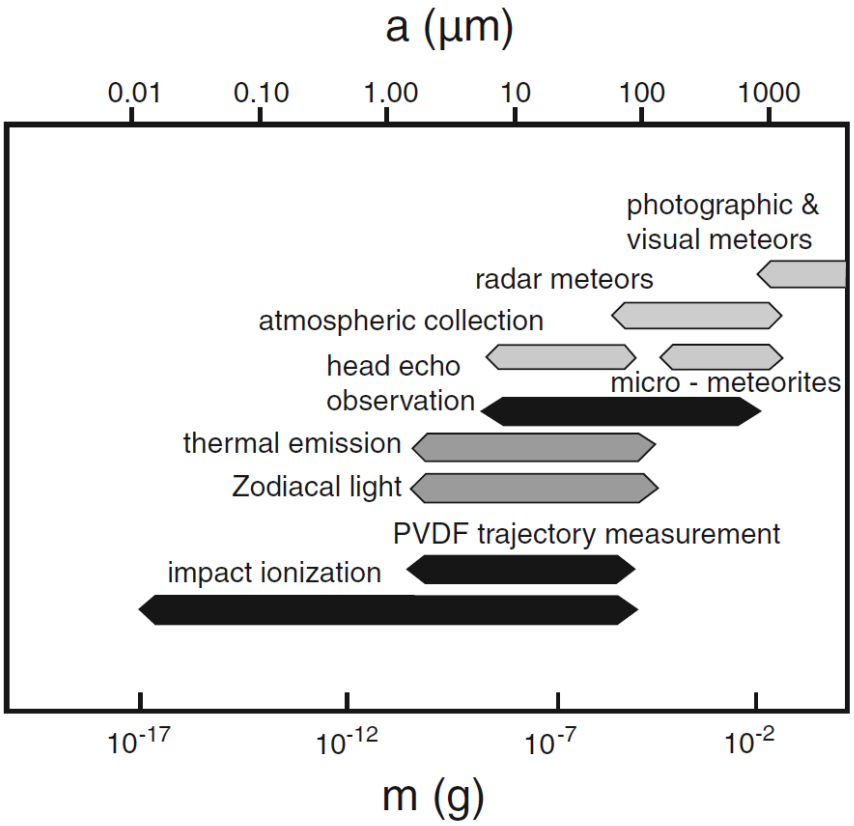

Figure 1.3: Detection methods of dust near earth and the applicable size/mass range. Different methods provide different information. The detection methods denoted as dark provide orbital information, while those denoted as grey bars provide brightness information integrated along the line of sight. The light grey bars denote detection of single particles or events where the orbital information is not clear (from Mann *et al*., 2006).

Most instruments on board spacecraft make use of the high speed of the dust particles. The Helios spacecraft measured the interplanetary dust near the ecliptic from 1 AU to 0.3 AU. Several spacecraft (Pioneer 8/9, HEOS 2, Hiten) measured the dust with size down to 0.3 μm (HEOS 2) near 1 AU. Ulysses measured an average flux of 1.5×10^{-4} m^{-2} s^{-1} at distance from 1.7 AU to 5 AU (Grün *et al*., 1994). Among these dust particles, half of them had impact speeds corresponding to hyperbolic orbits (β-meteoroids). For dust particles with heliocentric distance > 5 AU, measurements were made by Pioneer 10 and 11, which even detected dust particles up to 18 AU (Humes, 1980). Aside from Pioneer, Voyager 1 and 2 detected plasma clouds produced by dust impact onto the spacecraft by the plasma wave detectors from 6 to 51 AU (Voyager 1) and 33AU (Voyager 2) (Gurnett *et al*., 1997).

For high velocity (> 1 km/s) dust grains, the most sensitive and commonly used method is impact ionization (Auer, 2001). The most sensitive method for detecting slow-moving dust particles is measuring their charge (Auer *et al*., 2010). Lunar dust grains are charged by both the lunar plasma environment (Horányi, 1996; Wang *et al*., 2007) and triboelectricity upon release from the surface (Sternovsky *et al*., 2001, 2002). Detection methods based on momentum transfer or impact ionization are not applicable because of diminishing signal levels with decreasing velocity (Auer and Sitte, 1968). The Dust Trajectory Sensor (DTS) and Electrostatic Lunar Dust Analyzer (ELDA) instruments presented in this thesis follow this concept and will be discussed in details in later chapters.

1.2.4 Flight Instrumentation

Detectors on Explorer 16, Pegasus, and Pioneer 10 were large-area penetration detectors. If a dust particle has high speed (~ km/s), it can penetrate a thin foil (foil thickness ≈ particle diameter). The pressurized cell detector registers an impact when the cell's gas pressure

(monitored by a pressure switch) drops, because gas leaks into space through a penetration hole in the cell wall. The capacitor discharge detectors also utilize the penetrating ability of dust. A fast dust particle can penetrate the surface of a charged capacitor and strike the dielectric. The dielectric is compressed and may become conductive. The capacitor is discharged through the conductive path made by the dielectric. The Explorer 16 satellite, launched in 1962, carried several penetration detectors and the most successful type was the pressurized cell (Hastings, 1964). A similar detector was put on the Pioneer 10 (1972) and 11 (1973) spacecraft to Jupiter and beyond. The objective of this detector was to study the nature of the particles that were able to penetrate the cell walls. Pegasus satellites employed capacitor discharge detectors (Naumann *et al*., 1969). This capacitor discharge has been the basic mechanism of the Metal-Oxide-Silicon (MOS) detectors (Kassel, 1973) flown on Explorer 46 and the Long Duration Exposure Facility (LDEF) (Singer *et al*., 1985).

The Highly-Eccentric-Orbit Satellite 2 (HEOS 2) (1972) sensor was the first speed-and-mass sensor for small dust particles (Dietzel *et al*., 1973). Because of the small size, the dust particle cannot penetrate the front foil of the penetration detectors. The HEOS 2 sensor avoided such a cutoff by determining the speed from impact ionization. At high velocity, the impact of the dust particle within the instrument generates a plasma cloud, and the electrons and ions from the cloud are detected (Auer, 2001). The mass and the approximate speed of the impacting particle can be inferred from the total charge generated and the rise time of the charge pulse, respectively. The impact ionization method has been employed in many space instruments, like Particulate Impact Analyzer (PIA) on Giotto (1985) (Kissel, 1986) and Munich Dust Counter (MDC) on Hiten (1990) (Igenbergs *et al*., 1991).

Helios carried the first analyzer of the elemental composition in space (Dietzel *et al*., 1973). The Helios 1 spacecraft was launched in 1974 and its twin Helios 2 was launched in 1976. The sensor combined an impact ionization detector with a time-of-flight mass spectrometer. After the impact ionization of the dust grain and target materials, ions were extracted from the impact plume and analyzed in the time-of-flight spectrometer. An ion mass resolution of $m/\Delta m$ = 5 – 10 in the mass range 15 – 70 atomic mass units was achieved.

Galileo (1989) and Ulysses (1990) carried the large-area multi-coincidence Dust Detector System (DDS). The DDS was also an impact ionization detector, with a design similar to the HEOS 2 instrument, but a 10 times larger sensitive area (0.1 m^2). The large sensitive area provided a detection rate of about 1 impact per day and led to the discovery of jovian dust streams and interstellar dust (Grün *et al*., 1993). The main body of Galileo carrying the DDS is spinning about an axis which usually points in the anti-sun direction (Grün *et al*., 1992a). A twin instrument was operating on the Ulysses spacecraft (Grün *et al*., 1992b).

New Horizons (1996) is a NASA robotic spacecraft mission currently en route to the dwarf planet Pluto (Weaver *et al*., 2008). The Venetia Burney Student Dust Counter (SDC) onboard is an impact-based dust detector to map the spatial and size distribution of the interplanetary dust population throughout the solar system (Horányi *et al*., 2007). The sensor consists of thin, permanently polarized polyvinylidene fluoride (PVDF) plastic films. A high-velocity dust particle can penetrates through or into the film and result in complete depolarization within and near the crater or hole formed. The depolarization generates a fast current pulse in the external circuit and registers a dust impact. SDC can resolve the masses of grains with $10^{-12} < m < 10^{-9}$ g and has a total sensitive surface area of about 0.1 m^2.

The cosmic dust experiment on Pioneer 8 (1967) generated the first reliable data of dust fluxes in deep space (Berg and Richardson, 1969; Berg and Grün, 1973). The coincidence detector will be discussed more lately for trajectory measurement of individual particles.

The Cosmic Dust Analyzer (CDA) on Cassini (1997) is designed to simultaneously investigate the charge, speed, direction, mass, and composition of individual dust particles in interplanetary space and in the saturnian environment. It consists of a large (0.1 m^2) hemispherical impact ionization detector with a chemical analyzer target (CAT, area 0.02 m^2) in the middle of the hemisphere and an ion collector in center of the detector. A charge/velocity sensor is augmented in the aperture to investigate the charge, speed, and angle of the dust particles. The CDA made a lot of discoveries, such as the saturnian stream particles and the plume of Enceladus, which have been already introduced in the previous sections. The charge/velocity sensor will be discussed in details for trajectory measurement of individual particles.

1.3 Trajectory Measurement

1.3.1 Science Enabled with High Accuracy Dust Trajectory Measurements

The trajectories of dust particles are governed by the gravity of the Sun and large planetary objects as well as radiation pressure (Section 1.1.1). The trajectories are also affected by the dust particles' interaction with planetary and interplanetary magnetic fields because of the charge acquired from the space plasma environment. Many examples illustrate the complexity of interaction processes: the sporadic meteoroid dust slowly spirals towards the Sun due to the Poynting-Robertson effect and the β-meteoroid grains are expelled from the solar system on hyperbolic orbits because the radiation pressure dominates over gravity.

Dust particles can travel long distances due to their high mobility and, like photons, carry information from remote sites in space and time. With proper methods and instruments the messages sealed in dust grains can be extracted and provide unique insights into their sources and transportation processes. This is the "Dust Astronomy" concept which was introduced by Grün *et al*. (2005). This concept can be achieved by a "dust telescope" in space (Srama *et al*., 2004; Sternovsky *et al*., 2011). Targets for a dust telescope are the local interstellar medium and nearby star forming regions, as well as comets and asteroids. Full information is obtained for each particle, including the mass, chemical composition, charge, and the velocity vector. An accurate trajectory sensor can determine the origin of ejecta particles in dust clouds on Galilean moons, Io, Europa, and Callisto. Spacecraft carrying a dust telescope can get the "surface composition map" of an airless body by orbiting around it. The telescope combines the Large Area Mass Analyzer (LAMA) (Sternovsky *et al*., 2007; Srama *et al*., 2009) or other composition analyzer with a high accurate trajectory sensor. With accuracy 1 ° in angle and 1% in speed, the composition map could have ~ 1 km resolution for a 50 km orbiting altitude.

The accurate measurements of the velocity vector and the dust charge not only allows identification of the source for each detected dust particle, but also determination of the history of its interaction with the ambient environment, the interplanetary and planetary magnetic field. Take the interstellar dust particles for example; over the years of observations, the direction of the beam has changed by approximately 30 °, most likely due to the interaction with the heliospheric magnetic field (Krüger *et al*., 2007). Velocity measurement of these particles can unveil the process of the interaction and predict their motion. Interplanetary dust can also be used as a probe to study the interplanetary magnetic field if its trajectory can be measured accurately.

An active dust collector is a combination of an in-situ dust trajectory sensor together with a dust collector consisting of aerogel and/or other collector materials (Grün *et al*., 2012). It is optimized for capturing cosmic dust particles on a large-area 0.1 m^2 collector in space in the least degrading manner and returning them to laboratories on Earth for precision analysis. A dust trajectory sensor allows analyzing the pre-capture trajectories of submicron-sized and larger dust particles, and determining, for each particle, the time of capture, the precise speed, angle, and location of impact on the capture medium.

The mobilization and transport of slow moving dust particles on the lunar surface still remain elusive. Accurate velocity measurement of these particles can determine the dynamic of the dust and help us to better understand the charging process. Auer (1982) proposed to determine non-destructively the mass of a charged dust particle from the bending of its trajectory in a strong electric field, using high-resolution velocity/trajectory sensor. A particle's mass is derived from its charge-to-mass ratio, which is obtained by measuring the deflection of its path in an electric field and from its charge. One of these applications is the Electrostatic Lunar Dust Analyzer (ELDA) instrument, which has been developed for the detection of slow-moving dust particles mobilized by meteoroid bombardment and/or electrostatic forces (Duncan *et al*., 2011). The ELDA will be discussed in detail in later chapters.

1.3.2 Historical Perspective

Many of the discoveries and basic characterization of cosmic dust were accomplished by *in situ* dust detectors. The mass, composition, and speed can be measured directly for each particle using impact detectors, but the direction is obtained only by statistical analysis for most flight instruments. The exceptions are the dust detector on Pioneer 8 and the Cosmic Dust Analyzer (CDA) on Cassini, which will be discussed in details below. The *in-situ* dust detectors

have a large field-of-view (FOV) (> 45 ° half angle, typically), and the only information on the directionality of the dust particle is the orientation of the dust detector at the time of the impact, like Galileo and Ulysses. Thus the detection of a large number of particles is needed for establishing a meaningful distribution and determining the most likely impact direction. This is possible for the case of a well-collimated dust stream, such as the jovian dust stream, or interstellar dust particles, but not for other applications. Furthermore, the statistical data analysis requires the orientation of the dust detector to be swept over all direction, e.g., spinning spacecraft, which may not be desired.

The history of individual dust particle trajectory determination started with the Cosmic Dust Experiment on Pioneer 8 in 1967 (Berg and Richardson, 1969). Using a coincidence technique, the instrument generated the first reliable data of dust fluxes in the deep space. Impact location detectors were used to estimate the impact location, the incidence angle (±27 °) and speed (10%-15%). Figure 1.4 shows the schematics of the sensor. In addition to the large uncertainties in angle and speed, there are also other problems. Dust particles with slow speed or small size cannot penetrate the film and measured dust particles would be damaged by the impact process.

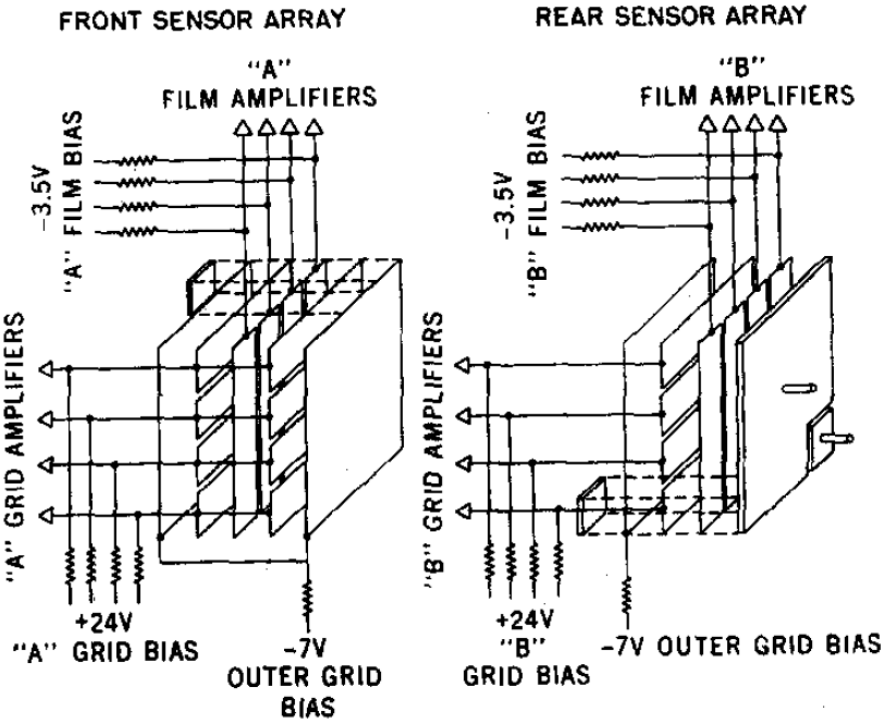

Figure 1.4: Schematic diagrams of sensor array on Pioneer 8. For the front sensor, the plane of the four vertical film strips and the plane of the four horizontal film strips form the front array. The right two planes form the rear array. Both the front and rear array consist of 4 × 4 square segment. Speed and directional information is obtained from the particle time-of-flight between front and rear array and the two impact locations. (from Berg and Richardson, 1969).

A similar concept of trajectory measurement of high-speed dust particle was introduced by Simpson and Tuzzolino in 1985. The detection is based on dust particle's penetrations in polarized thin-film polyvinylidene fluoride (PVDF) detectors instead of the film strips used on Pioneer 8. With a better determination of the penetration location, the measurement yielded velocities within 5% of incident velocities and the mean error angle was limited to ~ 4 °(Simpson and Tuzzolino, 1989).

The measurement of trajectory is possible through the detection of the charge the dust particles carry, a technique proposed by Auer (1975). In the interplanetary space, solar UV induced photoelectron emission is the dominant process and the particles will acquire

approximately +5 V surface potential (Zook *et al.*, 1996). In the shadow of big objects, or within planetary magnetospheres with higher density plasma, the particles are charged negatively because of the high flux of plasma electrons, and the expected surface potential is on the order of the electron temperature (in eV) (Horanyi, 1996).

The charge and velocity detector of the CDA on Cassini measured the velocity through detecting the charge on the dust particle (Auer *et al.*, 2002), and it was the first in-situ charge measurements of interplanetary grains (Kempf *et al.*, 2004). It was designed following a time-of-flight technique. The schematic of the detector on Cassini is shown in Figure 1.5.

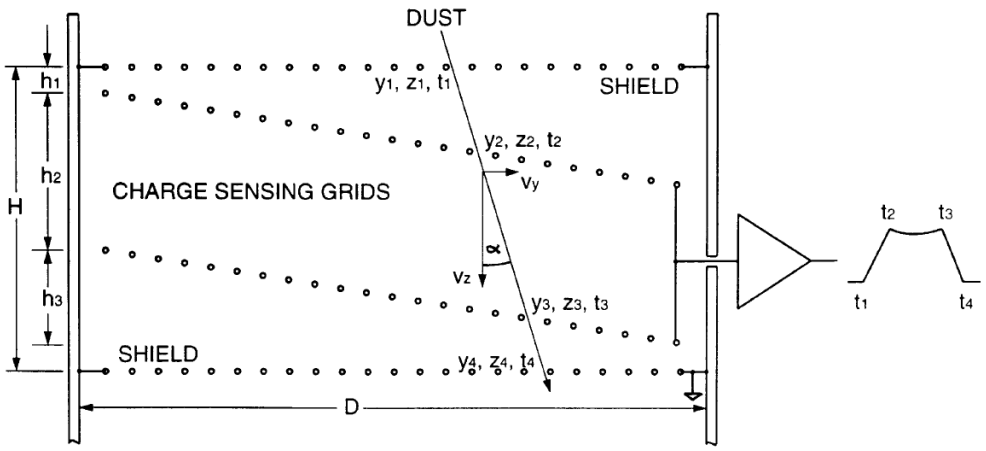

Figure 1.5: Schematic cross-section of the charge and velocity detector of the CDA on Cassini. There are four planes of grids; the two inclined grids are connected together and connect to a charge sensitive amplifier. The front and rear grids, together with the cylindrical walls, form a Faraday cage that shields the two charge sensing grids. The induced charge on the two inclined grids is a function of the particle position. The signal has a trapezoidal shape with times t1…t4 corresponding to the times when a dust grain passes through the 1st… 4th grid, respectively. The velocity information can be derived based on the shape (from Auer *et al.*, 2002).

The accuracy of the detector can be estimated from the calibration performed at the Heidelberg dust particle accelerator facility (Auer *et al.*, 2002). The dust particles used for this experiment are iron microspheres with diameters of a few microns, speeds of 2 – 5 km/s, and

high positive charges ranging from 60 to 700 fC. During the calibration, the CDA can be rotated about the *x*-axis. Eight or nine dust particles were shot for each fixed position.

For normal incidence, speed v_z measured by the charge and velocity detector of the CDA were found to closely agree with v_z [km/s] = (1.027 ± 0.011) v + 0.125, where v is the measured by the pickup-tube detector following the accelerator (Auer *et al*., 2002). In order to test the angular response, the CDA was tilted with respect to the particle beam, and the tilt angle was stepped from − 58° to 0° in intervals of 1°. Figure 1.6 shows the calculated angle of incidence from the detector as a function of the tilt angle. Since the dust particles from the accelerator are well collimated (< ± 0.1 °), the spread of calculated angles of incidence is characteristic of the accuracy of the detector. For high charge-to-noise ratio (QNR>100), the accuracy in angle for this detector is estimated to several degrees from the relation between the measured angle and tilt angle, and the accuracy in speed is several percent based on the agreement between the v_z and v.

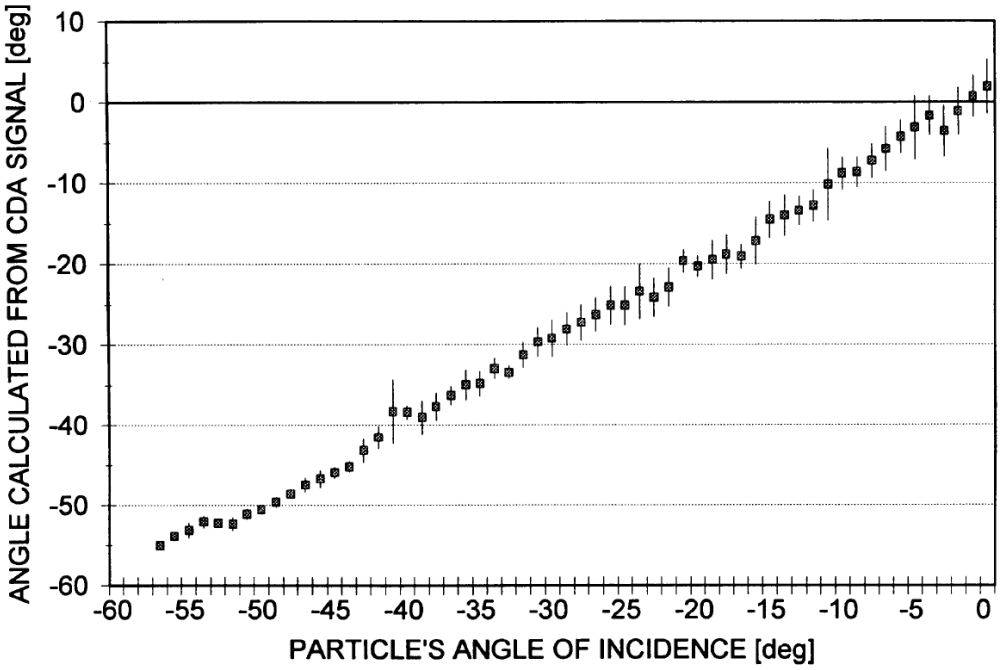

Figure 1.6: Angle of incidence measured by the charge and velocity detector of CDA, as a function of the tilt angle between the detector axis and the direction of the dust beam. The error bars indicate the standard deviation of the eight or nine dust samples taken at this angle. (from Auer *et al*., 2002).

2. Dust Trajectory Sensor (DTS) Definition

2.1 DTS Description and Capability

The accurate velocity measurement of individual dust particles has a range of applications in different areas of cosmic dust research. Among those trajectory sensors flown, the charge/velocity/trajectory sensor is the only nondestructive type and, therefore, our preferred choice. The cosmic dust analyzer CDA on Cassini carries a simplified version, where the two inclined grids are connected to a single amplifier (Auer *et al*., 2002). With an area of 0.1 m^2 it detected six dust particles within three months in interplanetary space (Kempf *et al*., 2004). One drawback of this sensor is that it can only sense electric charges greater than 1 fC of individual cosmic dust grains. From the equation for the surface potential of a charged spherical grain a convenient formula for the dust charge can be derived: $Q \approx 700 \Phi a$, where the charge Q is measured in elementary charges e^-, the surface potential Φ is in Volts, and the radius of the dust, a, is in μm. Dust grains exposed to the environment of space typically are charged to about +5 V surface potential due to solar UV illumination. A charge of 1 fC corresponds to a dust particle as small as $a = 1.8$ μm. Another drawback is that the detector only measures the two components v_y and v_z of the velocity (see Figure 1.5), and cannot completely describe the velocity and trajectory of the dust particle.

The Dust Trajectory Sensor (DTS) discussed in this work follows the concept of the charge and velocity detector of the CDA on Cassini: charge detection (Auer and von Bun, 1994). The DTS is based on measuring the distribution of the induced charges on an array of wire electrodes from a dust particle passing through. Wire electrodes have a small capacitance and the resulting lower electrical noise allows extending the detectable range toward smaller dust particles. The electrodes are arranged into four planes with orthogonal orientation of wires

between alternating planes, as shown in Figure 2.1. Each electrode is connected to a separate Charge Sensitive Amplifier (CSA). The electrode array is shielded within a Faraday box at ground potential for maintaining a low-noise environment. High open area ratio grid electrodes are used on the top and bottom allowing the particles to enter and exit the DTS. As the charged dust particle is passing through the instrument, it will induce charges on the wire electrodes and conducting walls. The sum of all induced charges is equal and opposite in polarity to the charge on the dust. The induced charge on each electrode is a function of the dust's position, and therefore a function of time. The induced charges are measured using CSAs and recorded in memory. The particle's velocity vector in the DTS is obtained by the shape, amplitude, and timing of the signals. A DTS with only two planes of wires which are arranged in perpendicular directions is also capable for obtaining full three-dimensional velocity information. However, the uncertainty will increase very fast as the noise increases.

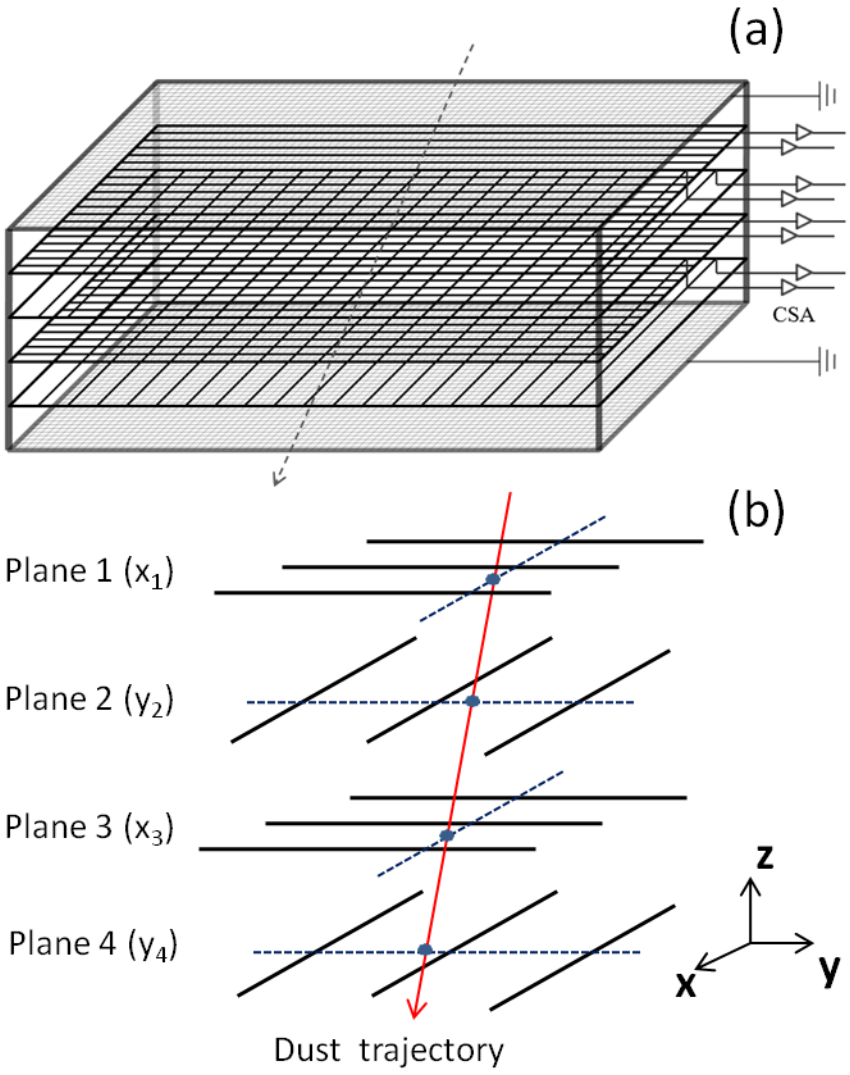

Figure 2.1: (a) The schematic of the Dust Trajectory Sensor (DTS). The entrance and exit grids are part of the shielding Faraday box around the array of electrodes. The four planes of electrodes are arranged in alternating directions and each wire electrode is connected to a separate Charge Sensitive Amplifier (CSA). (b) When a charged dust particle passes through the sensor, mirror charge is induced on the electrode. The shapes of the signals on wires in one plane determine the one-dimensional coordinates (x_1, y_2, x_3, y_4) of the trajectory. The charge information is obtained from the amplitude of the signals.

Auer *et al.* (2008) have performed a thorough numerical analysis of the DTS using the COULOMB software from Integrated Engineering Software/Enginia Research (Winnipeg, Manitoba, Canada). The goal was to establish a geometry that is optimal for operation and the

following parameters were established: (1) radius of the wire electrodes: 0.20 mm, (2) the spacing between wires in one plane: 20 mm, (3) the separation distance between the electrode planes: 40 mm, (4) distance of the entrance and exit grids from the closest electrode planes: 40 mm, and (5) distance of the walls of the Faraday shielding box from the closest wire electrode: 20 mm. These values ensure a good signal-to-noise ratio, an acceptable number of wire electrodes in the system and a large FOV.

A prototype of DTS was designed by Sternovsky, and built in the laboratory by Sternovsky, Drake, and Duncan in 2009. The geometry parameters are the same to those established in the numerical analysis (Auer *et al.*, 2008), except the radius of the wire is 0.195 mm instead of 0.2 mm. The number of wires in each plane is set to 19 for a large FOV, thus the geometry of the DTS is 400 × 400 × 200 mm (see Figure 2.2). The wires are stainless steel cables stranded from 7 thinner wires.

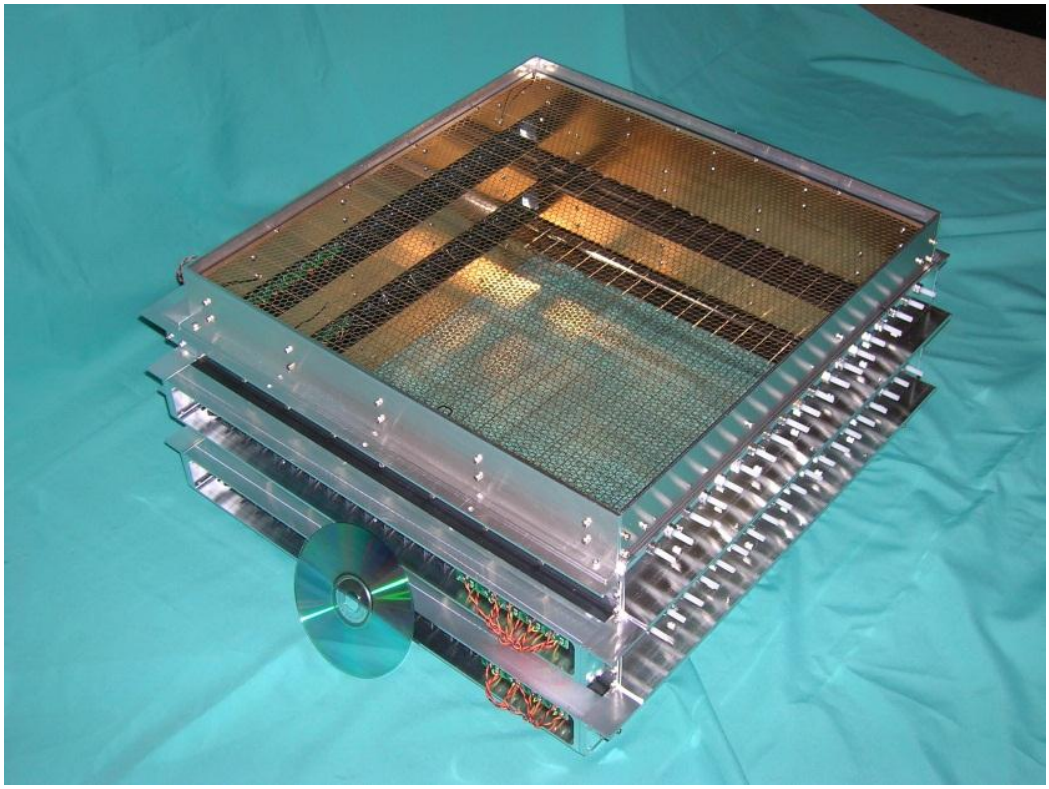

Figure 2.2: The DTS laboratory prototype. It has 19 wires per plane and the wire electrode is 0.195 mm in radius. The width and length are both 400 mm and the height is 200 mm.

The frame of the Faraday shielding is made of aluminum. The entrance and exit beryllium–copper (BeCu) grids are hexagonal in pattern with a transmission of 0.8. The transmission of one wire plane is $(20 - 0.39)/20 \approx 0.98$. Therefore, the transmission of the whole DTS is $0.8 \times 0.8 \times 0.98^4 = 0.6$. Each wire electrode is connected to a CSA. However, in the testing experiments of this thesis, only three, five or eight wire electrodes in each plane are active and connected to CSAs based on the experiment requirements and setup while other wires are connected to signal ground.

The DTS can detect dust particles with a high probability (≥ 99%) at charge-to-noise ratio (QNR) as low as 6.25 at velocities ≤ 20 km/s. When v is ≥ 20 km/s, the minimum QNR varies $\sim v^{1/2}$ for different v to keep this high detection probability due to limited sample points (Auer *et*

al., 2010). The sensitivity of the DTS instrument is defined as the smallest detectable dust size which is ultimately limited by the noise level of the CSAs. An application-specific integrated circuit (ASIC) has been developed for the space applications of the DTS instrument (Srowig, 2004; Srama *et al*., 2005). The circuit is a front-end CSA combined with a logarithmic amplifier for increased dynamic range from 10^{-16}-10^{-13} C. It has a root mean square (RMS) noise corresponding to about 1.5×10^{-17} C (100 e^-) with a bandwidth from 10 kHz to 10 MHz (Srama *et al*., 2005; Auer, 2007). By developing ultralow-noise amplifiers and using one amplifier per sensor wire instead of one for a pair of wire grids, DTS is capable of detecting and analyzing dust charges $\geq$ 0.1 fC (QNR = 6.25), which corresponds to a minimum detectable dust size of approximately a = 0.18 μm. With an area of 0.16 m^2, DTS is capable of measuring dust with low flux.

From the four coordinates (x_1, y_2, x_3, y_4) from the four planes of electrodes, DTS provides the complete three-dimensional information of the velocity/trajectory. Its precision is estimated by numerical study as 1% in speed and 1 ° in angle at a low QNR $\approx$ 10, which has been confirmed by laboratory testing at the Dust Accelerator Facility of the Max-Planck-Institute Heidelberg with dust particles at speed 2-5 km/s. More details about the accuracy analysis and the laboratory testing will be discussed in later chapters.

2.2 DTS Electronics

The CSAs connected to the electrodes are used to measure and amplify the induced charge on the wires when charged dust particles pass nearby. The noise performance of the CSA determines the smallest detectable dust charge and places a lower limit on the sensitivity of the instrument. The CSA electronics are constructed from common off-the-shelf components, on account of the large number of electrodes. The DTS interior is lined with 0.25 mm thick solid

BeCu sheets that are interconnected at each corner. There are small holes in the liners for the electrodes to pass through. The liners and the grids together form a Faraday cage that shields the wire electrodes. The Faraday cage is isolated from the mechanical structure and connected to the signal ground of the CSAs. The wire electrodes are electrically isolated and a simple mechanical structure is used to stretch the wires straight. The CSA electronics are mounted approximately 0.15 mm away from the electrodes, just outside the Faraday cage.

Two CSA configurations are used within DTS and optimized for different speed ranges. For high speed (1-100 km/s) measurements, the CSA electronics used in the laboratory model is shown in Figure 2.3. The first stage is a CSA with a C_1 = 0.5 pF capacitor and R_1 = 100 MΩ resistor in the feedback, followed by a 10× inverting amplifier and a unity gain buffer amplifier. The measured sensitivity is 1.2×10^{13} V/C, or about 1.9 μV/e^-. The RMS noise is equivalent to 1750 e^-. Each CSA is calibrated to a precision of <1%. The bandwidth of the CSA circuit is approximately 10 kHz – 10 MHz and is suitable for the detection of dust particles passing through the instrument with 1-100 km/s velocity.

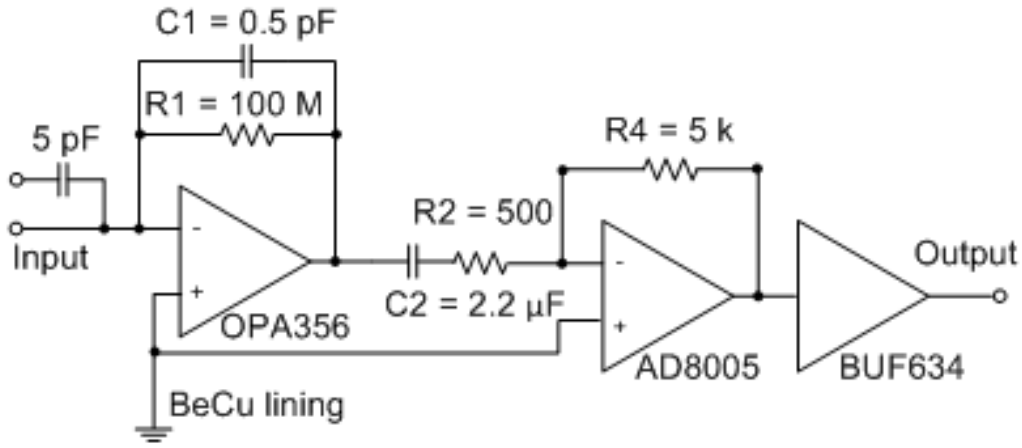

Figure 2.3: The schematics of the charge sensitive electronics (CSA) for high speed (1-100 km/s) dust particles integrated into the DTS laboratory version. The first stage is a CSA with C_1 R_1 feedback and the second stage is a buffer amplifier.

For the application of Electrostatic Lunar Dust Analyzer (ELDA), which measures slow moving (1-100 m/s) dust particles, the CSA in DTS is changed. Figure 2.4 shows the schematics of CSA for slow-moving dust particles used in the DTS. The first stage is a CSA with a C_1=5 pF capacitor and R_1=30 GΩ resistor in the feedback. The non-inverting input is connected to the BeCu liner and represents the signal ground. The LTC6240 operational amplifier is selected for its low noise, low drift and low bias current characteristics. The first stage is followed by an ac-coupled voltage amplifier with a gain of 91. The RMS noise is equivalent to 750 e^-. The bandwidth of the CSA circuit is 7 Hz–10 kHz and is selected for the detection of dust particles passing through the instrument with 1−100 m/s velocity. The separation distance between the wire electrode planes is 40 mm and thus the duration of the image charge signal on one wire is approximately in the range from 40 to 0.4 ms.

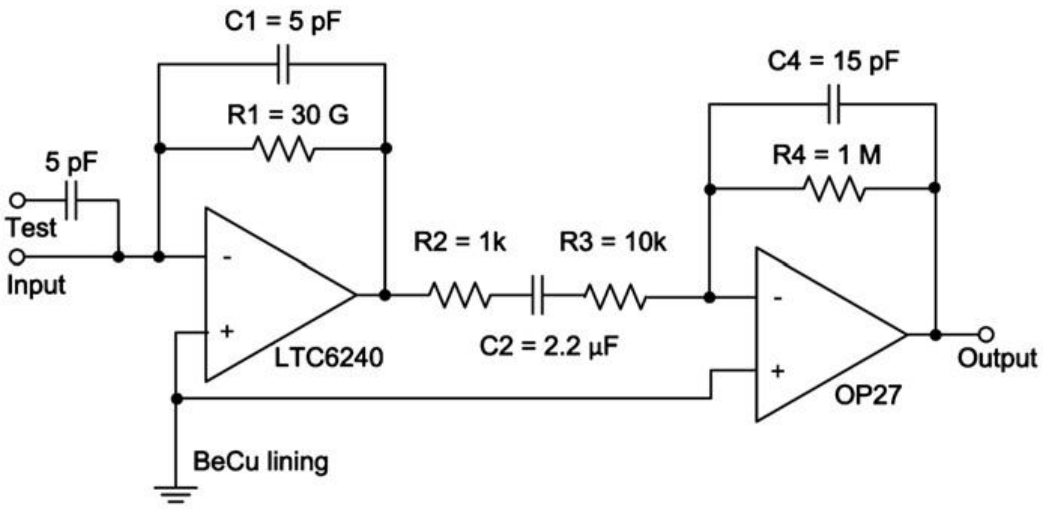

Figure 2.4: The schematics of the charge sensitive electronics (CSA) in DTS for low speed (1-100 m/s) dust particles.

The effects of electronics on the measurement are important because they affect the shape and amplitude of the induced charge signals directly. The limited bandwidth reduces the noise of the CSAs, but may distort the charge signal, and this effect is more significant for slow-speed measurement than the high-speed measurement. The measured signal can be corrected in the frequency domain using the equation

$$S_c(i\omega) = \frac{1}{i\omega}\frac{S_m(i\omega)}{G(i\omega)}, \qquad (2.1)$$

where ω is the angular frequency, i is the imaginary unit and S_m and S_c are the Fourier transforms of the measured and corrected signals, respectively. For different CSAs, the transfer function $G(i\omega)$ is different. Take the CSA in Figure 2.4 for example, the transfer function is

$$G(i\omega) = \frac{R_1}{(1+i\omega\tau_1)}\frac{i\omega\tau_2}{(1+i\omega\tau_2)}\frac{R_4}{(R_2+R_3)}\frac{1}{(1+i\omega\tau_3)}. \qquad (2.2)$$

The time constants correspond to $\tau_1 = C_1R_1 = 0.15$ s, $\tau_2 = C_1 (R_2 + R_3) = 0.242$ s, and $\tau_3 = C_4R_4 = 15$ μs. Figure 2.5 shows the correction of the measured signals using Equations 2.1 and 2.2.

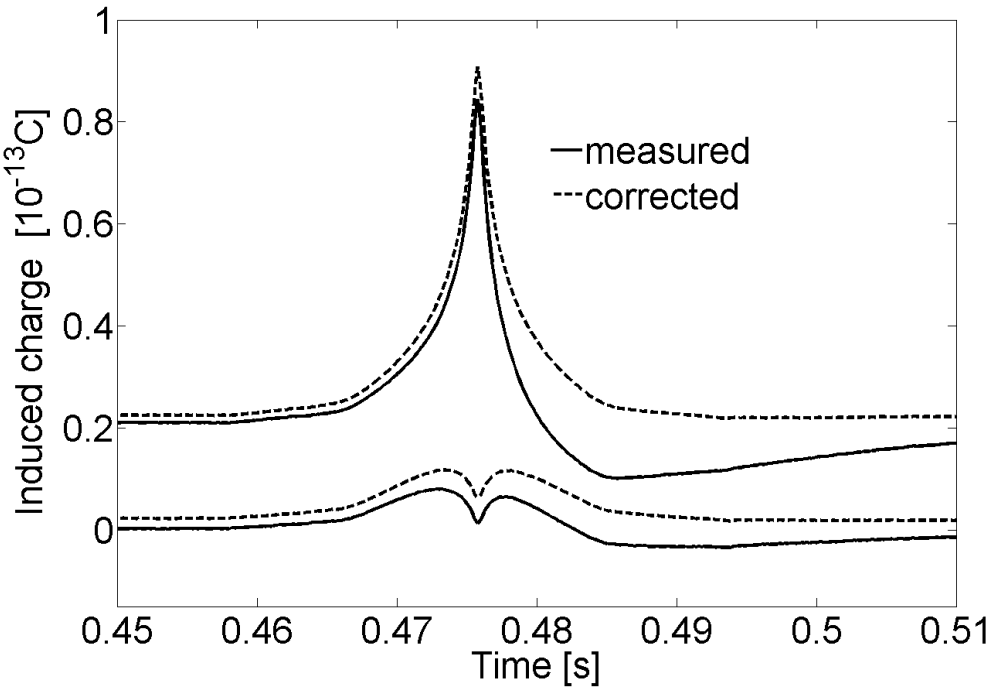

Figure 2.5: The correction of the measured signals using Equations 2.1 and 2.2. Signals from two adjacent wire electrodes are shown for a dust particle moving through DTS at approximately 4 m/s velocity. The signals are shifted in the vertical direction for clarity.

2.3 DTS Improvements

A new DTS (DTS2) was designed by Sternovksy, Gemer, Drake, and Duncan, and built by Drake, Duncan, and Le in summer 2011 with a better mechanical integrity and electronics. Throughout the construction and testing of the old DTS (DTS1), a number of areas of deficiency were noted. It is the intent of the redesign of the DTS to correct these deficiencies, resulting in the DTS2. The two DTS units have identical geometries; however, the DTS2 has improved mechanical and electrical properties.

First, we introduce the improvements in configuration/geometry. (1) In the old DTS, each plane of wires was housed in a single square aluminum frame; four wire planes required five separate frames to be stacked on top of each other. Since the wire array in each plane exerted

force on the square frame, the frame had a tendency to go out-of-square and become a parallelogram when the joints at the four corners of the frame were compromised. As a result, it was exceedingly difficult to get the four planes to attach to each other cleanly once the electrode wires had been installed and tensioned. In the new DTS, this problem was corrected by making each frame support two perpendicular planes of wires. Thus, the forces in the perpendicular directions were equivalent, resulting in lower stress at the corners of the frame. Therefore, the tension in the electrode wires actually helped to keep the frame square, rather than disturbing the frame geometry. (2) In the old DTS, each wire was composed of 7 thinner stainless steel wires, secured at one end by a solder joint, and at the other with a set screw, a plastic rod, and a stainless steel nut. This presented numerous problems. The wire was supplied on a roll, and it took a large amount of tensile force to make the wire run straight across the instrument. This wire also tended to slip from its tensioning device, making the application of the necessary tensile force very challenging. Finally, if it was necessary to replace a wire once the DTS had been assembled, it was quite laborious and overly complicated to do so, as the wire had to be fed through its individual hole and cut to length when installed in the instrument. These problems were remedied in the new DTS by using a 49-strand braided stainless steel wire, which was much more flexible and required far less force to sit straight in the instrument. This wire was also much easier to connect at each end, and a spring was incorporated into the non-CSA end of each wire. Not only did this tensioning system allow for individual fine-tuning of the tension in each wire which was not previously possible, it allowed constant tension to be applied to each individual wire. Finally, the tensioner design also allowed each wire and tensioner to be replaced individually, with a pre-fabricated unit that had been assembled outside of the instrument on a special jig. This made replacement of damaged wires much easier, as a number of new wire and

tensioner assemblies could be on-hand and ready for installation at any time. (3) The old DTS used strips of beryllium copper mounted to the inside surfaces of the instrument as a signal ground plane. These strips were difficult to mount and remove, and had a tendency to be wavy and uneven. This problem was fixed in the new DTS by incorporating the signal ground plane into the pre-fabricated wire and tensioner assembly as a small square copper-plated PCB board. Each wire and tensioner assembly featured two plated PCBs, one for each wall of the DTS that the wire passed through. Again, this made assembly of the instrument simpler, as well as making the ground plane more uniform and effective.

Next, we introduce the improvements in the electronics. The electrical circuits in the new DTS are similar to the old ones, but their physical layout and connections are greatly modified to reduce noise. (1) The CSA are placed as far as possible from dielectric materials to avoid micro-phonics. (2) The circuit boards are mounted to Delrin brackets instead of Noryl brackets because the surface of Noryl holds charge. In the old DTS, the Noryl is charged strongly and is suspected to be the primary contributor to vibration noise because the charge and close proximity to the electronics. (3) Each CSA is on its own PCB instead of placed together on a single PCB, as in the old DTS. Only the offending CSA board has to be removed and replaced to remedy a "dead" channel, rather than removing the entire CSA array. (4) Power is transferred to the CSA through rigid connectors rather than cables which are used in the old DTS. The use of rigid connectors reduces the inductance in the supply lines and micro-phonic pickup from vibrations in the instrument. (5) Four-layer boards are used instead of the two-layer board with exposed traces. The signals run on the two inside layers, which are protected by the grounded layers on the outside of the board. (6) The two stages of CSAs are mounted on one board to avoid noise. The CSAs in the old DTS are split on two separate PCB boards and the first stages are mounted

inside a faraday cage. In this configuration, the sensitive first stages are protected from the noise of the second stage because an unshielded first stage is subject to significant capacitive coupling with the second stage. The disadvantage is that signals have to travel unshielded via two solder junctions before getting to the second stage amplifier and the noise produced in this process is amplified in the second stage. In the DTS2, these noises are avoided by placing the circuits on one board and the capacitive coupling is mitigated by a shield placed 3 mm above the amplifiers.

In summary, for DTS2, more flexible wires are used that remain straight with less tensioning force, and the mechanical tensioning and positioning of the wire electrodes is improved to provide better than ± 0.2 mm accuracy while the accuracy is around ~ 0.4 mm in DTS1. The distance between the end of the wire and the CSA input is reduced to minimum and also enclosed by a Faraday shield. These improvements have greatly reduced the instrument's susceptibility to acoustic noise. Individual voltage regulators are also added to each CSA circuit to reduce the cross-talk between the channels. The RMS noise level of the CSA electronics used for high-speed dust particle is reduced approximately from 2.8×10^{-16} C (1750 e^-) to 2.4×10^{-16} C (750 e^-) and noise level for low-speed DTS is reduced from 1.2×10^{-16} C (750 e^-) to 5.7×10^{-17} C (356 e^-).

3. Dust Trajectory Sensor Modeling

In this chapter we describe the computer model developed for the DTS instrument. The main goal of this work is to calculate the signals for each wire electrode for a dust particle passing through the instrument on an arbitrary trajectory. Later, these results will be used to calculate the velocity vector from the DTS measurement by finding the best match between the data and simulations of known trajectories.

In principle, the charges induced on the wire electrodes from a charged dust particle can be calculated with arbitrary accuracy using electrostatics and it is obvious from the complexity of the instrument geometry that numerical methods need to be applied. We have chosen the COULOMB software package from Integrated Engineering Software/Enginia Research (Winnipeg, Manitoba, Canada) for the simulations. The choice was based on past experience and performance (S. Auer, personal communication).

With the COULOMB software we can calculate the distribution of the induced charges within the DTS for an arbitrary dust position, and the dust trajectory signals (temporal evolution of the induced charges) can be reassembled from a series of point calculations. When doing the calculations, a number of simplifying assumptions and compromises have to be made between the accuracy and speed. The DTS instrument consists of an array of thin wire electrodes within an enclosure box with grounded walls. Both the number of wire electrodes used and the distance from the dust particle to the wall will affect the distribution of the induced charge. Because of limited calculation power, it is difficult to calculate the induced charges for all possible dust positions within the DTS. In fact, we need to use a reduced-size DTS setup to keep the problem computationally feasible. Furthermore, we use the symmetric and periodic properties of the electrode arrangement to reduce the required calculations to a small kernel volume. As accuracy

is a concern, we keep record of the small errors introduced with each simplification made. The data analysis algorithm and accuracy will be discussed in the next chapter.

3.1 COULOMB Setup

The DTS instrument is a closed box with grounded walls with four electrode planes consisting of 19 wires each. Wires on a single plane are arranged in an orthogonal direction to wires on an adjacent plane. The numerical model is built according to Auer *et al.* (2008), using the same parameters as the DTS prototype instrument (see section 2.1): (1) The radius of the wire electrodes is a = 0.195 mm, (2) the spacing between wires in one plane is D = 20 mm, (3) the separation distance between the electrode planes is P = 40 mm, (4) the distance of the entrance and exit grids from the closest electrode planes is P = 40 mm, and (5) the distance of the walls of the Faraday shielding box from the closest wire electrode is D = 20 mm.

The electrostatic modeling of DTS is computationally demanding due to the combination of the large volume and the fine features of the wire electrodes that need to be resolved. The number of elements required to resolve the problem is high and, moreover, the memory requirement of COULOMB increases by the square of the elements. The full DTS model with four planes and 19-wires per plane exceeded the existing computational capabilities so we have reduced the DTS model size to 9-wires per plane. We will later show that this reduced-size model is sufficiently accurate to calculate the signals as the charge distribution on the wires close to the path of a dust particle becomes nearly insensitive to the increasing number of electrodes in each plane. In addition, the boundary element method (BEM) is employed for modeling the electrode array as it can incorporate open space and adapts small features within a large volume and thus is the preferred method for modeling DTS.

Figure 3.1 shows the computer model of the DTS. The origin of the coordinate system is at the center of the box and the axes are defined as shown. The charge on the dust is normalized to unity and the dust particle is modeled as a 5-micron-radius sphere with uniform volume charge distribution. Notice the small kernel in the center of the instrument. We only calculate the response of the wires when the dust particle is in that kernel. The kernel results can be extended to most of the entire volume of the instrument, which will be shown in section 3.4.

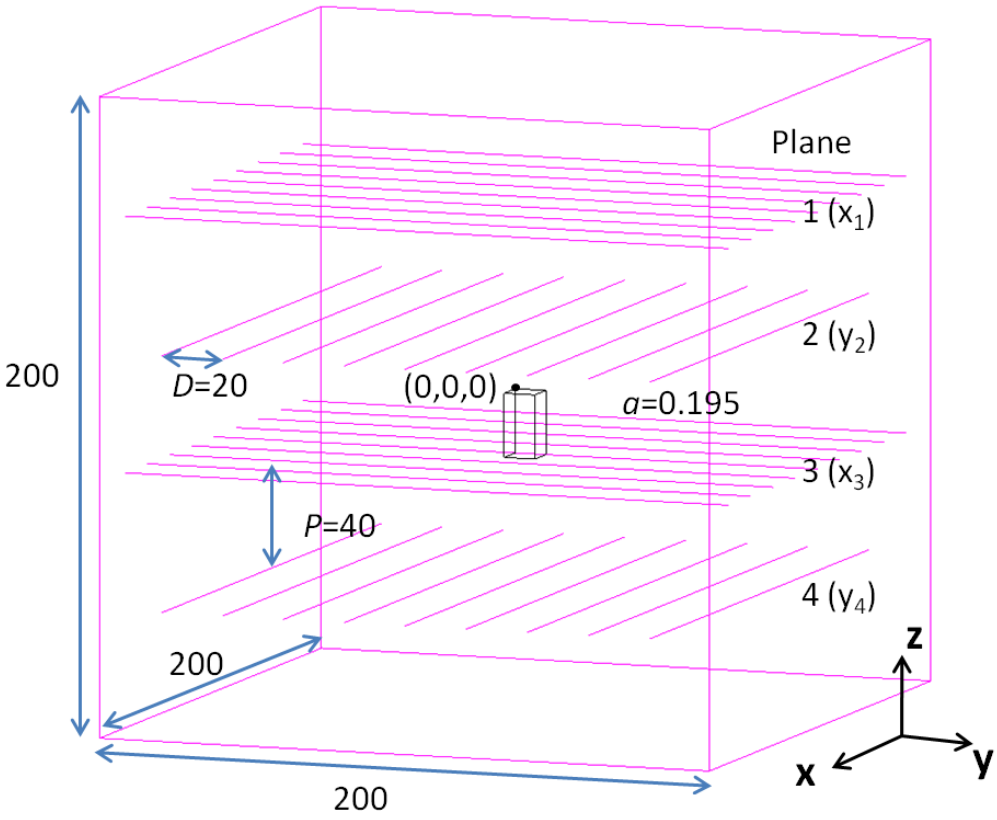

Figure 3.1: The COULOMB model of the DTS. There are four electrode planes with nine wires in each, which determine the four one-dimensional coordinates (x_1, y_2, x_3, y_4) of the particle's trajectory. The wires in planes 1 and 3 are along the *y*-axis and wires in planes 2 and 4 are along the *x*-axis. The origin of the coordinate system is placed at the center of the box. All dimensions are given in mm.

The configuration of the DTS in the computer model is as follows. The side walls of the box are grounded and divided into two-dimensional (2D) elements. The grounded grid electrodes at the top and bottom are simulated as simple conductive walls, because the cell size of the hexagonal openings (<5 mm) is small compared to the distance to the closest electrode plane (20 mm). The Coulomb software allows different ways of treating the charged dust particle and the wire electrode surfaces. These configurations affect both the accuracy and the speed of the calculation, and thus need investigation. A charged dust grain in Coulomb can be treated with (a) uniform surface charge distribution, (b) constant surface potential, or (c) uniform volume charge distribution. In the former two cases, the surface of the dust is subdivided into 2D elements and in the case (c) the dust particle is subdivided into three-dimensional (3D) elements.

In case (a), the charge is not allowed to redistribute on the surface of the dust particle. Cosmic dust is dominantly made out of insulating materials, so a constant uniform surface charge is reasonable. In case (b), the dust particle and the wire electrodes are capacitively coupled and the charge on the dust particle changes with distance to the electrodes, as the capacitance is changing and the surface potential is constant. However, this is not a problem for our calculations, since the total charge on the electrodes (and walls) is always equal and opposite to that on the particle. The charge distribution on the electrodes can be normalized to the charge on the dust particle which is also calculated. In this case, the dust particle is treated as a conductor and the charge is free to redistribute to satisfy the constant surface potential requirement. Case (b) is thus a physically viable option. In case (c), the charge is distributed over the volume of the particle and is immobile. The results presented in Sec. 3.2 show that the effect of the dust particle size can be ignored when particle radius a is less than 5 microns. For smaller

particles thus the difference between surface and volume charge distribution is negligible. Therefore, case (c) is also a viable option for the calculations.

The thin wire electrodes can be treated in COULOMB as (i) cylinders with 2D surface elements, or (ii) one-dimensional (1D) segment with a small defined radius. For case (ii) to be applicable, the requirement is that the radius is much smaller than the length, which is satisfied in DTS. The 1D segment has a virtual surface with constant potential and the charges on the 1D element are calculated to satisfy this surface potential.

There are a total of six configuration combinations: three for the dust particle and two for the wire electrodes. A simple test calculation is performed to find out the calculation speed and accuracy of these combinations. The dust particle is moved along the same defined trajectory: from coordinates (10, 0, 0) (equally far from plane 2 and plane 3) to (10, 0, −20) (equally far from two wires), then to (0.3, 0, −20) (close to a wire). The distributions of the induced charges in different configurations are calculated and compared. The results are summarized in Table 3.1. The table shows the maximum difference of the induced charge, $\Delta q/Q$, on one wire for two different dust-wire (center-to-center) distances: larger distance, d = 1-10 mm, and close proximity, d = 0.3-1mm. $\Delta q/Q$ is the largest induced charge difference (relative to case 1) on one wire (Δq) relative to the dust charge (Q). The bottom line from the analysis is that all configurations provide the same results with only negligible differences; however, case 6 is much faster to calculate than the other options. Clearly, the best option is to choose uniform volume charge for the dust particle and the 1D segment division for the wire electrodes.

Table 3.1: The maximum difference of induced charge, Δq, on one electrode and calculation speed for different configurations. Q is the total charge on the dust and d is the dust-wire distance. Case 1 is the reference (see text for details).

Configurations	$\Delta q/Q$ (d=1-10 mm)	$\Delta q/Q$ (d=0.3-1mm)	Calculating Speed
1.(a)+(i)	0	0	~1 hour per position
2.(a)+(ii)	0.18%	0.13%	~1 hour per position
3.(b)+(i)	0.17%	0.12%	~1 hour per position
4.(b)+(ii)	0.20%	0.13%	~1 hour per position
5.(c) +(i)	0.23%	0.21%	~1 hour per position
6.(c)+ (ii)	0.24%	0.20%	~1 min per position

3.2 Effect of the Dust Particle Size

Shape and size of the dust particle also affect the induced charge distribution. The same trajectory in Section 3.1 is used for the test calculation to find out the difference of the induced charges on electrodes for different particle sizes. The claimed dust particle size limit for DTS is as small as 0.2 microns. Three representative dust particle sizes are used in the model: a = 0.5, 5, and 50 microns, and 5 microns is the reference. Table 3.2 shows the results of the comparison. The results show that the effect of the particle size is diminishing quickly with decreasing radius. The difference from 5 microns to 0.5 microns is negligible even for very short dust-wire distance d = 0.3-1mm, which means that a model of 5 microns size particle is very accurate for all particles smaller than 5 microns. The difference between 5 microns and 50 microns particle sizes is also small, which indicate that the 5-micron model is still good for real particles within 50 microns in size. The effect of shape is very similar to that of size, thus can be ignored.

Table 3.2: The maximum difference of induced charge, Δq, on one electrode for three different dust particle sizes. Q is the total charge on the dust and d is the dust-wire distance. a = 5 microns is set as reference.

Particle size a [μm]	$\Delta q/Q$ (d=1-10 mm)	$\Delta q/Q$ (d=0.3-1mm)
5	0	0
0.5	4.7×10^{-4} %	0.095 %
50	0.294%	0.476%

3.3 Effect of the Model Size

With the reduced-size model, the electrodes are shorter and the effect of the sidewalls is more pronounced as they are closer to the path of a dust particle. In this section we show that a reduced-size model with 9-wires per plane is a reasonable compromise between calculation speed and accuracy. We built two additional models with the same parameters, except one with 7 and one with 11 wires per plane. The same trajectory in Section 3.1 is used for the test calculation to find out the difference of the induced charge. Table 3.3 shows the results of the comparison of the three different models, considering the induced charges on the inner 28 electrodes. The model with 9-wires per plane is the reference. The results show that the effect of the model size is diminishing quickly with increasing number of wires per plane. The difference from 9 wires going to 11 is negligible and we conclude that the model with 9 electrodes has sufficient accuracy.

Table 3.3: The maximum difference of induced charge, Δq, on one electrode for three model sizes. Q is the total charge on the dust and d is the dust-wire distance. The model with 9 wires per plane is the reference.

Model size	$\Delta q/Q$ (d=1-10 mm)	$\Delta q/Q$ (d=0.3-1mm)
9 wire per plane	0	0
7 wire per plane	0.174%	0.078%
11 wire per plane	0.057%	0.028%

3.4 Properties of the DTS: Symmetry and Periodicity

The symmetric and periodic properties of the DTS discussed in this section allow extending the solutions from a small kernel volume to the entire instrument. The kernel is in the middle of the DTS, with the sides defined by x = [0, 10] mm, y = [0, 10] mm, and z = [−20, 0] mm, shown in Figure 3.1. Within the kernel, the distribution of induced charges on the electrodes is calculated for dust positions defined by a matrix with 1 mm spacing in each direction. Additional calculations are done for close proximity between the dust and the electrode with 0.1 mm spacing for d < 1 mm, where the charge distribution varies steeply with position. The total charge on the dust particle is assigned to be −1. The numerical model yields the induced charge $Q_{M,N}$ (x_i , y_i , z_i) on each wire relative to the charge on the dust particle, where (x_i , y_i , z_i) are the coordinates of a matrix element of the dust particle's position, M designates the wire plane (M = 1, 2, 3, and 4 from top to bottom) in the instrument, and N is the index of the wire in one plane (N = 1, 2 . . . 9 with increasing coordinate).

For an arbitrary dust position (x_p , y_p , z_p) within the kernel, the induced charge on any electrode is calculated as a weighted average from the 8 adjacent matrix elements (corners of the enclosing cube):

$$Q_{M,N}(x_p, y_p, z_p) = \frac{\sum_{i=1}^{8} \frac{Q_{M,N}(x_i, y_i, z_i)}{|(x_p - x_i)(y_p - y_i)(z_p - z_i)|}}{\sum_{i=1}^{8} \frac{1}{|(x_p - x_i)(y_p - y_i)(z_p - z_i)|}} . \quad (3.1)$$

For dust positions on the plane (axis) of matrix elements, Equation 3.1 collapses into two-dimensional (one-dimensional) averaging from the adjacent four (two) matrix elements.

The kernel results can be extended over a larger volume defined by intervals x = [−10, 10] mm, y = [−10, 10] mm, z = [−20, 20] mm using the mirror-image symmetry properties with

respect to the planes $x = 0$, $y = 0$, and $z = 0$. For electrodes along the y direction ($M = 1$ or 3), the mirror image of the induced charges are calculated as

$$\begin{aligned} Q_{M,N}(x_p, y_p, z_p) &= Q_{M,10-N}(-x_p, y_p, z_p), \\ Q_{M,N}(x_p, y_p, z_p) &= Q_{M,N}(x_p, -y_p, z_p), \\ Q_{M,N}(x_p, y_p, z_p) &= Q_{5-M,N}(y_p, x_p, -z_p), \end{aligned} \tag{3.2}$$

where the exchange of the x and y coordinates in the last line means a rotation by 90 °. Similarly for the electrodes along the x direction ($M = 2$ or 4)

$$\begin{aligned} Q_{M,N}(x_p, y_p, z_p) &= Q_{M,N}(-x_p, y_p, z_p), \\ Q_{M,N}(x_p, y_p, z_p) &= Q_{M,10-N}(x_p, -y_p, z_p), \\ Q_{M,N}(x_p, y_p, z_p) &= Q_{5-M,N}(y_p, x_p, -z_p). \end{aligned} \tag{3.3}$$

Assuming that the DTS is an infinite periodic structure, the kernel results can be extended to the entire volume using translational symmetry (periodicity). Along the x and y directions this simply means $x \rightarrow x + mD$ and $y \rightarrow y + nD$, where $D = 20$ mm is the wire separation distance and m and n are integers. Along the z direction the translation $z \rightarrow z + kP$ (k is an integer and $P = 40$ mm is the separation distance between electrode planes) has to be accompanied by rotation of the frame by $k \times 90$ °.

3.5 Effect of Walls and Calibrations

The kernel results can be extended to the entire volume of DTS by its symmetry and periodicity properties, which have been discussed in the previous section. However, the DTS instrument is not an infinite periodic structure. When the dust particle approaches a grounded side wall, the entrance or exit grid, the applicability of the kernel results breaks down. In the

vicinity of a wall, a significant fraction of the dust charge is induced on the wall, which distorts the distribution of image charges on the electrodes.

First, we discuss the case of side walls. The effect of the wall increases with decreasing dust-wall distance and also with increasing distance to the nearest wire. The effect is most significant when the dust particle is exactly in between two electrode planes along the z-direction (see Figure 3.2). However, the induced electrode signals are the largest, when the dust particle is within an electrode plane. In this case, the wall effect is diminishing quickly with increasing distance from the wall. For a particle moving within an electrode plane, the difference of the induced charge signals with and without the wall effect is < 4% at distances > 40 mm from the wall. In summary we can state, that the electrode signals are distorted when the dust particle is passing near the sidewalls and this will lower the accuracy of the measurement. However, considering the geometry and the FOV of the DTS instrument, only a small fraction of particles will pass near the walls, and hence the effect of the sidewall is neglected in the present analysis.

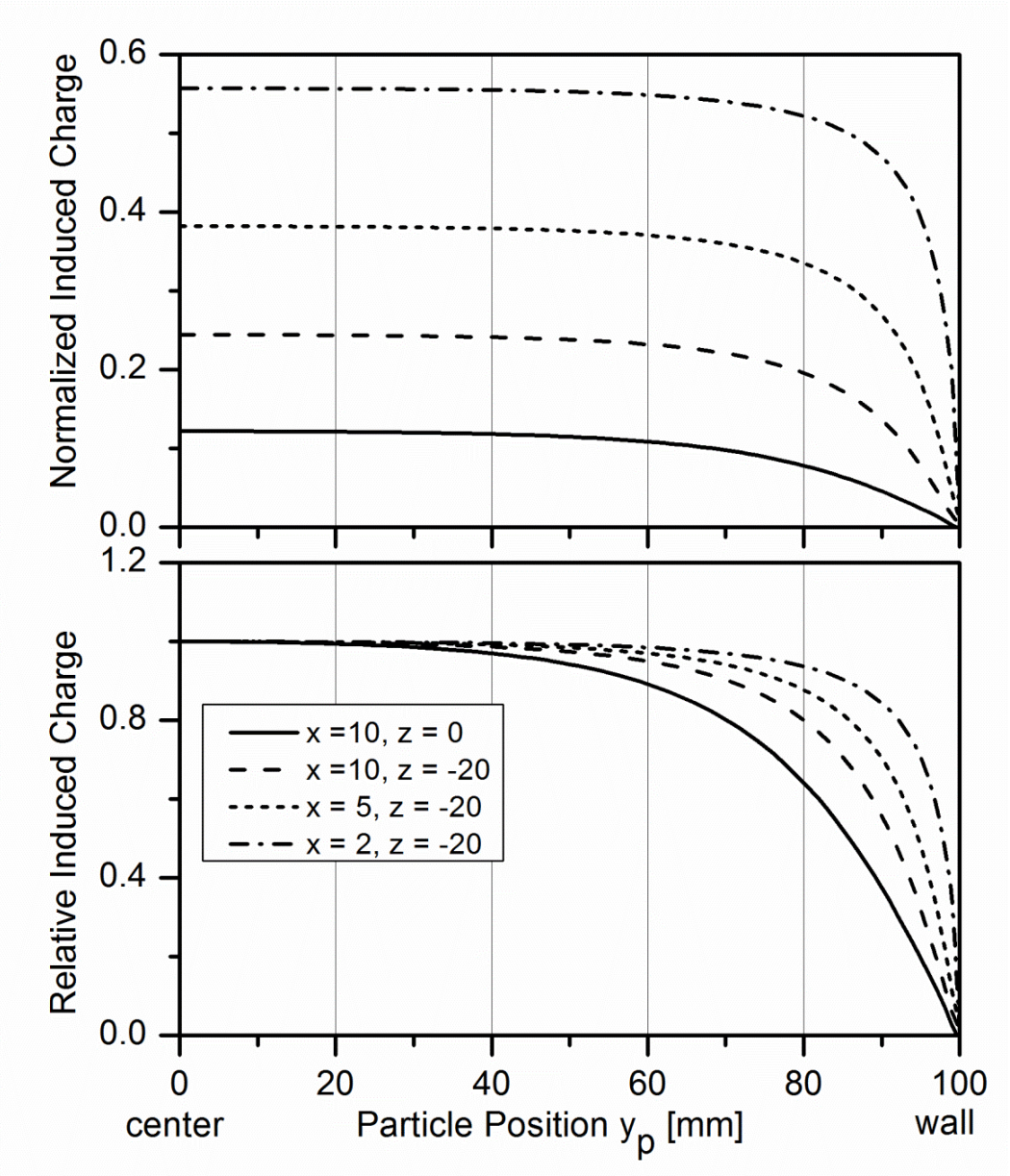

Figure 3.2: The effect of the proximity of a sidewall on charge ($Q_{3,5}$) induced on the closest wire that is located at (x = 0, y, z = −20). The upper panel shows the induced charge as a function of the distance from the wall for several different trajectories (x and z coordinates fixed, y varies). The effect of the wall is the strongest, when the dust particle is in between two electrode planes (x = 10 mm, z = 0 mm). The effect gets smaller when the dust particle is in the wire plane (z = − 20 mm), and gets even smaller when the dust particle is closer to a wire (x = 10 to 2 mm). The bottom panel shows the induced charge relative to the undisturbed kernel results.

Similarly, when the dust particle is close to the entrance or exit grids, the induced charge distribution on the wire electrodes is distorted. Every dust particle, however, has to pass through the entrance and exit grids and their effect cannot be ignored. When the particle is in the region between the entrance grid and the first electrode plane, defined by interval z = [60, 100] mm, the induced charges on the first plane $Q_{1,N}$ will be modeled using the kernel results (third plane $Q_{3,N}$) as:

$$Q_{1,N}(x_p, y_p, z_p) = Q_{3,N}(x_p, y_p, z_p - 2P) f(z_p) , \quad (3.4)$$

where $f(z_p)$ is a correction function with values $f(z_p = 100 \text{ mm}) = 0$, when the dust particle is in the plane of the entrance grid, and $f(z_p = 60 \text{ mm}) \approx 1$, when passing the first electrode plane, and P = 40 mm is the separation distance between electrode planes. The correction function is different for each unique dust trajectory. However, later analysis will show that this difference is small and, for simplicity, all dust signals will be corrected by the same function. The correction function $f(z_p)$ used in the present analysis is calculated from the ratio for a fixed trajectory between points (10, 10, 100) → (10, 10, 60):

$$f(z_p) = Q_{1,5}(10,10, z_p)/Q_{3,5}(10,10, z_p - 2P) , \quad (3.5)$$

where $Q_{1,5}(10, 10, z_p)$ is the actual numerical result with the wall effect included. The shape of the correction function is shown in Figure 3.3.

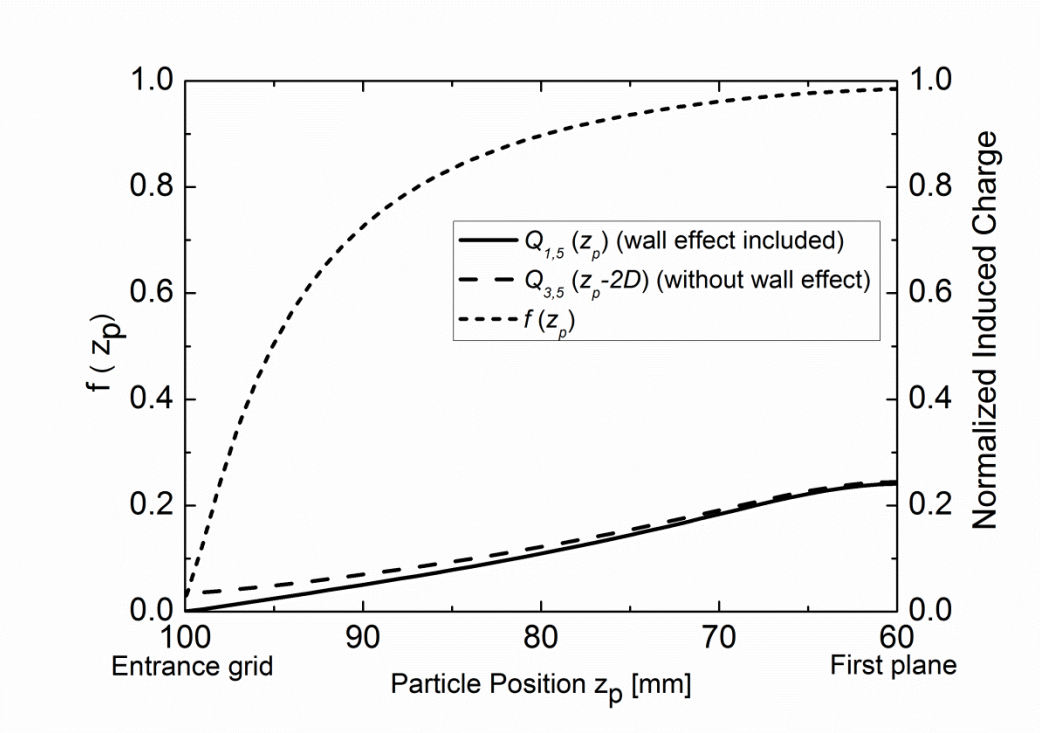

Figure 3.3: The effect of the entrance grid and the correction function f (z_p). The figure shows the induced charge on the nearest electrode as a function of distance, with and without the wall effect included. The ratio of the two calculations defines the shape of the correction function f (z_p). The correction for the effect of the exit grid is done similarly.

The correction function is different for each unique dust trajectory. Figure 3.4 shows the correction function for three typical dust trajectories. The function f (10, 10, z_p) is the same function in Figure 3.3. In this case, the dust particle is in between two wires in the first plane and thus the wall effect is the greatest. In the case of f (1, 1, z_p), the dust particle enters almost exactly on top of a wire electrode, and the effect of the grids is least significant. The third case f (5, 5, z_p) is in between the two other cases.

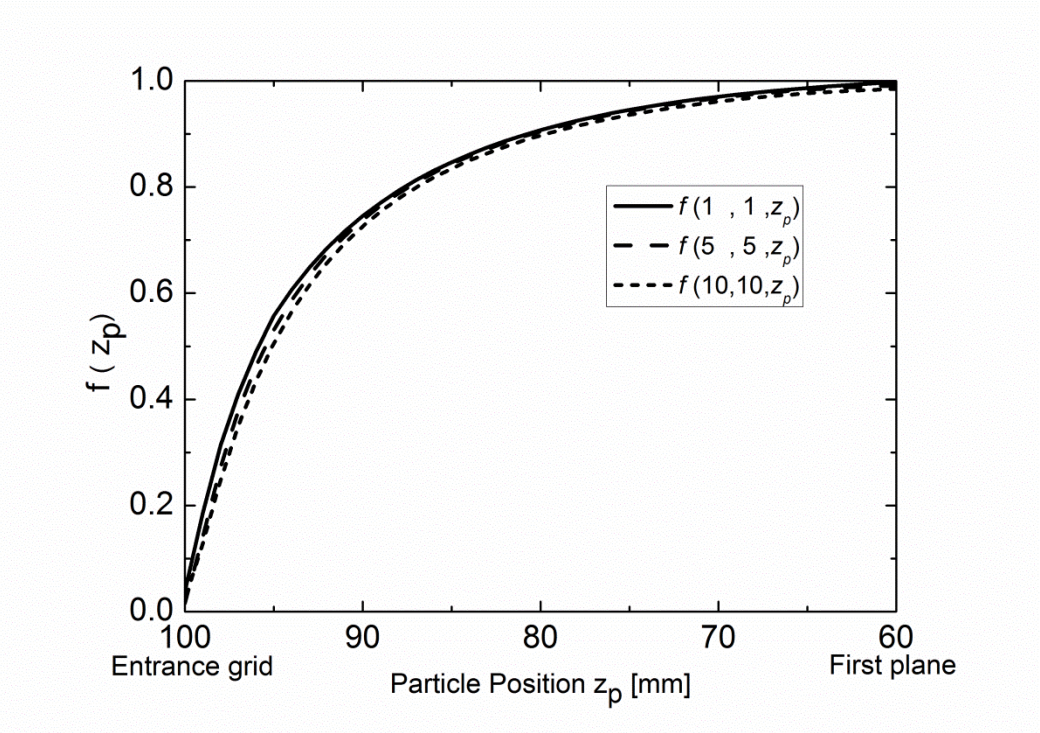

Figure 3.4: The effect of the entrance grid and the correction function f (z_p) for three typical trajectories. The difference in the correction functions for different dust trajectories is small; therefore all the dust particle trajectories are corrected by the same function f (10, 10, z_p).

3.6 Signal Characteristics

In this section, we present some of the typical characteristics of DTS signals. The model presented above is used to calculate the ideal induced charge signals on each electrode from a defined dust trajectory. For a high speed dust particle, its trajectory is almost a straight line in the DTS, which is fully defined by coordinates (x_{in} , y_{in}) and (x_{out} , y_{out}) on the entrance and exit grids, respectively. The actual signals are measured as a function of time that is related to the speed v of the dust particle through:

$$v = \frac{\sqrt{(x_{out}-x_{in})^2+(y_{out}-y_{in})^2+(z_{out}-z_{in})^2}}{t_{out}-t_{in}}, \qquad (3.6)$$

where t_{in} and t_{out} are timestamps corresponding to entering and exiting the instrument and $z_{out} - z_{in}$ = 200 mm is the distance between the entrance and exit grids. The velocity vector is fully defined by the speed and the two angles of incidence (θ_x in the *x*-*z* plane and θ_y in the *y*-*z* plane):

$$\theta_x = tan^{-1}\left(\frac{x_{out}-x_{in}}{z_{out}-z_{in}}\right),$$

$$\theta_y = tan^{-1}\left(\frac{y_{out}-y_{in}}{z_{out}-z_{in}}\right). \quad (3.7)$$

Figure 3.5 shows the schematic of the particle's trajectory when it passes through a wire plane. The plane crossing position *y* is defined as the distance from the nearest wire when the dust particle is in this wire plane; θ_y has been defined in Equations 3.7.

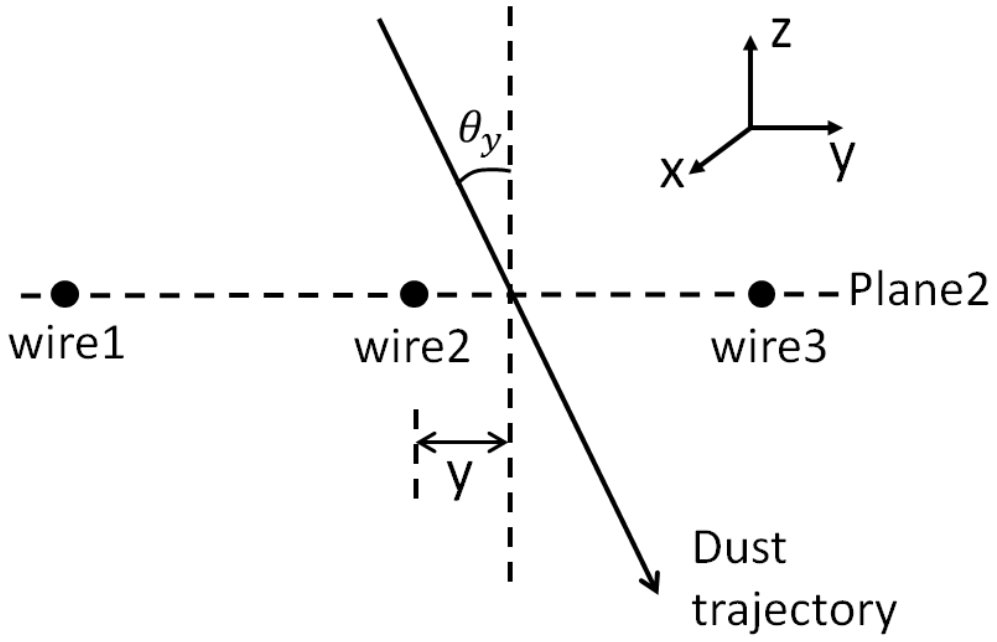

Figure 3.5: The geometry of a dust particle trajectory when particle is passing electrode plane 2.

Figure 3.6 shows the signals from the three electrodes with the strongest image charge signals in plane 2 for different plane crossing positions *y* and incident angles θ_y. Several observations can be made. (a) The charge signals diminish quickly with increasing distance, and the strongest signal is on the wire closest to the dust trajectory. (b) For cases, where the dust

grain passes very close to one wire (y = 1 mm, e.g.), there is a sharp increase of the signal intensity on that wire as the induced charge is concentrated there. At the same time, the signals on the other two wires exhibit a local minimum. It is interesting to note that these two signals are also similar to each other in shape and amplitude. This has an important implication for the analysis of the DTS data, as it may become difficult to decide on which side of the wire the particle passed by. (c) The maximum in the signal amplitude corresponds to the closest approach between wire and dust, and may not necessarily occur at the plane crossing. The closest approach may be different for different wires in the same plane and that explains the offset in the peak position (θ_y = 45 deg). Figure 3.7 shows an example of signals from the four planes for a given trajectory.

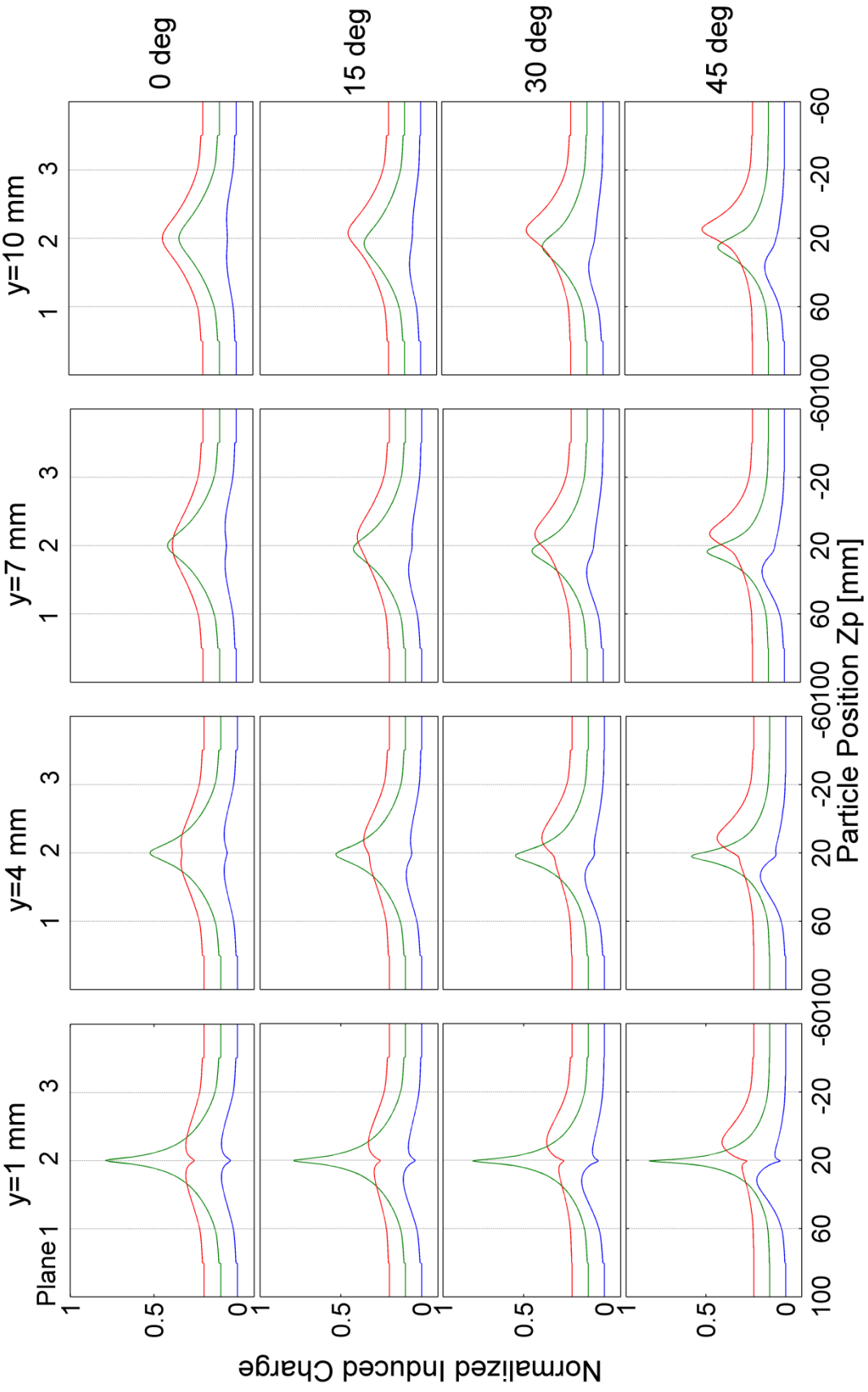
0 deg
15 deg
30 deg
45 deg
y=1 mm
y=4 mm
y=7 mm
y=10 mm
Plane 1
Normalized Induced Charge
Particle Position Zp [mm]

Figure 3.6: The largest three simulated induced charge signals on plane 2 from a dust particle with different plane crossing positions y = 1, 4, 7, and 10 mm, and different incidence angles θ_y = 0^o, 15^o, 30^o, and 45^o, $\theta_x = 0^o$. Signals for y > 10 mm can be derived from signals from 20 − y by using symmetry. The blue, green, and red curves correspond to wire1, wire2, and wire3 in Figure 3.5, respectively. The data are normalized to the dust charge, and the curves are staggered in the vertical direction for clarity. The vertical grids mark the positions of the three electrode planes.

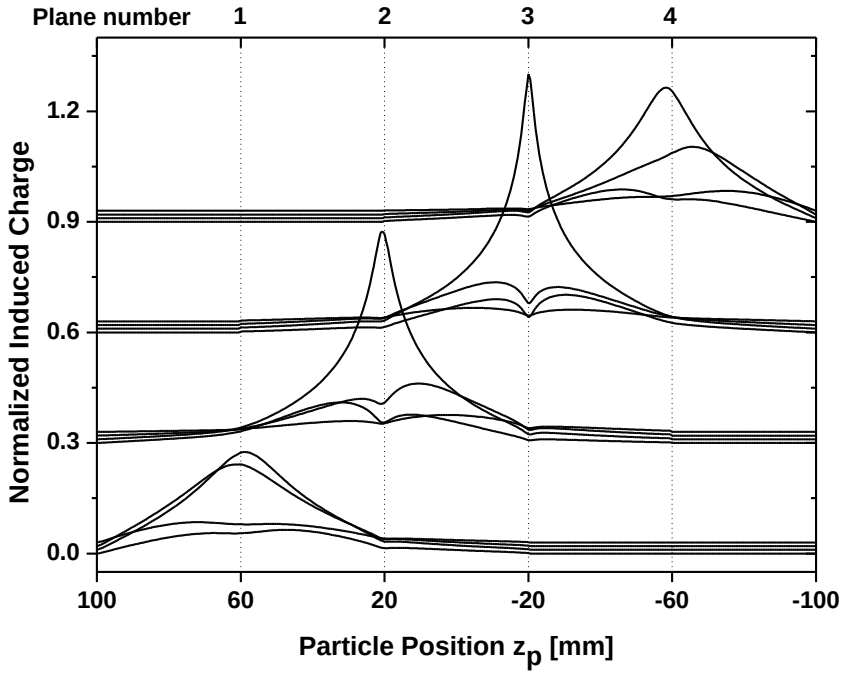

Figure 3.7: An example of simulated data showing the signals from the four electrodes closest to particle's trajectory in each plane. The calculations are done for a trajectory defined by entrance position (13, −22, 100) mm and exit position (−7, 38, −100) mm that corresponds to θ_x = −5.7 ° and θ_y = 16.7 °. The dust particle is passing planes M = 1, 2, 3, 4 at x_1 = 9, y_2 = 2, x_3 = 1 and y_4 = 28, i.e. 9, 2, 1, and 8 mm distance from the nearest wires, respectively. In plane M = 2 and 3, the dust particle passes through the wire plane very close to a wire and the signals look very similar to the signals for close passing in Figure 3.6. In planes M = 1 and 4 the dust particle passes approximately half way in between two wire electrodes.

4. DTS Data Analysis Algorithm and Experiment

4.1 Algorithm for Data Analysis

By comparing the DTS signals with numerical simulations of dust trajectories, it is possible to extract the grain's velocity and incident angle. The first step of the data analysis is identifying valid data among the many analog channels that are continually digitized and stored in transient recorders with buffer memory.

A trigger signal for freezing the memory and initiating data analysis can be derived from the DTS itself or an accompanying instrument. For example, when DTS is combined with a chemical analyzer instrument into a Dust Telescope, the dust impact signal is large and thus straightforward to identify. Auer *et al*. (2010) have presented a DTS self-triggering method. A simple digital filter covering a range of 1−128 km/s is applied to each electrode channel. The individual signals are fed into parallel amplitude filters for coincident detection on multiple channels. This method allows the high fidelity detection of even very small signals with QNR ≥ 6.25, and with a low false-event rate. After a trigger signal is obtained and the data are stored in the memory, a numerical data analysis is used to identify the 2 wires in each electrode plane that are the closest to the trajectory of the dust. The signals from these electrodes are then used for the calculation of the dust particle's velocity vector.

The DTS data analysis is based on finding the best fit between experimental data and simulations. There are 7 independent parameters, $\boldsymbol{P} = (Q, t_{in}, t_{out}, x_{in}, y_{in}, x_{out}, y_{out})$, which fully describe the trajectory within the DTS instrument and charge of the dust. The data analysis is performed in the following steps. (1) *Initial estimate of the parameters* $\boldsymbol{P_0}$. The amplitude ratio of the two electrodes with the largest signal in each plane gives a rough estimate of the 1-dimensional coordinate (x_1, y_2, x_3, and y_4) in each plane along with the charge, Q. In addition, the

timestamps when particle passes through planes 1 and 4 (t_1, t_4) are estimated. Together, the spatial coordinates, timestamps, and charge Q give initial estimate for $\boldsymbol{P_0}$:

$$x_{in} = \frac{3}{2}x_1 - \frac{1}{2}x_3\ , \quad x_{out} = 2x_3 - x_1\ ,$$
$$y_{in} = 2y_2 - y_4\ , \quad y_{out} = \frac{3}{2}y_4 - \frac{1}{2}y_2\ , \tag{4.1}$$
$$t_{in} = \frac{4}{3}t_1 - \frac{1}{3}t_4\ , \quad t_{out} = \frac{4}{3}t_4 - \frac{1}{3}t_1\ .$$

These relations are derived by computing the slopes of linear trajectories through the DTS with the geometry and coordinate system shown in Figure 3.1. The form of the equations ensures that all coordinate information can be derived from internal measurements only. (2) *Initial estimate of the range for each parameter* $\boldsymbol{\Delta P_0}$. The QNR is calculated as the estimated Q divided by the RMS of the noise from the electrode signals. The ranges for coordinates (x_1, y_2, x_3, y_4) are set as ±10 mm, and for charge Q, ±10%, which are much larger than the uncertainties of the estimations in step (1). For parameters t_1 and t_4, the range is calculated as $\Delta t = (t_4 - t_1) / 10$, accounting for incidence at an large angle when the signal peaks may not coincide with the time of the plane crossing (see Figure 3.6). (3) *Data fitting*. A Monte Carlo optimization process is used to find the best match between the measurements and simulations. Individual sets of parameters are randomly selected with each parameter from the corresponding range. The simulated signal for each parameter set is calculated and sampled at the same time steps as the experimental data. The goodness of the fit is characterized by the following parameter:

$$\chi^2 = \sum_N (D_j - S_j)^2\ , \tag{4.2}$$

where N is the number of data points, D_j is the j^{th} measured data point and S_j is the simulated data calculated in the same time steps as the measured data. (4) *Refining the fitting parameters*. The next step is determining an improved parameter set $\boldsymbol{P_1}$, which is closer to the real trajectory values. $\boldsymbol{P_{1,min}}$ is the one parameter set that corresponds to the minimum χ^2 value from the Monte

Carlo calculations performed in the step above. The behavior of χ^2 is analyzed individually for each fitting parameter for enhanced convergence. With six parameters fixed to values from $\boldsymbol{P_{1,min}}$, χ^2 is calculated as a function of only the remaining parameter. This typically yields a clear minimum and the parameter, where this minimum occurs, becomes the next best guess in $\boldsymbol{P_1}$. The procedure is repeated for the other six parameters. (5) *Reducing the range for the fitting parameters*. A new and narrower parameter range is then defined as $2\boldsymbol{\Delta P_0}$ /3, or $3|\boldsymbol{P_1} - \boldsymbol{P_0}|$, whichever is greater. (6) *Iterations*. Steps (3)–(5) are repeated in an iterative way until the desired accuracy of trajectory parameters is obtained or the χ^2 stops decreasing.

In step (3) *Data fitting*, because χ^2-minimum search is performed over a 7-dimensional parameter space, each iteration step requires a large number (~ 10^6) of Monte-Carlo tries that makes the data analysis computationally demanding. For faster analysis, only the signals nearest to the dust trajectory are considered (2 signals in each plane, 8 signals altogether). The Monte Carlo optimization always finds the position, which is closer to true parameters. Figure 4.1 shows the distribution of the χ^2 along one dimension of the seven parameters space. Only two of the seven parameters are shown here for simplicity: (a) charge Q and (b) x_3. There are 10^6 points in one iteration, but only the points with $\chi^2 \leq \chi^2_{min} + (\chi^2_{max} - \chi^2_{min}) \times 0.1$ are shown in the figure for clearly view. In Figure 4.1 (a), the points with small χ^2 are all around the real value, $Q = 1$. In figure (b), the true value is $x_3 = 97$ mm (3 mm away from the closest wire). Notice that there are two local minimums; one is around $x_3 = 97$ mm and the other is around $x_3 = 103$mm. When a dust particle is very close to one wire, the signals of the two the wires next to nearest wire are very small and similar to each other. Because of the noise, the code occasionally chooses the wrong minimum, which is discussed in more detail in Section 4.3.

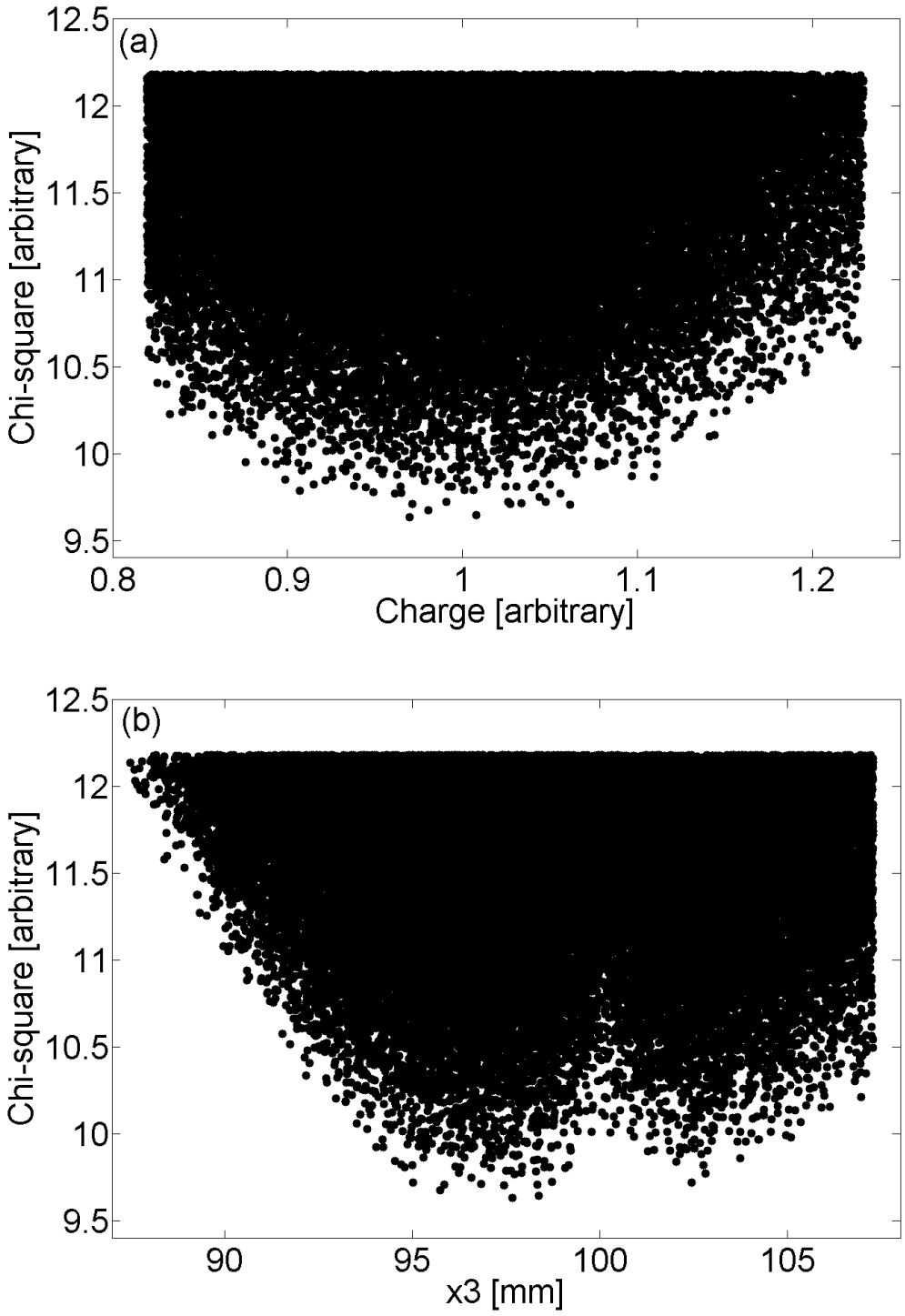

Figure 4.1: The χ^2 distribution along the one parameter Q (a) and x_3 (b) in the Monte Carlo optimization process in step (3). The Monte Carlo optimization always finds local minimum, which is closer to the true parameters in the seven-dimensional space (here Q = 1 and x_3 = 97

mm). The data analyzed are for an artificial signal with passing velocity v_z = 5 km/s and QNR = 10 (white noise). The dust particle moves from (−5.5, −10, 100) to point (32, −10, 100), which corresponds to $\theta_x = 10.62\,°$ and $\theta_y = 0\,°$. For more details about the artificial signal, see Section 4.2.

In step (4), *Refining the fitting parameters*, we find the $\boldsymbol{P_{1,min}}$ at first, which is the one parameter set that corresponds to the minimum χ^2 value from the Monte Carlo calculations. Then we fix the other 6 parameters, and χ^2 is calculated as a function of only the remaining parameter to find a new estimate of this parameters. Here, also for simplicity, only the results for two parameters Q and x_3 are shown in Figure 4.2. In part (a), when the other six parameters are around the real values, the χ^2 minimum for parameter Q appears near the true value, Q = 1. In part (b), there are once again two local minimums. That is why we need several iterations to make sure that the parameter falls to the right local minimum after vibrations.

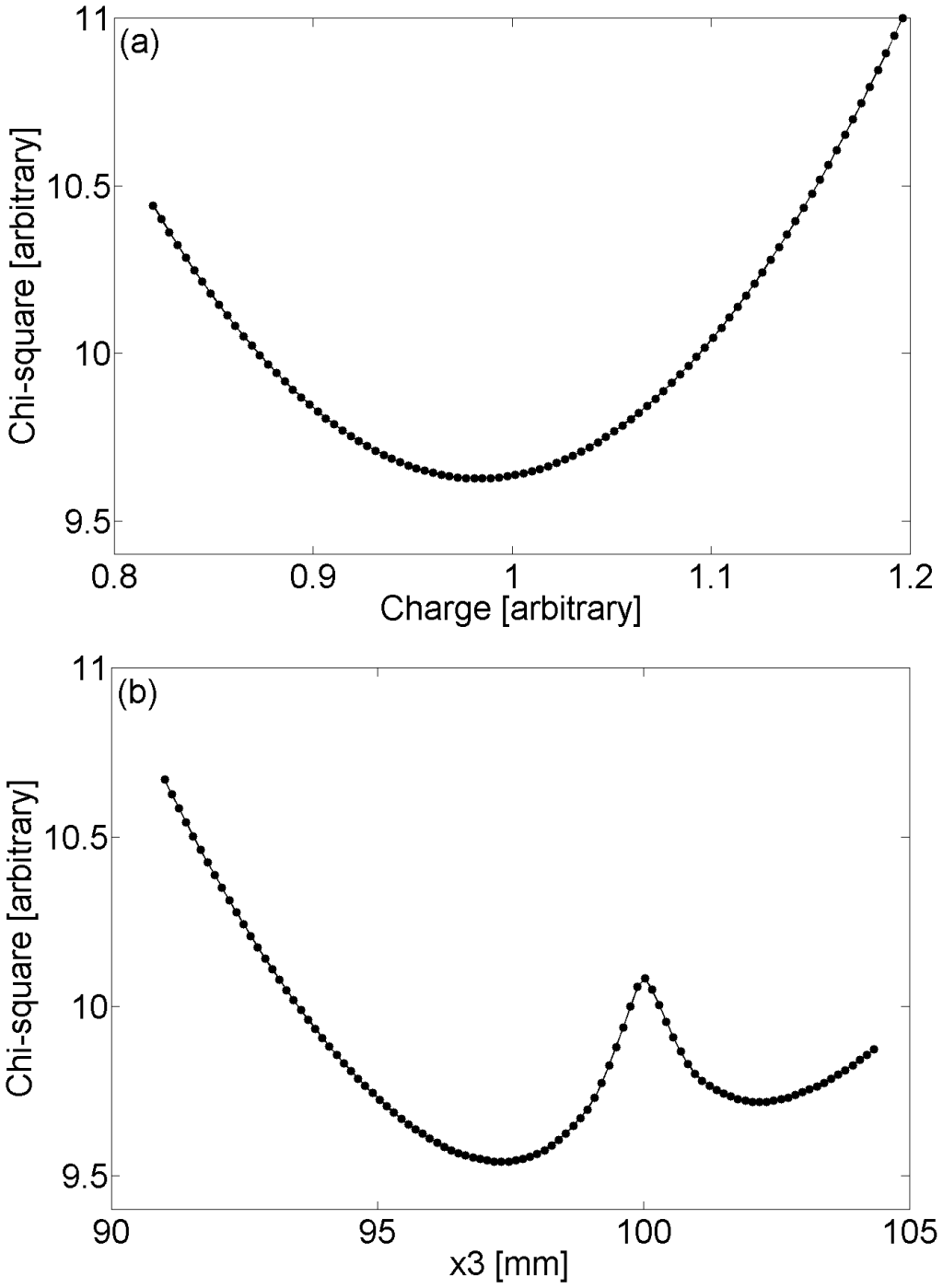

Figure 4.2: The χ^2 as the function of one parameter Q (a) and x_3 (b) when the other parameters are fixed in step (4). The new estimate of Q and x_3 are still close to the true results $Q = 1$ and $x_3 = 97$ mm.

Experience shows that ten or more iterations in step (6) are sufficient to reach the best possible trajectory information. After step (6) is finished, we get the desired solution. The analysis is repeated nine times, and the final result is the average of the nine solutions. Figure 4.3 shows the χ^2-minimum values in the 10 iterations for nine tries. The results show that the nine tries all converged to the same solution (fall into the same local minimum). Since the data analysis is a based on the Monte Carlo method, occasionally an iterative step does not produce a smaller χ^2-minimum value than the previous one. One such case is visible in Figure 4.3 (solid squares, iteration #5). In this case, the iterative step is ignored and the parameters in $\boldsymbol{P}$ and their ranges $\boldsymbol{\Delta P}$ are preserved from the previous step.

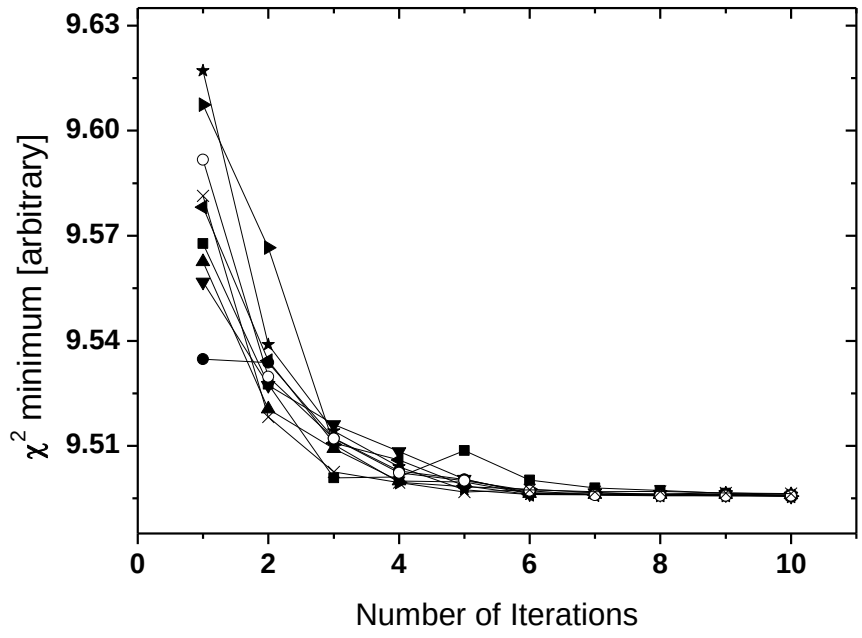

Figure 4.3: The convergence of the χ^2-minimum with increasing number of iteration steps. The different lines correspond to different data analysis runs.

4.2 Chi-square versus Cross-correlation

In the previous section, a χ^2-minimum method is used for the data fitting process, which finds the best match between the measurements and simulations. A Cross-correlation is another method that can be used for data analysis. After some analysis, we find that the χ^2-minimum and the cross-correlation get similar results, but the cross-correlation is less computationally expensive. Therefore, we select cross-correlation for later analysis.

The goodness of the fit between the simulated and measured signals is characterized by the cross-correlation coefficient SS, which is defined as:

$$ss = \frac{\sum_N (D_j \times S_j)}{\sqrt{\sum_N D_j^2} \times \sqrt{\sum_N S_j^2}}, \tag{4.3}$$

The denominator normalizes the convolution. If the two signals have the same shape and the time delay of the two is zero, then the cross-correlation coefficient equals unity. Since the cross-correlation method doesn't depend on the amplitude of the signals, the number of parameters is reduced from seven to six, (t_1, t_4, x_1, y_2, x_3, y_4). In step (3) *Data fitting*, the best match between the simulated and measured signals is only performed over a 6-dimensional parameter space, and each iteration step only requires 2×10^5 of Monte-Carlo tries, instead of 10^6 of tries in the χ^2-minimum method. Therefore, the cross-correlation method is much cheaper computationally. The charge Q is finally calculated using the χ^2-minimum method after the other six parameters have already been determined.

Numerical studies are performed to investigate which method has better accuracy. We use artificial signals to do numerical studies about the data analysis algorithm. The data algorithm is used to analyze the given artificial data, and the results are compared to the exact known parameters. If not specified, all the artificial signals mentioned in this thesis are simulated in the same trajectory: between entrance and exit points (−5.5, −10, −100) to (32, −10, 100). The incidence angles are θ_x = 10.62 ° and θ_y = 0 °, and the plane crossings occur at coordinates x_1 = 2,

$y_2 = -10$, $x_3 = 17$, $y_4 = -10$, i.e., 2, 10, 3, and 10 mm distance from the closest electrodes. This trajectory is representative for near-wire crossing in the x direction (x_1, x_3), and far-away-wire crossing in the y direction (y_2 and y_4). In this study, 40 μs transition time in DTS is used, i.e. v_z = 5 km/s. The assumed 10 MS/s sampling rate then yields roughly S = 400 data points for passing the instrument (400 mm path length). The charge is normalized to unity and random white noise with a distribution:

$$WN(x) = \frac{1}{\sqrt{2\pi\sigma^2}} e^{-\frac{x^2}{2\sigma^2}}, \tag{4.4}$$

is added to the data. The width of the distribution is related to the desired QNR as $\sigma = 1/\text{QNR}$.

The parametric study is performed for three different QNR ratios (6.25, 10, and 20). For each QNR value, nine different data sets are generated with different artificial noise added to the data. The two methods, χ^2-minimum and cross-correlation, are used for the analysis of the data to calculate the dust charge, Q, passing velocity v_z, and incident angles θ_x and θ_y. Figure 4.4 shows that the two methods provide essentially the same results, with the differences only due to the random characteristics of the analysis method. The consistency of the two algorithms also confirms the correctness of the algorithms.

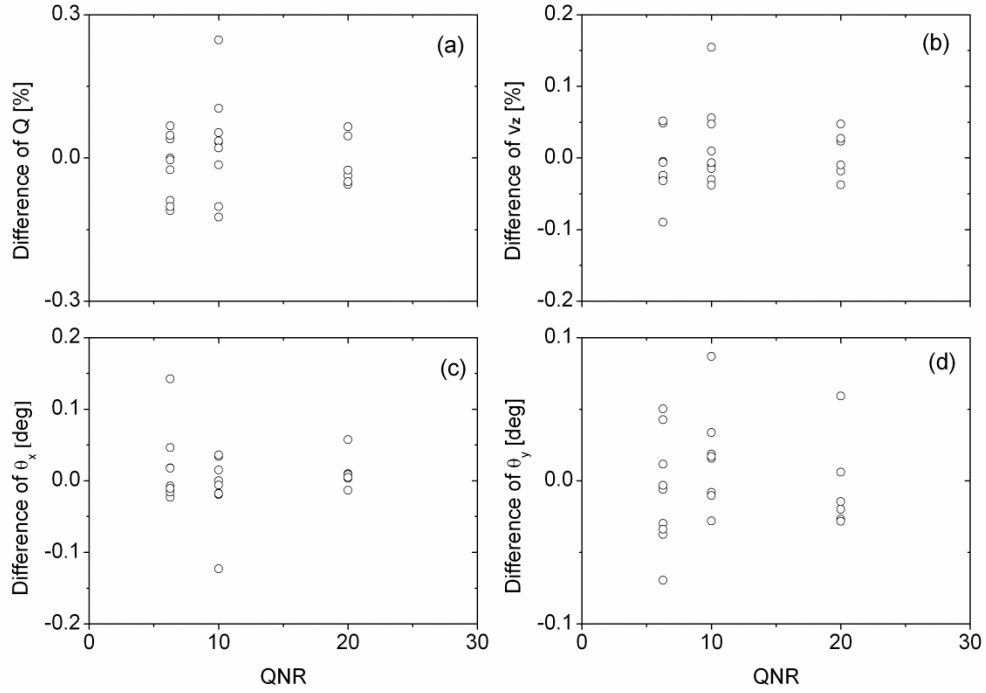

Figure 4.4: Results of the χ^2-minimum method minus the results of the cross-correlation method for artificial signals as a function of QNR. The difference is < 0.3% for charge, < 0.2% for speed, and < 0.2 °for angles.

4.3 Noise and Limited Sample Points on Uncertainty

The accuracy of the dust trajectory determination will decrease with decreasing QNR as the analysis is based on fitting the shapes and the amplitudes of the data. Furthermore, with increasing velocity, the number of useful data points from a dust particle transition will decrease. This is assuming that the CSA channels are sampled at the same rate (10 MS/s), independent of the velocity. A numerical study has been performed to investigate the effect of noise (QNR= 6.25, 10, 20, 50, and 100, see Equation 4.4) on the attainable accuracy of the measurements for different passing velocities (v_z = 5, 20, 40, and 80 km/s, which corresponds to sample points S = 400, 100, 50, and 25).

The parametric study is performed for a fixed artificial dust trajectory (More details in Section 4.2). The incidence angles are $\theta_x = 10.62\,°$ and $\theta_y = 0\,°$, and the plane crossings occur at coordinates $x_1 = 2$, $y_2 = -10$, $x_3 = 17$, $y_4 = -10$, i.e., 2, 10, 3, and 10 mm distance from the closest electrodes. This trajectory is representative for near-wire crossing in the x direction (x_1, x_3), and far-away-wire crossing in the y direction (y_2 and y_4). For each QNR and v_z value, nine different data sets are generated with different artificial noise added to the data. The algorithm described in previous section is used for the analysis of the data to calculate the dust charge Q, passing velocity v_z, and incident angles θ_x and θ_y.

First, we discuss the results when $v_z = 5$ km/s. Figure 4.5 shows the scatter of data caused by the added noise. For QNR ≥ 50, the scatter is minimal, and the analysis returns the correct values. With decreasing QNR, the scatter of the data increases.

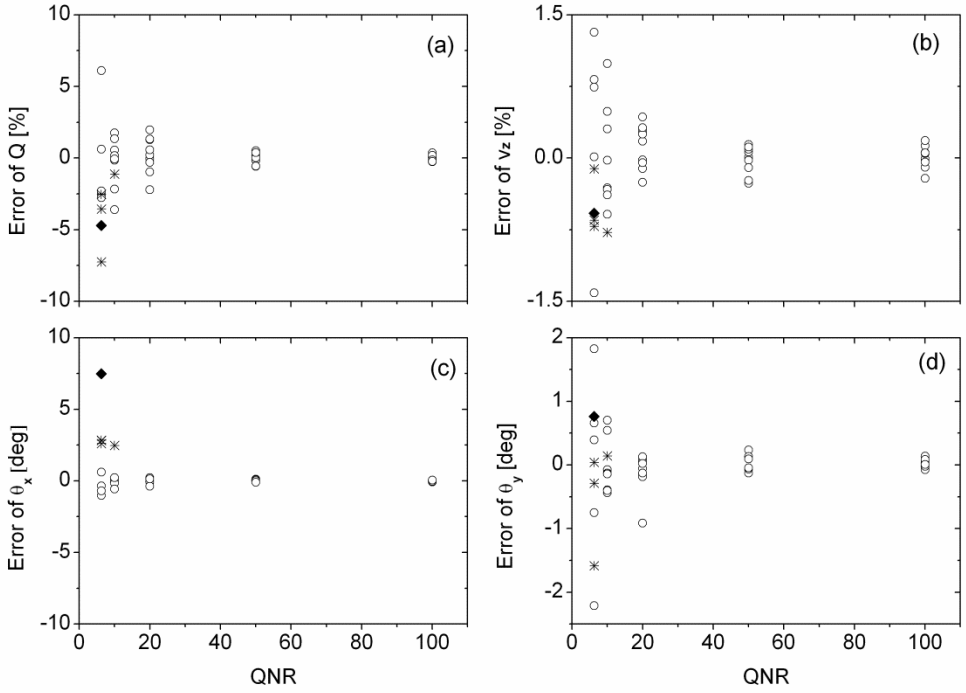

Figure 4.5: Errors of the parameters determined from the analysis as a function of QNR at v_z = 5 km/s. The five outliner points (one diamond and four asterisks) are discussed in details in the text.

At QNR = 10, the accuracy of the charge is approximately between −4 % to +3%. The accuracy of the velocity stays within approximately ±0.75 % for most cases and is distributed symmetrically around the correct value. The accuracy in the angle of incidence is better than 1 ° in general; however, there is one outlier point in Figure 4.5(c) designated by an asterisk symbol. The error is due to the incorrect determination of the *x*-coordinate in the first plane, where the dust particle is passing at a 2 mm distance from the closest electrode. In this case, most of the charge is induced on the closest wire and the signals on the two next-closest electrodes are relatively small and similar in both shape and amplitude (compare to y = 1 case in Figure 3.6). The added random noise makes it difficult to determine what side of the electrode the dust particles passed by, because the cross-correlation coefficient *ss* values (Equation 4.3) are similar

for both cases. The same thing happens in χ^2-minimum method. The analysis then incorrectly yields $x_1 = -2$ mm instead of $x_1 = 2$ mm, i.e., a 4 mm discrepancy, which translates into a $\Delta\theta_x \approx \tan^{-1}(4/80) = 2.86°$ error in the θ_x as observed in Figure 4.5(c), where the 80 mm is the distance between planes x_1 and x_3.

At QNR = 6.25, the accuracies of the parameters are still good for most cases. For the three outliers (asterisk symbols) around 2.8 ° in incidence angles θ_x, the same situation as above happened: the analysis incorrectly yielded $x_1 = -2$ mm instead of $x_1 = 2$ mm at plane 1. For the more distant outlier (diamond), not only is $x_1 = 2$ mm mistaken as $x_1 = -2$ mm at plane 1, but also $x_3 = 17$ is mistaken as $x_3 = 23$ due to larger noise. A 10 mm discrepancy corresponds to a $\Delta\theta_x \approx \tan^{-1}(10/80) = 7.13°$ error in the θ_x, which is consistent with observation. Because the dust particle passed through plane 2 and plane 4 as a far-away-wire crossing, the errors in θ_y are much smaller than θ_x at low QNR.

Next, we discuss the uncertainty at different QNR for v_z = 5, 20, 40, and 80 km/s. The uncertainty is calculated as the standard deviation of the errors for nine different tries for each QNR and v_z value. Figure 4.6 shows the uncertainty of dust trajectory determination for different QNR and v_z. For QNR $\geq$ 50, the uncertainties of the parameters are insensitive to QNR and velocity. For QNR $\leq$ 20, the uncertainty increases rapidly with decreasing QNR and increasing velocity. DTS is designed to measure high-speed dust particles in a range of 1-100 km/s. To keep the accuracy of the measurement, a higher sampling rate should be used instead of 10 MS/s.

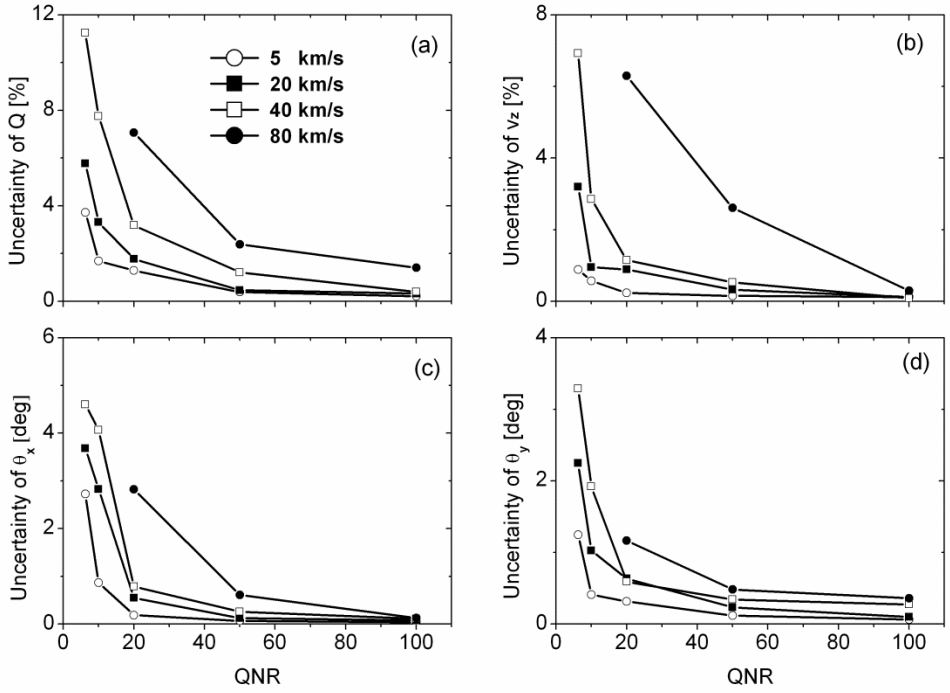

Figure 4.6: Uncertainties of charge Q, passing velocity v_z, incidence angle θ_x and θ_y for different QNR and v_z. The uncertainty is calculated as the standard deviation of the errors for nine different tries. When QNR $\leq$ 10 at v_z = 80 km/s, the code sometimes fails due to limited sample points and a high noise level. Therefore, there is no data for QNR= 6.25 and 10 for that speed.

4.4 Manufacture and Computer Simulation on Uncertainty

The attainable accuracy of the DTS instrument is limited by (a) charge on particle and the noise level of the CSA electronics (QNR), (b) sampling rate or dust particle's velocity, (c) accuracy of the computer simulation results, and (d) precision of the mechanical geometry of the instrument. Parts (a) and (b) are discussed together in the previous section. This section we discuss the effect of parts (c) and (d).

For the computer modeling, the errors in $\Delta q/Q$ are the following: configurations < 0.25%, particle size < 0.1%, model size < 0.1% and calibrations of the effect of the grids < 0.1% (Chapter 3). Thus the maximum error in $\Delta q/Q$ from the computer modeling is 0.55%. These error

sources should be independent of each other, which comes to a total uncertainty of $(0.25^2+0.1^2+0.1^2+0.1^2)^{1/2}$ % ≈ 0.30%. Simulations show that the 0.30% uncertainty in $\Delta q/Q$ corresponds to an uncertainty of 0.08 mm in one-dimensional coordinate (x_1, y_2, x_3, y_4), and a maximum error of 0.55% corresponds to 0.13 mm.

According to the geometry manufacturer, the mechanical tensioning and positioning of the wire electrodes is improved in DTS2 to provide better than ± 0.2 mm accuracy (Section 2.3).The uncertainty of the wire positions is independent of each other, thus the uncertainty Δz in z is $(0.2^2 + 0.2^2)^{1/2} \approx 0.28$ mm. The uncertainty of Δx (Δy) in x (y) is $(0.2^2+0.2^2+0.08^2)^{1/2} \approx 0.29$ mm, including the 0.08 mm uncertainty from the computer modeling. In this case, most of the uncertainty is from the uncertainty of the wire positions. For the speed v_z, the uncertainty is $\Delta v_z \approx \Delta z/3P \approx 0.2\%$, where $3P$ = 120 mm is the distance between the first and fourth electrode plane. For incident angles θ_x or θ_y, the uncertainty, $\Delta\theta_x$ or $\Delta\theta_y$, is about $\tan^{-1}(0.29/80) \approx 0.21°$.

In summary, when QNR is large (≥ 100), the uncertainty is mostly from the wire positions and computer modeling. When QNR decreases down to 20 and the sample points are limited, the uncertainty is mostly from the large noise level and limited sample points. At present, the accuracy of the DTS instrument is limited by the electronic noise and the wire positions.

4.5 Experimental Setup

The first DTS (DTS1) has been tested at the Heidelberg dust accelerator facility in November, 2010. Briefly, the accelerator uses a 2 MV Van de Graaff generator with a dust source mounted on the high voltage terminal. Prior to entering the experimental chamber, the dust particles transit a pickup-tube detector. The duration and amplitude of this signal are used for determining the particles velocity, v, and charge, Q, respectively. The mass is calculated from the relation, $m = 2QU/v^2$, where U = 2 MV is the acceleration voltage. Iron dust particles of a

spherical shape from a size distribution of approximately 0.2–5 microns were used for the measurements.

The DTS was mounted on a platform in the experimental chamber at the end of the beam-line (see Figure 4.7). The platform can be translated and rotated horizontally. Two sets of data were collected: one at approximately $0\,^{\circ}$ and one at $10\,^{\circ}$ orientation between the dust beam and the DTS normal direction. Measurements at different horizontal positions at each angle were taken in order to test the response of the various channels. The dust particles entering the experimental chamber were distributed over a 10 mm diameter spot, while the estimated angular uncertainty is $< \pm 0.1\,^{\circ}$, as defined by the geometry of the dust accelerator beam-line.

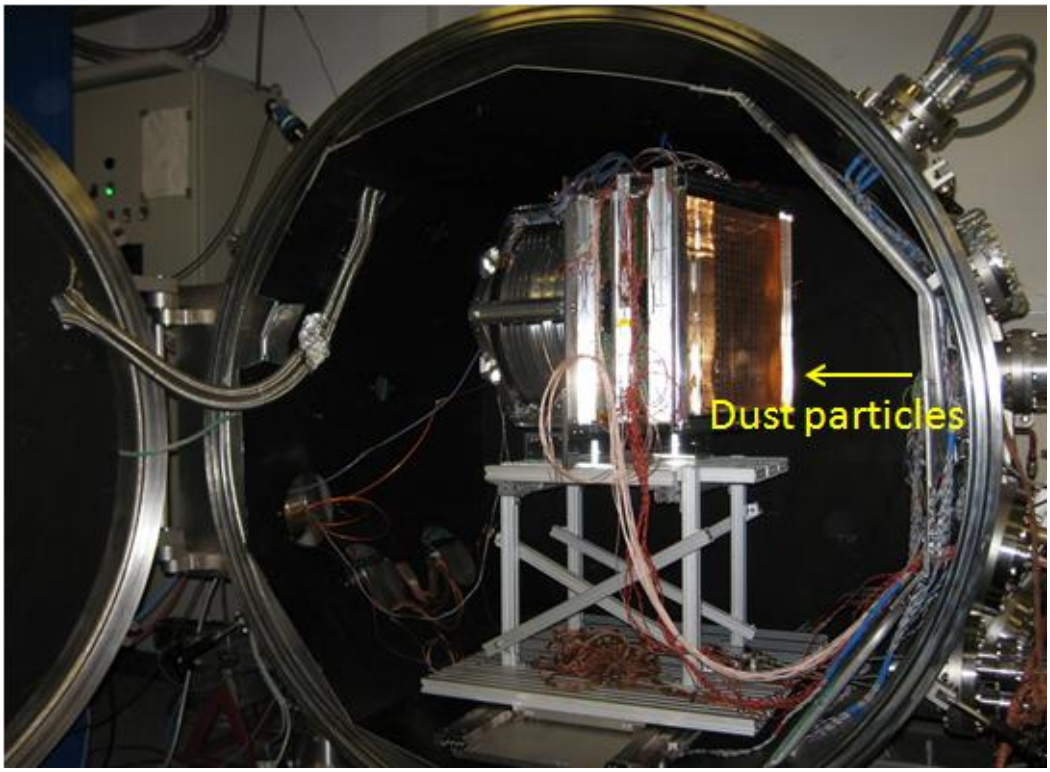

Figure 4.7: Experimental setup of the DTS testing at the dust accelerator facility in Heidelberg, Germany. The dust particles came from the right tube.

There were 32 active wire electrodes connected to CSAs in the DTS (8 in each plane). The rest of the wires were shorted to signal ground. The active electrodes were positioned symmetrically in one corner of the DTS and around the expected path of the dust particles. The 32 channel transient recorder ASIC chip was used for the recording of the DTS data. The ASIC had a 10 bit resolution over a voltage range of 0−1.8 V and was configured to operate at a sampling rate of 10 MS/s. The signal from the pickup-tube detector was used as an external trigger for the DTS data acquisition. The trigger signal stops the recording and all data were serially read out.

4.6 Results of High Speed Straight Trajectory

The recorded signals are analyzed as described above. The QNR varies approximately over a range QNR = 10−100. Figure 4.8 shows an example of a measured dust signal and the best fit of the data that yields the trajectory parameters.

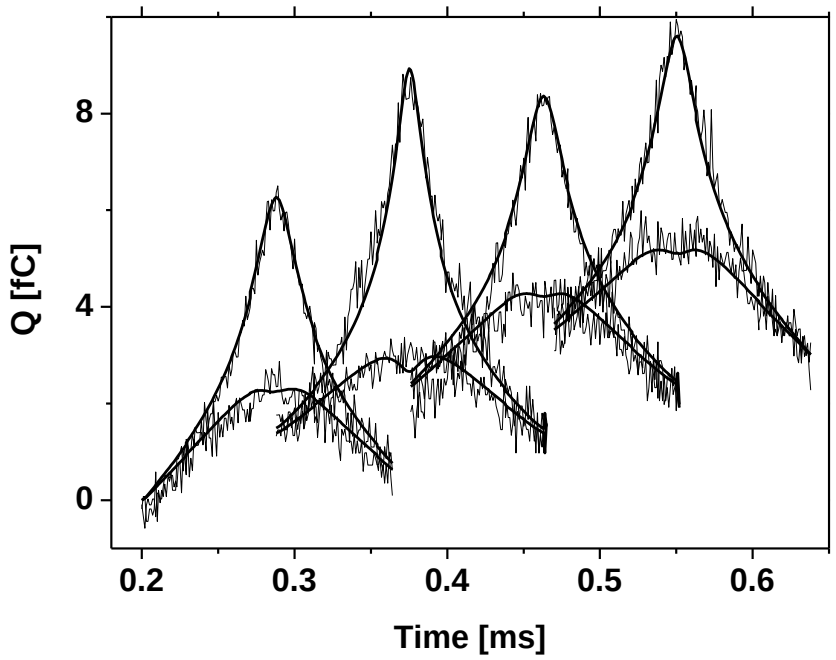

Figure 4.8: An example of DTS data and the best fit provided by the analysis (thick smooth lines). Signals from the eight electrodes closest to the path of the dust particle are shown. The calculated particle parameters are: Q = 15.77 fC, v = 4.57 km/s, θ_x = 0.086 ° and θ_y = 0.98 °. The curves are staggered in the vertical direction for clarity.

Figure 4.9 is the summary of the data analysis showing the charge, velocity and impact angles as a function of QNR. The calculated dust charge increases linearly with QNR, as expected. The small deviations from a perfect line are due to the fact that the QNR is calculated individually for each data set as an average of the noise from the eight electrode signals closest to the path of the dust. The noise levels on different electrodes can be slightly different and also show temporal variations. The dust charge values determined from the analysis are in good agreement with the calibrated pickup-tube measurements. Typically, the discrepancy is less than ± 5%, which is within the accuracy of the pickup-tube measurements. The velocity of the particles is in the range 2.5−5 km/s. The difference between velocity values calculated from the

DTS data and those measured by the pickup-tube detector is between 8.5−10.8%. This suggests a systematic error of approximately 9.6%. Unfortunately, due to the limited duration of availability of the dust accelerator facility for the testing of DTS, the source of this discrepancy has not been determined.

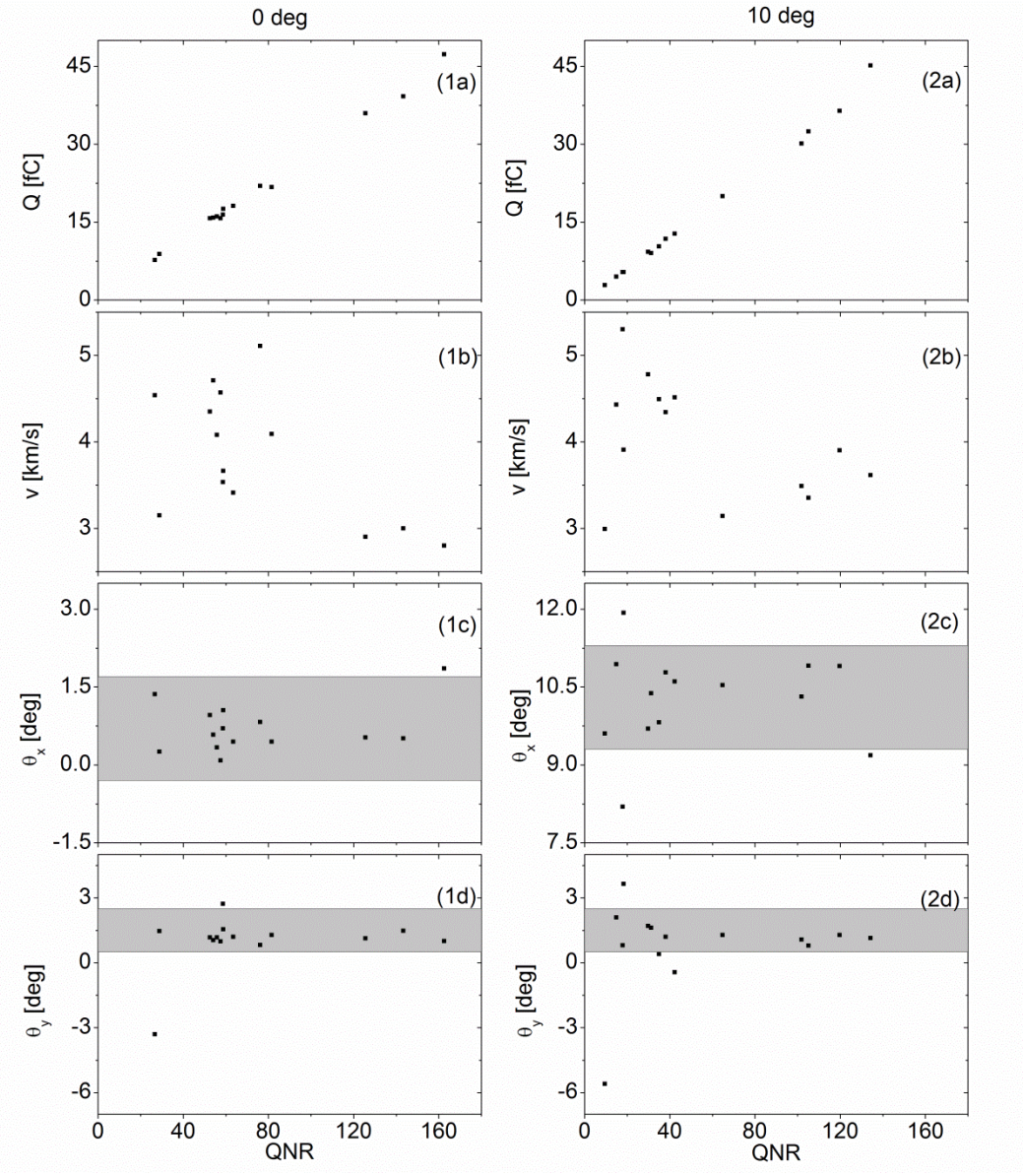

Figure 4.9: Results of analysis of the data for incident angle (1) 0 ° and (2) 10 °. (a) Charge, (b) Speed, (c) Incident angle θ_x, (d) Incident angle θ_y.

Since the dust particles from the accelerator are well collimated (< ±0.1 °), the spread of calculated angles of incidence is characteristic to the accuracy of the DTS laboratory model. The average values of the calculated angles are $\theta_x \approx 0.7°$ and $\theta_x \approx 10.3°$ for the two different orientations. In the vertical direction, the calculated incidence angle is $\theta_y \approx 1.5°$ for both cases. Generally, the spread of the data points is within ±1 °with the exception of a few outliners, which have been looked at in more detail. The outlining point in panel (1d) at QNR = 26.7 corresponds to a dust particle that passes planes at $y_2 = -17.74$ mm and $y_4 = -22.37$, i.e. at about 2 mm from an electrodes. As described in Section 4.3, in the case of near-electrode passing combined with low QNR, it is difficult to determine the side of the electrode, where the dust particle passed by. Assuming that this is the case, the error can be estimated as $\tan^{-1}(5/80) \approx 3.6°$, where 5 mm is the error made in the position determination in one of the planes and 80 mm is the distance between planes y_2 and y_4. It is important to note that the θ_x value of the same particle is still correct, i.e. the two components of the impact angle are calculated independently. The largest discrepancy of about 7 °occurred for the dust particle with QNR = 9.5 shown in panel (2d) of Figure 4.9. The inaccuracy is likely of similar origin and it is possible that the errors have been made on both the y_2 and y_4 planes, thus doubling the discrepancy in the angle of impact.

Based on the numerical analysis presented in Section 4.3, one would expect that the accuracy of the instrument is increasing with increasing QNR. However, there are two points outside the ±1 °accuracy with QNR = 162 and QNR = 134 in panels (1c) and (2c), respectively. Here too, the near-electrode pass could be the source of error. In the former case, the dust particle passed the x_3 plane at −19.12 mm, or 0.68 mm from the surface of the electrode, which results in weak signals on the two closest electrodes. If the particle indeed passed on the other

side of the electrode, i.e. at $x_3 = -20.88$ mm, then the error made in the analysis is $\tan^{-1}(1.76/80) \approx 1.26°$, which agrees with the observed discrepancy.

The laboratory testing presented here is limited to about 5 km/s dust velocity, while relative velocity of cosmic dust particles can extend well over 50 km/s. The laboratory tests are limited by access to the dust accelerator facility and relatively high noise of the CSA electronics integrated into the DTS prototype. The acceleration of dust particles to > 10 km/s is limited to submicron sized dust particles, which carry less charge and thus are more difficult to detect. The constructed laboratory prototype proved the concepts of DTS measurements. In order to extend the detectable size range to smaller dust particles, better electronics with lower noise needs to be developed and integrated into DTS.

5. Electrostatic Lunar Dust Analyzer (ELDA) Instrument

The DTS instrument measures the charge and velocity of individual dust particles. The mass *m* of a dust particle can be determined using a variety of methods. The mass can be measured from the amplitudes of the charge signals obtained from impact ionization when the impact speed *v* is known (Auer and Sitte, 1968; Dietzel *et al.*, 1972; Timmermann and Grün, 1991). Mass estimation is limited to a factor of about 6 – 10 because the amplitudes of the charge signals also depend on the particle's composition, density, and angle of incidence, which are generally unknown. Similarly, *m* can be determined from impact light flashes, thin-foil depolarization, or momentum transfer signals, using empirical relations when *v* is known (Auer, 2001). All of these methods are only applicable for high speed impacts and the dust particles are destroyed in the measurements.

Auer (1982) proposed a method to non-destructively determine the mass of a charged dust particle by bending its trajectory in a strong electric field. A particle's mass can then be derived from its charge-to-mass ratio, which is obtained by measuring the charge and the deflection of its path by a high-resolution trajectory sensor. The Electrostatic Lunar Dust Analyzer (ELDA) instrument uses this principle to measure particle mass. The ELDA has been developed for future lunar landing missions to detect slow-moving (1–100 m/s) charged dust particles near the lunar surface. The ELDA instrument simultaneously measures the charge, velocity vector, and mass of individual dust grains. The scientific motivation for the ELDA instrument is described in more detail in Section 1.1.3.

5.1 ELDA Description

ELDA consists of two DTS units with a deflection-field region (DFR) in between them, as shown in Figure 5.1. The DFR uses a high electrostatic field to bend the electrically charged

dust grain's trajectory. The two DTS units measure the charge and velocity vector of a dust particle before and after its trajectory is modified by the DFR (Auer, 1982). This arrangement allows for a precise measurement of the particle's trajectory deflection, which, in conjunction with charge information, is used to determine its mass.

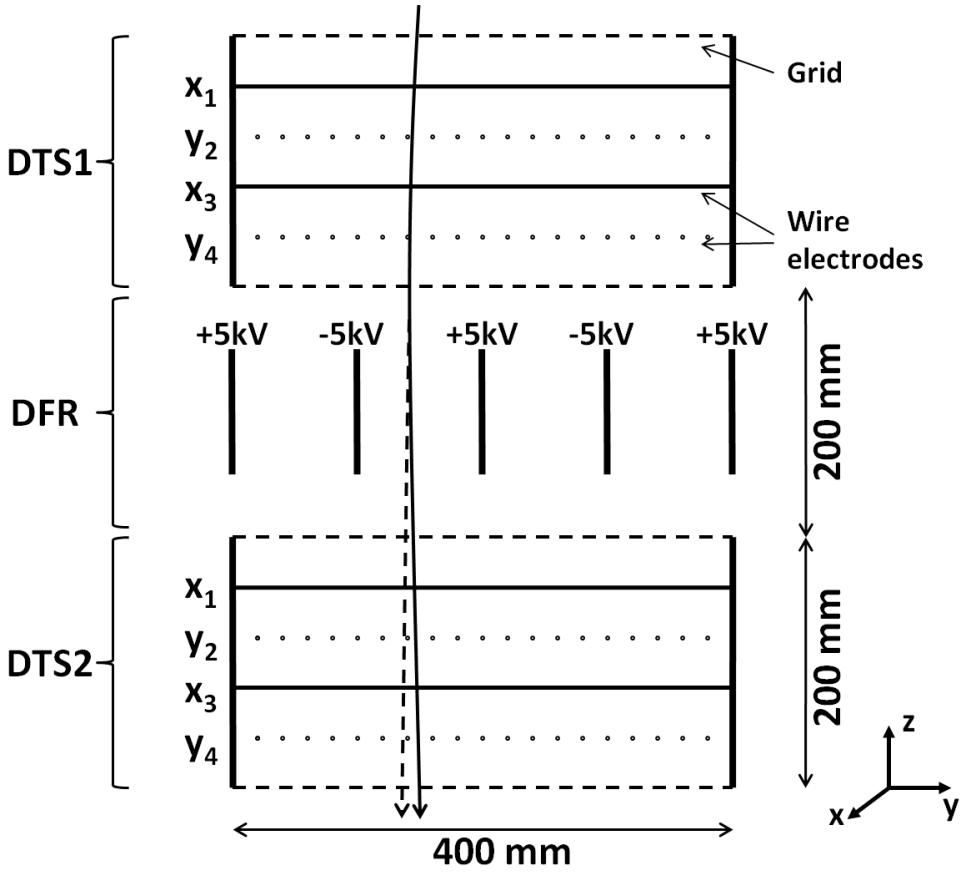

Figure 5.1: (To scale) Schematic of the Electrostatic Lunar Dust Analyzer (ELDA) instrument. The electrodes of the DTS are arranged in four planes (x_1, y_2, x_3, y_4) with alternating orientations in the x and y directions. The dust enters from the top and is deflected by the electric field in DFR in the y-direction (solid line). The dashed line indicates the trajectory without deflection. The DFR consists of pairs of plates biased to ± 5kV.

The DFR system consists of a set of biased plates with alternating polarities of +5 kV and -5kV (Figure 5.1). The plates are separated at 100 mm and the intensity of the generated electric

field is around 1×10^5 V/m. In general the electrostatic force experienced by a charged dust particle (and thus also the resulting deflection in the *y*-direction) depends on where the dust particle enters the DFR region, as the electric field is not entirely uniform. Duncan *et al*. (2011) have optimized the geometry of the DFR and found that a distance greater than 40 mm between the exit/entrance grid of the DTS and the biased plates is large enough to sufficiently reduce fringe field effects, maintaining a slowly varying deflection angle about $2\,^\circ$ for different entrance positions.

A laboratory prototype of ELDA was designed by Gemer and Drake, and was built using the two exiting two DTS units by Drake and Le in 2011 (Figure 5.2). For simplicity in testing, the DFR in the laboratory prototype consists only of one pair of electrodes biased at + 5 kV and − 5 kV. At each edge of the electrodes in the *x*-direction, a set of strip electrodes run in the *z*-direction to smooth the electric field. These strip electrodes are biased in equal voltage steps from +5 kV to -5 kV.

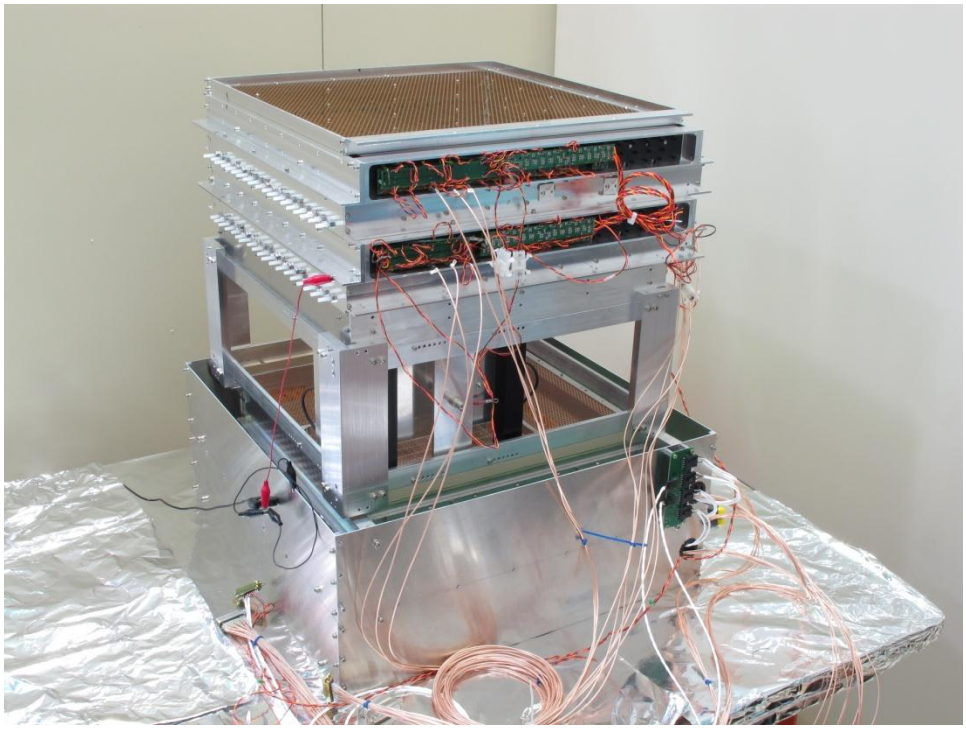

Figure 5.2: The laboratory prototype of ELDA. The overall dimensions are 400 ×400 ×600 mm.

5.2 DTS Data Analysis – with Gravity Included

The DTS data analysis algorithm for high speed dust particles has been discussed in Section 4.1 and 4.2. For slow-moving dust particles, the effects of gravity cannot be ignored, and causes acceleration during measurement and a deviation of the trajectory from a straight line. The same algorithm used to find the best fit between the experimental data and simulations is used for the slow-speed particles. In this case, the position and velocity information corresponding to the measured data cannot be calculated directly from the six parameters (t_1, t_4, x_1, y_2, x_3, y_4). The entrance point (x_{in}, y_{in}, 100), entrance timing (t_{in}), and entrance velocity (v_{x_in}, v_{y_in}, v_{z_in}) have to be calculated first. Here we will show how to calculate the entrance information from the six parameters (t_1, t_4, x_1, y_2, x_3, y_4) and the three components g_x, g_y, and g_z

of the acceleration vector due to gravity. Figure 5.3 shows the schematic of the six grids of the DTS and the corresponding position and velocity information of the dust particle.

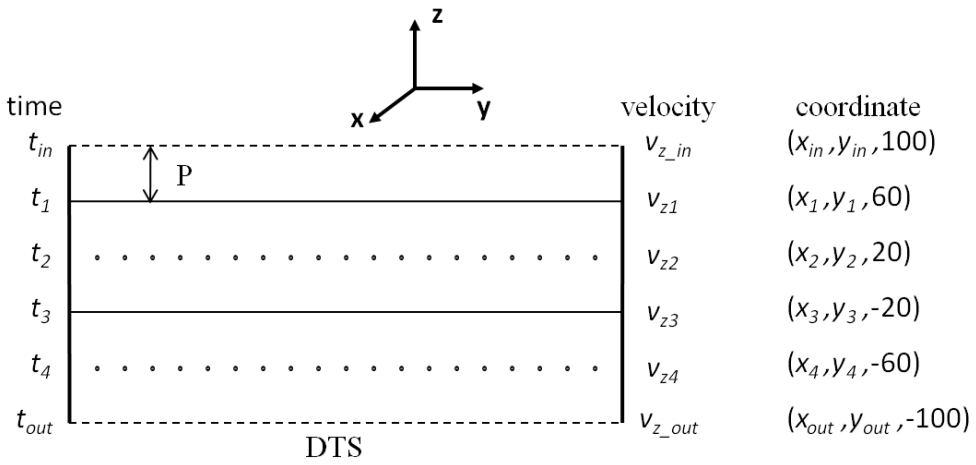

Figure 5.3: Schematic of the six grids of the DTS and corresponding time, position, and velocity information of the dust particle.

The DTS consists of an entrance grid, four planes of wires, and an exit grid. The spacing between them is *P*. The times when a dust particle passes through these six planes are given by t_{in}, t_1, t_2, t_3, t_4, and t_{out} respectively. v_{z_in}, v_{z1}, v_{z2}, v_{z3}, v_{z4}, and v_{z_out} are the *z* component of the velocity when the dust particle passes through the six planes, respectively. The *x*, *y* components of the velocity are denoted in a similar way.

First, we calculate the *z* component of the velocity when dust grain passes the six planes:

$$v_{z1} = \frac{3P}{t_4 - t_1} - \frac{1}{2} g_z (t_4 - t_1) , \qquad v_{z4} = \frac{3P}{t_4 - t_1} + \frac{1}{2} g_z (t_4 - t_1) ,$$

$$v_{z2} = \sqrt{v_{z1}^2 + 2 g_z P} , \qquad v_{z3} = \sqrt{v_{z4}^2 - 2 g_z P} , \qquad (5.1)$$

$$v_{z\_in} = \sqrt{v_{z1}^2 - 2 g_z P} , \qquad v_{z\_out} = \sqrt{v_{z4}^2 + 2 g_z P} .$$

Second, we determine the times the dust grain passed entrance grid, exit grid, plane 2 and 3:

$$t_{in} = t_1 - \frac{2P}{v_{z\_in}+v_{z1}}, \qquad t_{out} = t_4 + \frac{2P}{v_{z\_out}+v_{z4}},$$

$$t_2 = t_1 + \frac{2P}{v_{z1}+v_{z2}}, \qquad t_3 = t_4 - \frac{2P}{v_{z3}+v_{z4}}. \tag{5.2}$$

Third, we calculate the v_{x1} and v_{y2}:

$$v_{x1} = \frac{x_3-x_1}{t_3-t_1} - \frac{1}{2}g_x(t_3 - t_1), \qquad v_{y2} = \frac{y_4-y_2}{t_4-t_2} - \frac{1}{2}g_y(t_4 - t_2). \tag{5.3}$$

Fourth, we calculate the *x* and *y* components of the entrance velocity:

$$v_{x\_in} = v_{x1} - g_x(t_1 - t_{in}), \qquad v_{y\_in} = v_{y2} - g_y(t_2 - t_{in}). \tag{5.4}$$

Finally, we determine the entrance position (x_{in}, y_{in}, 100).

$$x_{in} = x_1 - \frac{v_{x1}^2 - v_{x\_in}^2}{2g_x}, \qquad y_{in} = y_2 - \frac{v_{y2}^2 - v_{y\_in}^2}{2g_y}. \tag{5.5}$$

5.3 Deflection Field Region (DFR) Modeling

The DFR is used to modify the dust particle's trajectory. The simplest approximation is to assume the electric field between the two plates is homogenous with a magnitude of *E*. If a dust grain enters the DFR along the *z*-direction with an entrance velocity (v_{x_en}, v_{y_en}, v_{z_en}) and an exit velocity (v_{x_ex}, v_{y_ex}, v_{z_ex}), the mass of the dust grain can be determined by

$$m = \frac{2QEl}{(v_{y\_ex}-v_{y\_en})(v_{z\_en}+v_{z\_ex})}, \tag{5.6}$$

where l = 100 mm, the dimension of the plate in the *z*-direction.

The actual *E*-field between the two plates is not uniform and has nonzero components in the *x* and *z* directions as well. A computer model built in COMSOL MULTIPHYSICS (COMSOL, Inc) was used to calculate the *E*-field distribution within the DFR using finite element method (FEM). The distribution of the electric field intensity is calculated for an array with 1 mm step size. The *E*-field intensity at an arbitrary point (x_p, y_p, z_p) is calculated from the weighted average of the 8 adjacent matrix elements (corner of the enclosing cube):

$$E_k(x_p, y_p, z_p) = \frac{\sum_{i=1}^{8} \frac{E_k(x_i, y_i, z_i)}{|(x_p - x_i)(y_p - y_i)(z_p - z_i)|}}{\sum_{i=1}^{8} \frac{1}{|(x_p - x_i)(y_p - y_i)(z_p - z_i)|}}, \quad (5.7)$$

where k means the x, y, z component of the E field. For dust positions on the plane (or axis) of matrix elements, Equation 5.7 collapses into two-dimensional (or one-dimensional) averaging from the adjacent four (or two) matrix elements.

Figure 5.4 shows equipotential lines of the voltage in the y-z plane, which is perpendicular to the biased plate electrodes. In the prototype of ELDA, the DFR consists only of one pair of electrodes biased at + 5 kV and − 5 kV. The pair of electrodes is not placed symmetrically in the structure (Figure 5.5), which in turn causes the equipotential lines to be asymmetrical.

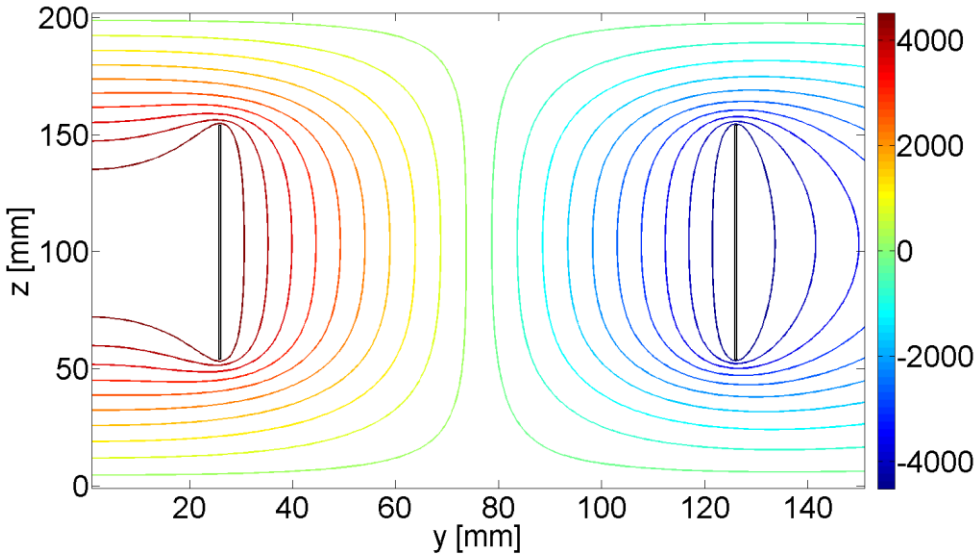

Figure 5.4: Equipotential lines of the voltage in the plane perpendicular to the biased plate electrodes. The lines are not symmetrical because the pair of plates is not symmetrically placed in the structure (Figure 5.5). The left plate is just 25 mm away from the edge of the instrument.

5.4 Mass Determination

The mass of the dust grain is calculated from the position and velocity change before and after the transition through the DFR. The initial value of the mass is estimated using Equation 5.6. The mass is then varied over a range around the initial value, and the trajectories in the DFR are calculated based on the measurement of DTS1, and compared to the measurement of DTS2. A fourth-order Runge-Kutta algorithm is used to solve the equations of motion within the DFR. The electric field intensity is calculated using Equation 5.7 and gravity is included in the net acceleration. Both the position and velocity information can be used to determine the match between the measurement and simulation independently. We found that the mass calculated from the velocity match provides more consistent and more accurate results.

5.5 Laboratory Test

The ELDA instrument was tested in the laboratory using particles with a narrow size distribution to evaluate its accuracy. ELDA was installed in a vacuum chamber as shown in Figure 5.5. The electrodes were 100 mm tall in the *z*-direction and spaced 100 mm apart in *y*-direction. The *z*-distance between the DFR electrodes and the DTS grids was 50 mm on both sides. The chamber was evacuated to $< 10^{-6}$ Torr. A dust dropper was mounted 590 mm above the entrance grid of the ELDA and the dust particles were dropped into the instrument. The dust dropper consisted of an electromagnetically agitated thin gold-plated disk with an aperture in the center, following the design by Walch *et al.* (1994). A small amount of dust was loaded on the disk and the falling particles were triboelectrically charged by contacting with the disk's surface (Sternovsky *et al*., 2001, 2002). The charge can be either positive or negative, depending on the disk material and triboelectric processes.

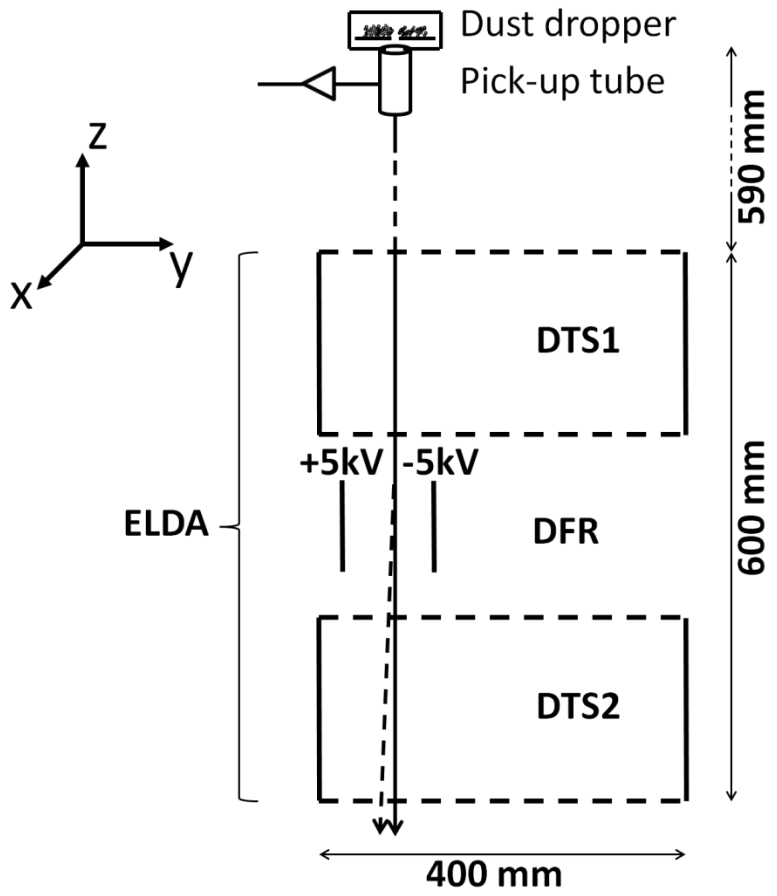

Figure 5.5: Laboratory test setup of the ELDA instrument inside the vacuum chamber. Charged dust particle were dropped from the top of the vacuum chamber, through DTS1 and deflected in the DFR, which consisted of a pair of plate electrodes. DTS2 measured the resulting trajectory.

The particles used were monodisperse (Catalog Number: DC100, Duke Scientific Corporation) with an average diameter d = 108 ± 4 μm and a standard deviation σ = 9.8 μm (Figure 5.6). The microsphere composition is polystyrene divinylbenzene (4-8%) with a density of 1.05 g/cm^3.

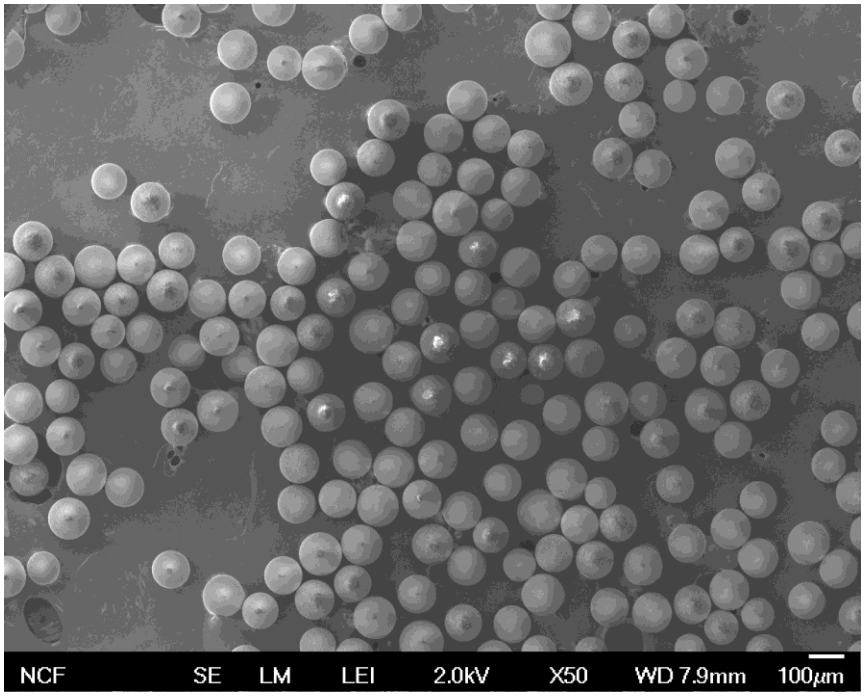

Figure 5.6: Scanning Electron Microscope (SEM) image of the dust sample used in the experiments (provided by Shu). The size distribution is consistent with the parameters provided by the manufacturer.

There were 32 active wire electrodes connected to CSAs in the two DTS units: three per plane in DTS1 and five per plane in DTS2. The active wire electrodes were positioned close to the expected path of the falling particles. The remaining wires were grounded for simplicity. A 32-channel data acquisition card with a 16 bit resolution was used for data recording. The sampling rate was 5 kS/s for each channel. A pick-up tube detector, connected to a CSA and installed underneath the dust dropper, was used to trigger the data acquisition.

5.6 Result

The magnitude of the dust charge varies between 0.18 - 1.92 $\times 10^{-13}$ C with an average value of 0.56 $\times 10^{-13}$ C. The corresponding range of charge-to-mass ratio (Q/m) is 2.6 - 27.7 $\times 10^{-5}$ C/kg, where $m = 6.93 \times 10^{-10}$ kg and is calculated from the average dust size d = 108 μm and a density of ρ = 1.05 g/cm^3. The corresponding surface potentials are 3 - 32 V. The Q/m ratios

from above are within the region of parameter space that is measureable by the ELDA, which will be discussed in detail in the error analysis. From a total of 68 particles, 43 were charged negatively. The magnitudes of charges were similar in both the positive and negative cases.

The charge-to-noise ratio (QNR) is calculated individually for each particle measurement based on the noise from the eight electrodes signals used for the dust's trajectory analysis. The noise varies slightly from electrode to electrode and shows some variation with time. The QNR varies approximately between 120 - 1400 for DTS1 and 170 - 2800 for DTS2, which has a lower noise level overall.

Gravity information is needed for the data analysis. In this experiment, the ELDA instrument was installed in a vertical position (Figure 5.5) and we use $g = 9.796$ m/s^2 along the z-direction.

Figure 5.7 shows an example of dust signals from DTS2 and the best fit yielding the velocity information. The signals on planes 1 and 3 are similar as there is no deflection in the x-direction. The signals of planes 2 and 4 differ because of the deflection in the y-direction.

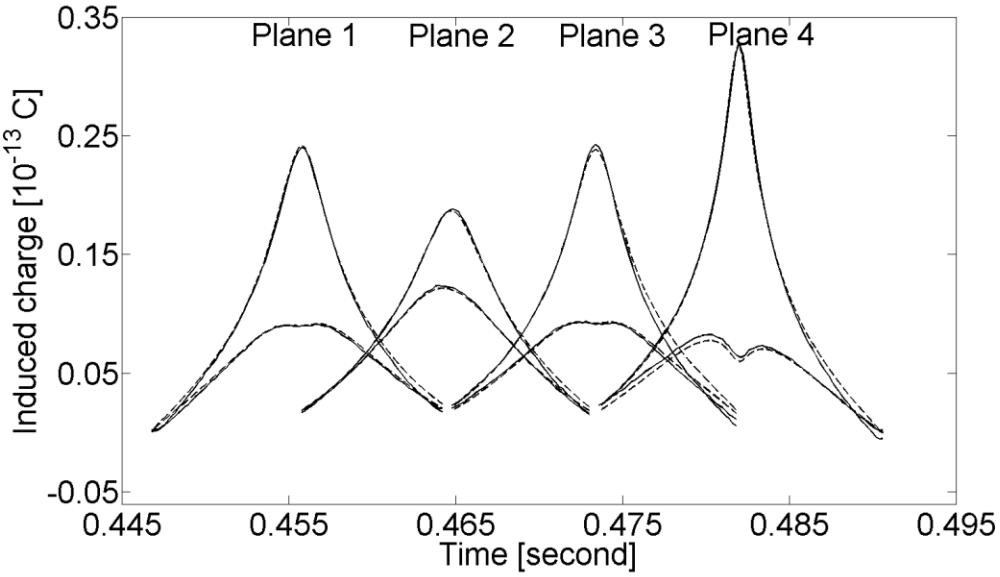

Figure 5.7: A data set from DTS2 recorded with the DFR high voltage on (solid lines). For each plane, the signals from the two wire electrodes closest to the path of the dust trajectory are shown. The fitted charge $Q = 0.62 \times 10^{-13}$ C. Gravity accelerates the particle in the *z*-direction and thus the velocities at the entrance (4373 mm/s) and exit (4800 mm/s) are slightly different. The dashed lines represent the best fit from the analysis.

5.6.1 Result of E = 0

Two tests were conducted; one with the DFR electric field on, and one with it off. With the electric field off, the dust particles pass though the ELDA instrument with a simple free-fall motion. Upon release from the dust dropper, the particles may start with a small initial velocity with both horizontal (*x* and *y*) and vertical (*z*) components. This velocity is random in direction and is typically on the order of 10 mm/s. Independent measurements from the two DTS units can be used to evaluate their relative measurement accuracies in speed and angle, and also determine the accuracy of the ELDA geometry (distortion). The latter is important, as the distortion of the ELDA instrument is small and may be difficult to measure otherwise.

The two DTS units provide independent measurements of the velocity vector and these results can be used to predict velocity at other positions. For example, the exit velocity, defined

at the point of crossing the bottom grid of ELDA, is 4798 - 4808 mm/s calculated from DTS1 and 4814 - 4842 mm/s from DTS2. The slightly larger values measured by DTS2 are likely due to geometric imperfections (displacement) in the ELDA instrument, which are due to its prototype nature. When predicting the exit velocity from DTS1, the mechanical dimensions of ELDA are used. The measurement of dimension has a ~ 1 mm error, which affects the velocity calculation. We note that the discrepancy is still < 0.5%, and is within the claimed speed measurement uncertainty of DTS < 1%.

The accuracy of the angle measurements of DTS can be calculated by tracing back the trajectories to the plane of the dust dropper. The trajectories of all particles should converge to the orifice, which defines the starting position and is measured to < 1 mm uncertainty. The dispersion of the predicted starting positions provides the error of the DTS in angle measurement. The standard deviations of the starting positions predicted by DTS1 are σ_x = 2.21 mm and σ_y = 2.95 mm, which corresponded to 0.18 ° and 0.25 ° errors in the respective angle measurements. Similarly, the deviations from DTS2 are σ_x = 4.38 mm and σ_y = 4.78 mm, corresponding to 0.28 ° and 0.31 ° errors.

It appears that DTS1 provides more accurate angular information than DTS2, despite the lower noise levels in the latter. Further investigations show that the CSA electronics in DTS2 are more prone to low-frequency noise, which essentially biases the signals. Since the position of the dust within one plane is greatly determined by the ratio of the signals from the two neighboring wires (see Figure 5.7), a small bias voltage can cause large errors in the data analysis. Low frequency signals are more difficult to filter out digitally since the length of the recorded signal is finite due to limited available memory. Digital high-pass filters, which would remove the low-frequency bias signal, may introduce distortion to the signal shape and lead to other errors.

Figure 5.8 shows the estimated error in one-dimensional coordinate measurement (x_1, y_2, x_3, y_4) as a function of the signal voltage offset. The calculations are done for different plane crossing positions, where the dust particle passes through the two wire electrodes. An error $\Delta\theta$ in angle measurement corresponds to error $tan\ (\Delta\theta) \times 2P$ in position measurement, where P = 40 mm is the distance between two neighboring electrode planes. The 0.31 ° angle measurement error in DTS2 corresponds to a 0.43 mm error in position measurement in $y_4 - y_2$. A bias of 0.01 (1% of the total charge Q) can cause an uncertainty of ~ 0.4 mm in $y_4 - y_2$. The uncertainty introduced by the bias in Q is 2 × bias (2%). Including the uncertainty < 1% without bias for QNR > 100 (Section 4.3), the total charge uncertainty in this test is < 3%. The bias has no effect in time measurements (t_1, t_4), thus no effect in the measurement of the passing velocity v_z. The conclusion from these findings is that attention needs to be paid to the noise spectrum of the CSA electronics, as low-frequency noise can lead to errors in the velocity vector measurements in x-y direction.

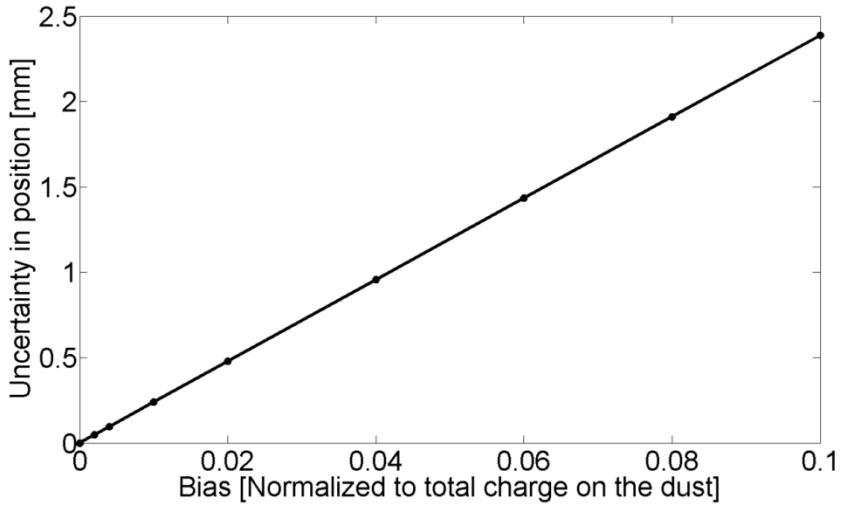

Figure 5.8: The estimated uncertainty in parameters (x_1, y_2, x_3, y_4) introduced by the voltage bias of the CSA electronics. The uncertainty is calculated using artificial data for dust particle passing through one wire plane for different plane crossing positions and incidence angles.

The position where the dust particle exits the ELDA instrument can also be calculated using both DTS1 and DTS2. The statistical distribution of the exit positions enables us to evaluate the relative positioning accuracy of the two DTS units. We find that DTS1 is displaced by x_d = 3.17 mm and y_d = 1.78 mm relative to DTS2. This evaluation also yielded two different values for the deviation from the horizontal positions of the DTS units. For DTS1, the deviations are $0.069°$ and $-0.199°$ in the x and y-directions, while for DTS2 these values are $0.017°$ and $0.148°$.

The relative tilts and displacements are the result of assembling the ELDA instrument from two discrete DTS units and the DFR. A flight instrument can be built with better precision; nevertheless, the data analysis for $E = 0$ is both useful and necessary to evaluate the instrument's accuracy. The results of $E = 0$ allows determination of the direction of the gravitational acceleration after the instrument is deployed on the lunar surface, for example. One limitation of this method is that it requires the detection of a statistically significant number slow moving ($\leq$ 10 m/s) dust particle, for which the gravitational acceleration within the instrument causes a measurable deviation from a straight-line trajectory.

5.6.2 Result of $E > 0$

With the high voltage bias potentials in the DFR on, the recorded data are analyzed as described in Section 5.2-5.4 and the mass of the dust particle is calculated. The displacements and tilt determined in the previous section are included in the calculations. Due to the electrode structure in the DFR, the z-component of the E-field is not zero. Depending on the position of the transition and the polarity of the dust charge, the dust particles can be slightly accelerated or decelerated in the z-direction by the E-field.

The dust particles used in the experiment are monodisperse and have an average diameter $d = 108 \pm 4$ μm, with a standard deviation $\sigma = 9.8$ μm. The mass distribution measured by ELDA is converted to a size distribution using a density of $\rho = 1.05$ g/cm^3, and is compared to the distribution provided by the manufacturer. The measured average diameter $d = 109$ μm and deviation $\sigma = 11.8$ μm (see Figure 5.9).

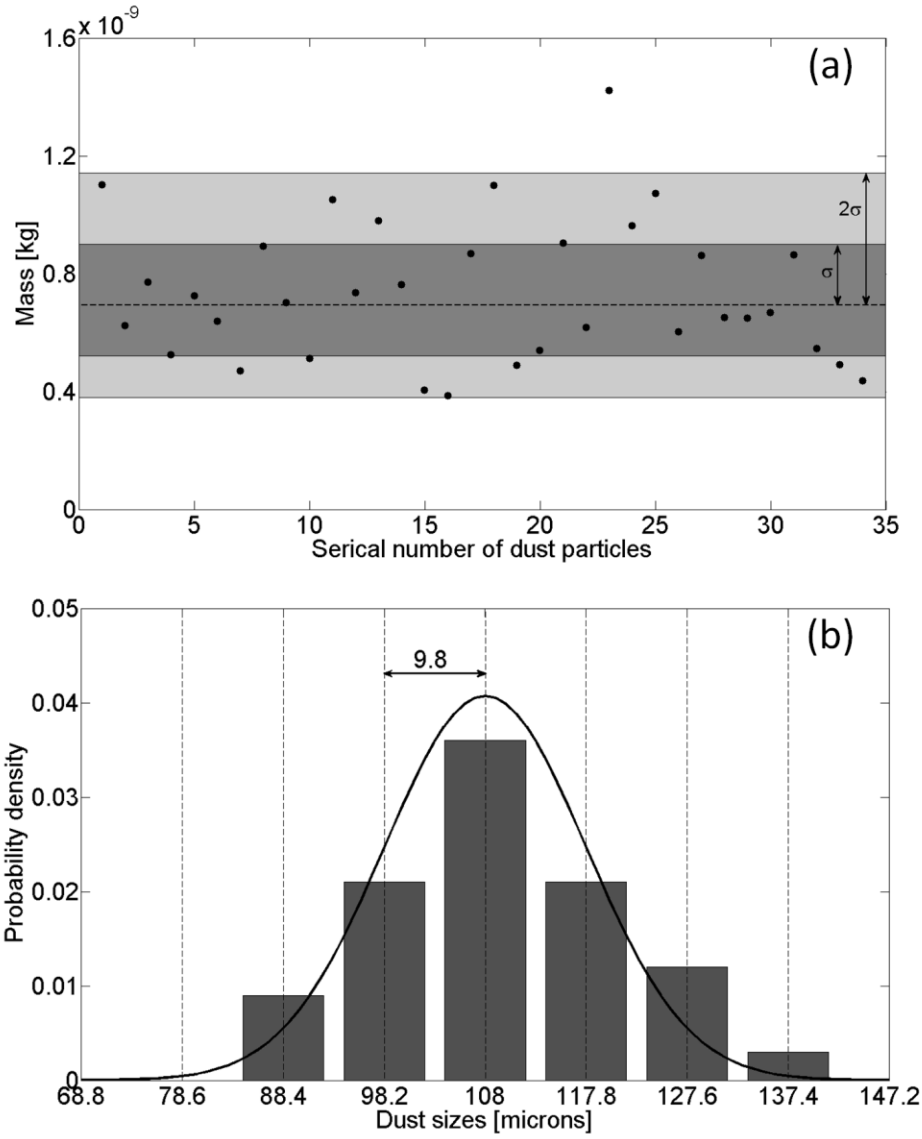

Figure 5.9: (a) The measured mass of the 34 dust particles used in the experiment. The dashed line represents the mass calculated from an average diameter d = 108 μm. The mass range

calculated from σ and 2 σ size ranges are also shown. (b) Measured size distribution of the dust particles from ELDA compared to the size distribution provided by the manufacturer (solid line). The statistical result shows that ELDA instrument determines the mass of individual dust particles with a very high accuracy.

5.6.3 Error Analysis

The size distribution of the dust particles measured by the instrument is very close to the parameters provided by the manufacturer. In this section we evaluate whether this good agreement is serendipitous or if ELDA is capable of measuring mass with high accuracy. First, consider the situation without gravity. For a dust velocity along the *z*-axis v_z, the mass of the dust particle can be estimated from Equation 5.6, which is simplified to

$$m = \frac{QEl}{(v_{y\_ex} - v_{y\_en})v_z}, \tag{5.8}$$

where *l* is the effective length of the electrical field region, which is estimated at 150 mm from the computer model, and is somewhat longer than the physical size of the electrode (100 mm). The velocity change due to electrostatic deflection is:

$$v_{y\_ex} - v_{y\_en} = \frac{y_4 - y_2}{t_4 - t_2} - \frac{y_4' - y_2'}{t_4' - t_2'} = \frac{(y_4 - y_2) - (y_4' - y_2')}{2P/v_z}, \tag{5.9}$$

where *y'* and *t'* refer to measurements by DTS2. Substituting Equation 5.8 into Equation 5.8 and denoting $(y_4 - y_2) - (y_4' - y_2') = Y$, we obtain

$$m = \frac{2QElP}{Yv_z^2}. \tag{5.10}$$

The accuracy of calculating the mass is determined by the accuracy of measuring Q, v_z, and (y_4, y_2, y_4', y_2'). In this laboratory test, the Q and v_z are measured with uncertainties < 3% and < 0.5%, respectively, and thus the uncertainty in the mass calculation depends mostly on the measured positions in the *y*-direction. As shown in Section 5.6.1, the 0.31 ° uncertainty in the angle

measurement of DTS corresponds to an uncertainty *tan* (0.31 °) × *2P* = 0.43 mm in $y_4 - y_2$, thus an uncertainty of $(0.43^2 + 0.43^2)^{1/2} \approx 0.61$ mm in *Y*. On the other hand,

$$Y = \frac{2ElP}{v_z^2}\frac{Q}{m}. \qquad (5.11)$$

For the average $Q/m = 8 \times 10^{-5}$ C/kg, with $v_z \approx 4$ m/s, we get $Y = 6$ mm. An uncertainty of 0.61 mm in *Y* corresponds to a mass range 0.91 - 1.11 *m*, which translates to ± 4.0 μm for the 108 μm mean diameter. This simple analysis suggests that the good agreement in Figure 5.9 is realistic and for the conditions in the experiment the mass is measured accurately. For decreasing *Q/m* or increasing v_z, the deflection *Y* is smaller (Equation 5.11) and the mass *m* becomes more sensitive to uncertainties in *Y*. In the experiment, $Q/m = 2.6 \times 10^{-5}$ C/kg is the lowest charge to mass value with a deflection of approximately *Y* = 2 mm. The corresponding mass range is 0.77 - 1.26 *m*, or ± 9.4 μm in diameter.

5.7 Measureable Region of Parameter Space

The analysis performed in Section 4.3 showed that the uncertainty in the dust trajectory measurement is < 1 ° in angle, 1% in speed, and < 3% in charge for QNR ⩾ 10. The 1 ° uncertainty in angle corresponds to an uncertainty of 2 mm in *Y*. To measure the mass of dust particles within a factor of two, *Y* has to be ≥ 4 mm, and the following equation can be derived:

$$\frac{Q/m}{v_z^2} \geq 3.3 \times 10^{-6}\,\frac{\mathrm{C/kg}}{(\mathrm{m/s})^2}. \qquad (5.12)$$

This relation defines the measurable parameters as shown in Figure 5.10. Part (a) shows the *Q/m* and v_z ranges where the dust particles can be measured within a factor of two when QNR⩾ 10. *Y* < 100 mm is required by the instrument geometry. Part (b) shows the relation between the size of the dust particle and *Q/m* ratio for different surface potentials using the density of lunar regolith particles 3 g/cm^3 (Carrier *et al.*, 1991).

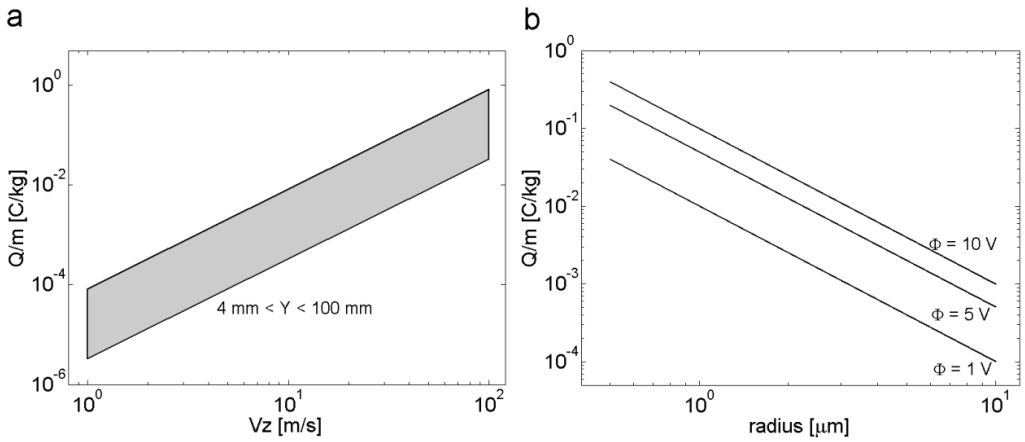

Figure 5.10: (a) The region of parameter space for Q/m and v_z, where the dust mass can be measured with a factor of two when QNR $\geqslant$ 10, according to Equation 5.12. (b) The relationship between the size of the dust particle and the Q/m ratio for surface potentials on the dust of 1, 5, and 10 V on the dust. The density of the particle used is 3 g/cm^3.

Combining the information from part (a) and (b) in Figure 5.10 and supposing the surface potential of the dust particle is 5 V, the measurable region of parameter space for dust size a and passing velocity v_z is shown in Figure 5.11.

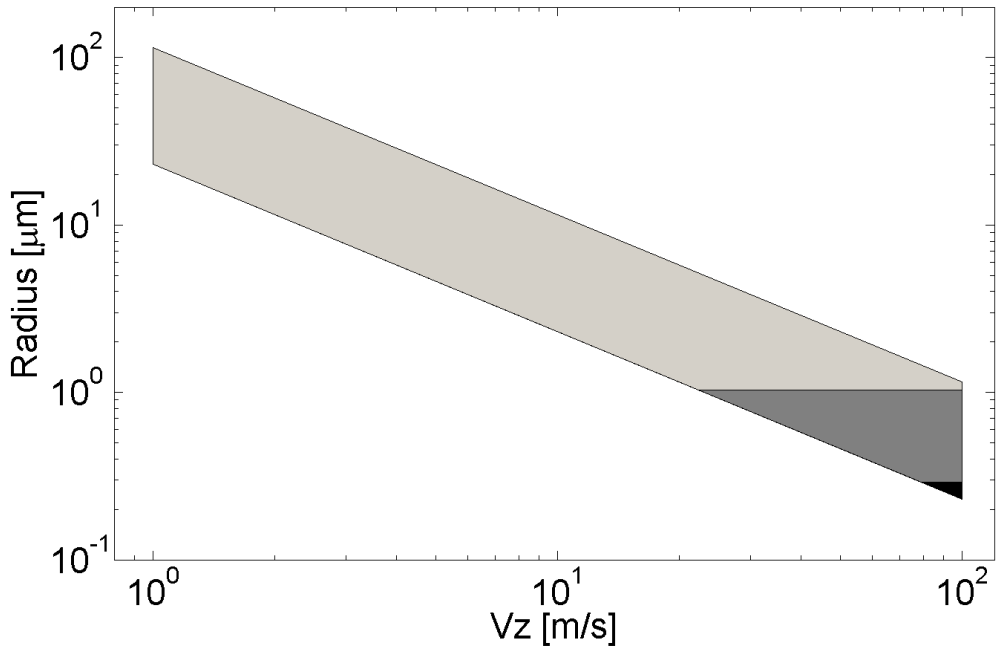

Figure 5.11: The parameter space of dust particle size a and passing velocity v_z, where the dust mass can be measured with a factor of two when QNR $\geqslant$ 10, supposing a surface potential 5 V. The region denoted as light grey is achievable by the prototype ELDA with a noise level 356 e^-. The grey and light grey region is achievable by the theoretical noise level limit of 100 e^-. For the dark region, CSA with noise level lower than 100 e^- is required.

5.8 Other Designs for the Instrument

5.8.1 Reflection versus Deflection

Another design for ELDA was proposed by R. Srama (personal communication). The operating principle is to reflect, instead of deflect, a dust particle in a Refection Field Region (RFR) using a strong electric field. In this section, we show that deflection is a better choice than reflection.

For the reflection version of ELDA, the same DTS is used to measure the velocity and position before and after the particle is reflected. The mass is calculated from Q/m, which is obtained from the change of trajectory. Figure 5.12 shows a schematic of the reflection version

of ELDA. The DTS is exact the same as that in Chapter 2. The RFR region is under the DTS and used to reflect the charged dust particle back into the DTS. The polarity of the voltage in the RFR may be changed over time to detect dust particles of different charge sign.

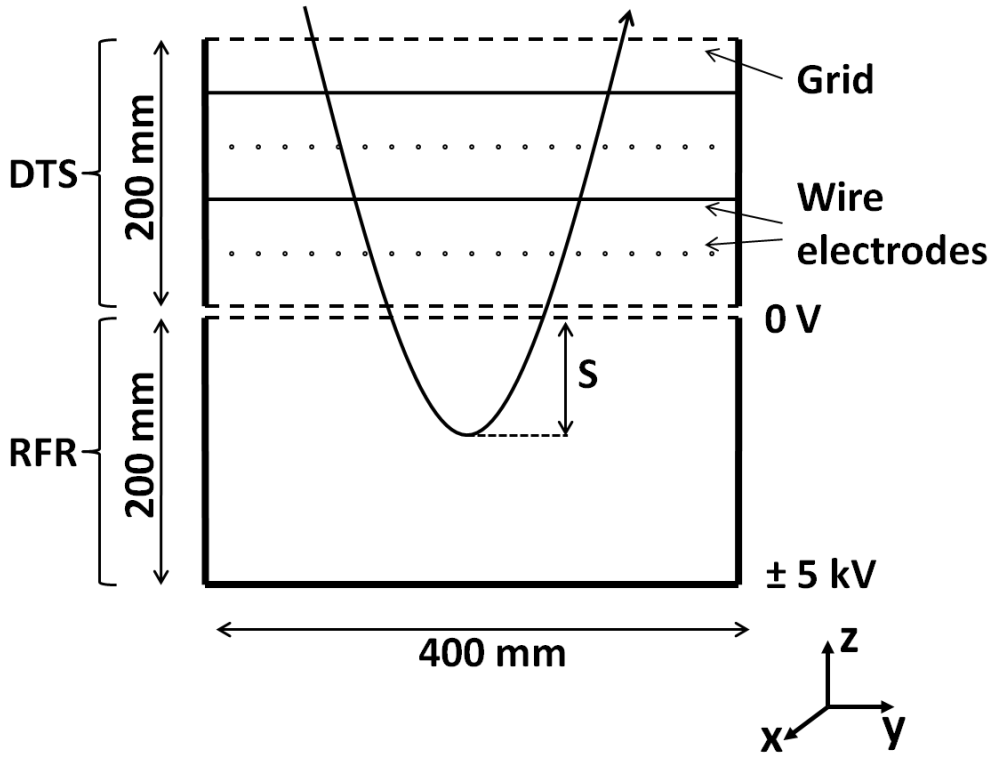

Figure 5.12: The schematics of the reflection version of ELDA. Dust particles passing through DTS are reflected in the Reflection Field Region (RFR). *S* is the depth the particle penetrates into the RFR. The velocity and position of the particle before and after entering the RFR are obtained by a single DTS. The voltage can be changed between +5 kV and -5 kV for detecting positively and negatively charged particles respectively.

The requirements of the reflection version of ELDA are discussed here. In order to avoid hitting the bottom of the device, the charge to mass ratio *Q/m* of the dust particle must satisfy the following equation:

$$QU > \frac{1}{2}mv_z^2 + mgH \,, \tag{5.13}$$

where U = 5 kV is the voltage in the RFR, g = 1.622 m/s^2 (in z-direction) is the gravity on the Moon, and H = 400 mm is the dimension of the instrument along the z-direction. Because the gravitational potential energy is much smaller than the kinetic energy in most cases (v_z = 1-100 m/s), the second term can be ignored and Equation 5.13 becomes

$$\frac{Q}{m} > \frac{v_z^2}{2U}. \tag{5.14}$$

The position change in the y-direction is

$$dy = 4S\frac{v_y}{v_z}. \tag{5.15}$$

From conservation of the total energy, S and v_z can be related as

$$S = \frac{mv_z^2}{4QU}H. \tag{5.16}$$

Combining Equations 5.15 and 5.16, we get

$$dy = \frac{mv_z^2}{QU}H\frac{v_y}{v_z}. \tag{5.17}$$

The change in position in the y-direction should be between 4 and 100 mm in order for the change to be measureable:

$$8\frac{v_z^2}{2U}\frac{v_y}{v_z} < \frac{Q}{m} < 200\ \frac{v_z^2}{2U}\frac{v_y}{v_z}. \tag{5.18}$$

In order to avoid hitting the wall, v_y has to be much smaller than v_z. Suppose v_y / v_z =1/8, then we get:

$$\frac{1}{2}\frac{v_z^2}{U} < \frac{Q}{m} < 12.5\ \frac{v_z^2}{U}. \tag{5.19}$$

From Equation 5.11 and 4 mm < Y< 100 mm, the requirement for the deflection version of ELDA is:

$$\frac{1}{60}\frac{v_z^2}{U} < \frac{Q}{m} < \frac{5}{12}\ \frac{v_z^2}{U}. \tag{5.20}$$

Comparison between the equations above shows that the reflection version of ELDA requires a much higher *Q/m* for the same voltages. To maintain the same measurement capabilities of the reflection version, the voltage in this ELDA has to be increased by a factor of 30, i.e. 150 kV. Such a high voltage is not reasonable for space missions. Therefore, this design for ELDA is not suitable.

5.8.2 Design for Smaller ELDA

The Lunar Dust Environment and Plasma Package (L-DEPP) for the planned Lunar Lander mission by the European Space Agency is intended to investigate the interaction between the lunar surface, dust and local plasma. The ELDA instrument is a good candidate for this goal. However, a reduced ELDA would be needed to satisfy mass, volume, and power limitations.

A reduced performance ELDA has been designed by Gemer, which measures the charge and mass of dust grains, and two components v_y and v_z of the dust particle's velocity (Figure 5.13). All the principles described in the previous section can be applied to this reduced performance ELDA. With accurate mechanical manufacturing, the mass of this instrument can reduced to 4.2 kg.

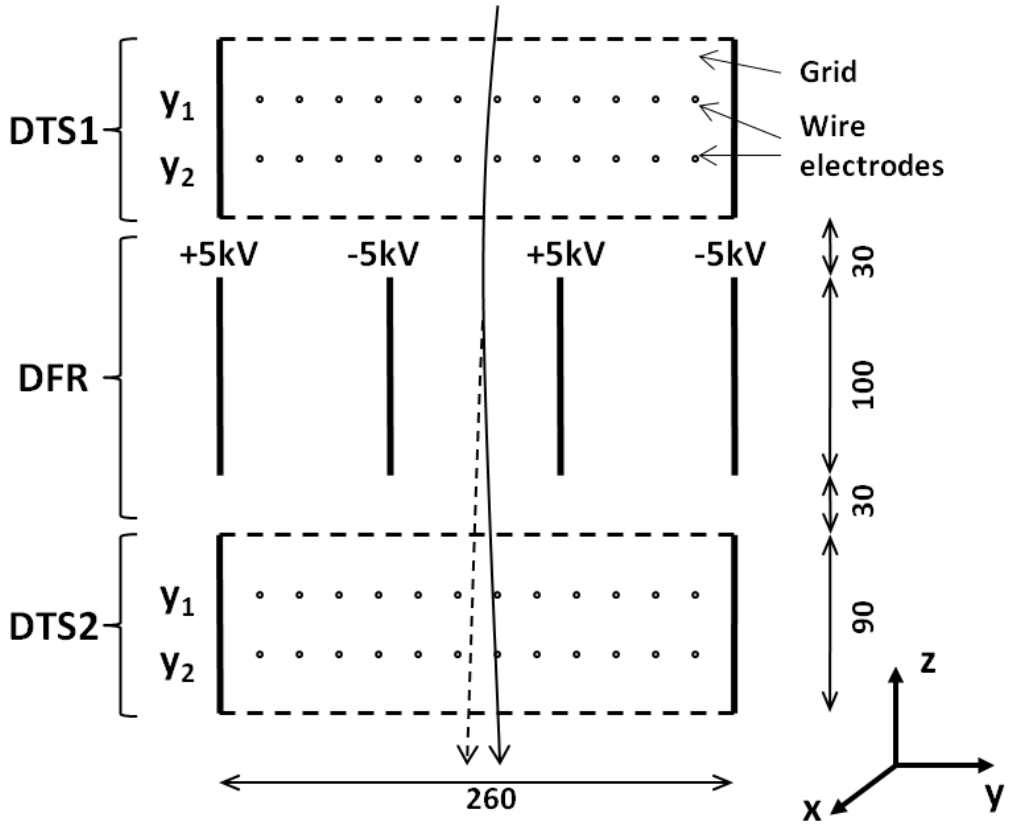

Figure 5.13: The schematics of the reduced performance ELDA, which has been optimized to balance performance and instrument size. The DTS has only two planes of wires, which are arranged in parallel for velocity measurement only in the *y* and *z* directions. There are 12 wires in one plane, and the distance between the two planes is 30 mm. Four plate-electrodes are used in the DFR, which are separated by a distance of 86 mm. The dimensions are given in mm.

6. Summary and Conclusions

The sensitive and accurate measurement of the velocity vector of dust particles has been an outstanding issue of cosmic dust researches. Such measurements can help to identify the source of individual dust particles, and/or determine the history of their interactions with the ambient environment, the interplanetary and planetary magnetic field. Previously, the trajectory information was obtained mostly based on statistical analysis. Trajectory measurement of individual dust grains was started in 1967 by the Cosmic Dust Experiment on Pioneer 8. The instrument obtained the speed and direction information by determining the times and locations of the impacts on two planes of film strips from the same particle. This method has large uncertainties in angle ($\pm 27^\circ$) and speed (10%-15%), and can be only applied to high-speed and relatively large dust particles (> 10 microns).

In interplanetary space, dust particles are charged due to exposure to UV radiation and space plasma, and will acquire approximately +5 V surface potential. The concept of trajectory measurement through the detection of charge on the dust particle was proposed by Auer in 1975. The charge and velocity detector of the Cosmic Dust Analyzer (CDA) on Cassini was the first flight instrument to measure dust velocity through detecting the charge. The velocity is determined by the shape and amplitude of the induced charge signal on two inclined grids, which are connected to each other and to a charge sensitive amplifier (CSA). CDA is sensitive to dust particles with charge > 1 fC (radius a = 1.8 μm for +5V surface potential) and obtains the two dimensional components of the velocity. For this instrument, the accuracy in speed is several percent while the accuracy in angle is several degrees.

This work presented the design and characterization of the Dust Trajectory Sensor (DTS) instrument. For higher sensitivity, DTS employs an array of wire electrodes, with each electrode

connected to a charge sensitive amplifier (CSA). Wire electrodes have a small capacitance and allow operation with lower noise, extending the detectable range toward smaller dust particles. In theory, DTS could detect dust charges ≥ 0.1 fC (0.18 micron radius), which corresponds to the noise limits of modern CSA electronics. The DTS measurements also provide the full three-dimensional information of the particle's velocity and trajectory.

The data analysis method for DTS signals is based on fitting the experimental data with simulated signals. The best fit then provides the particle's characteristics: the charge, the velocity, and the incidence angle relative to the instrument. The attainable accuracy of the DTS instrument is limited by (a) the accuracy of the computer simulation results, (b) the precision of the mechanical geometry of the instrument, (c) the charge-to-noise ratio (QNR) of the measurement, and (d) sample rate. The uncertainties from part (a) were analyzed, and found negligible in comparison. A numerical study was performed to evaluate the effects of part (c) and (d). A laboratory version of the DTS instrument has been tested with particles in the velocity range of 2–5 km/s using the dust accelerator facility in Heidelberg, Germany. Both the numerical study and the experimental data show that the accuracy of the instrument is better than 1% in velocity and 1 ° in direction even for noisy data (QNR = 10). For a subset of data, however, the uncertainty of the incidence angle can increase up to a few degrees. This occurs when the dust particle happens to pass very close to one of the wire electrodes, resulting in weak signals on the other two closest wires and making it difficult to determine which side the particle passed the wire on.

The Electrostatic Lunar Dust Analyzer (ELDA) instrument is a specific application of the DTS concept and is designed for the measurement of slow-moving (1–100 m/s) charged dust particles mobilized near the lunar surface. The ELDA instrument is capable of measuring the

charge, velocity, and mass of individual dust particles simultaneously. ELDA consists of two DTS units with a deflection-field region (DFR) in between. The DFR uses a strong electrostatic field (around 1×10^4 V/m) to bend the electrically charged grain's natural trajectory. The two DTS units measure the charge and velocity vector of an individual dust particle before and after its trajectory is modified by the DFR. This arrangement allows for a precise measurement of the deflection of the particle's trajectory, which is used to determine its mass. In this thesis we present the mass derivation algorithm and computer modeling of the DFR. A full laboratory prototype version of the ELDA instrument has been built and tested in vacuum. The statistical analysis of the results for $E = 0$ in the DFR can be used to assess the accuracy of the instrument geometry (displacements and tilts) and provide the orientation of the gravity vector with respect to the instrument. The analyses from this work show that the dust mass can be measured within a factor of two for conditions that satisfy Q/m [C/kg] $\geq 3.3 \times 10^{-6}\, v_z^2$[m/s] and QNR ≥ 10.

The constructed laboratory prototypes proved the concepts of DTS and ELDA measurements. The shielding of the DTS is adequate, and applying the proper grounding scheme, it is possible to achieve the theoretical minimum noise level of the CSA electronics. The CSA electronics integrated into the instrument are critical for the performance of both DTS and ELDA. The noise levels determine the sensitivity, i.e. the smallest detectable dust size. In order to extend the detectable size range to smaller dust particles, better electronics need to be developed and integrated into the DTS. We also find that low-frequency noise can introduce larger errors in both direction and mass measurements. The findings in this thesis allow defining the requirements for a potential flight version of the ELDA instrument to be deployed on the lunar surface.

Bibliography

Allison, R. J., McDonnell, J. A. M., 1981. Secondary cratering-effects on lunar micro-terrain: implications for the micrometeoroid flux. Proc. Lunar Planet. Sci. Conf 12B, 1703–1716.

Altobelli, N., Kempf, S., Landgraf, M., Srama, R., Dikarev, V., Krüger, H., Moragas-Klostermeyer, G., Grün, E., 2003. Cassini between Venus and Earth: Detection of interstellar dust. J. Geophys. Res. 108 (A10), 8032.

Altobelli, N., Kempf, S., Krüger, H., Landgraf, M., Roy, M., Grün, E., 2005. Interstellar dust flux measurements by the Galileo dust instrument between the orbits of Venus and Mars. J. Geophys. Res. 110, A07102.

Auer, S., Sitte, K., 1968. Detection technique for micrometeoroids using impact ionization. Earth Planet. Sci. Lett. 4, 178-183.

Auer, S., 1975. Two high resolution velocity vector analyzers for cosmic dust particles. Rev. Sci. Instrum. 46, 127–135.

Auer, S., 1982. Imaging by dust rays: a dust ray camera. Opt. Acta 29, 1421–1426.

Auer, S., von Bun, F.O., 1994. Highly transparent and rugged sensor for velocity determinations of cosmic dust particles. LPI Tech. Rep. 94-05, 25–29.

Auer, S., 2001. In: Interplanetary Dust, edited by E. Grün, B. Gustafson, S. F. Dermott, and H. Fechtig, Springer, Heidelberg, 385–444.

Auer, S., Grün, E., Srama, R., Kempf, S., Auer, R., 2002. The charge and velocity detector of the cosmic dust analyzer on Cassini. Planet. Space Sci. 50, 773.

Auer, S., 2007. Low-noise amplifier for measuring dust charges in the presence of plasma and UV radiation. ESA SP-643, 231–233.

Auer, S., Grün, E., Kempf, S., Srama, R., Srowig, A., Sternovsky, Z., Tschernjawski, V., 2008 Characteristics of a dust trajectory sensor. Rev. Sci. Instrum. 79, 084501.

Auer, S., Lawrence, G., Grün, E., Henkel, H., Kempf, S., Srama, R., Sternovsky, Z., 2010. A self-triggered dust trajectory sensor. Nucl. Instrum. Methods A 622, 74-82.

Baguhl, M., Grün, E., Hamilton, D. P., Linkert, G., Riemann, R., Staubach, P., Zook, H. A., 1995. The flux of interstellar dust observed by Ulysses and Galileo. Space Sci. Rev. 72, 471.

Berg, O. E., Richardson, F. F., 1969. The Pioneer 8 Cosmic Dust Experiment. Rev. Sci. Instrum. 40, 1333–1337.

Berg, O. E., Grün, E., 1973. Evidence of hyperbolic cosmic dust particles. Space Res. 13, 1046.

Berg, O. E., Richardson, F. F., Burton, H., 1973. APOLLO 17 Preliminary Science Report. NASA SP-330, 16.

Berg, O. E., Richardson, F. F., Rhee, J. W., Auer, S., 1974. Preliminary results of a cosmic dust experiment on the Moon. Geophys. Res. Lett. 1, 289–290.

Bernhard, P., Birger, S., 2001. Accretion of extraterrestrial matter throughout earth's history. Springer. 66–67.

Brownlee, D. E., Tsou, P., Anderson, J. D., Hanner, M. S., Newburn, R. L., Sekanina, Z., Clark, B. C., Hörz, F., Zolensky, M. E., Kissel, J., JMcDonnell, J. A. M., Sandford, S. A., Tuzzolino, A. J., 2003. Stardust: Comet and interstellar dust sample return mission. J. Geophys. Res. 108 (E10), 8111.

Burns, J. A., Lamy, P. L., Soter, S., 1979. Radiation Forces on Small Particles in the Solar System. Icarus 40, 1–48.

Carrier III, W. D., Olhoeft, G. R., Mendell, W., 1991. Physical properties of the lunar surface. In: Heiken, G. H., Vaniman, D. T., French, B. M. (Eds.), Lunar Sourcebook: A User's Guide to the Moon. Cambridge Univ. Press.

Ciolek, G. E., 1995. ASP Conf. Ser. 80, The Physics of the Interstellar Medium and Intergalactic Medium, edited by A. Ferrara, C. F., McKee, C., Heiles, P. R., Shapiro (San Francisco: ASP), 174.

Colangeli, L., Lopez-Moreno, J. J., Palumbo, P., Rodriguez, J., Cosi, M., Corte, V. D., Esposito, F., Fulle, M., Herranz, M., Jeronimo, J. M., Lopez-Jimenez, A., Epifani, E. M., Morales, R., Moreno, F., Palomba, E., Rotundi, A., 2007. The Grain Impact Analyser and Dust Accumulator (GIADA) Experiment for the Rosetta Mission: Design, Performances and First Results. Space Sci. Rev. 128, 803–821.

Colwell, J. E., Batiste, S., Horányi, M., Robertson, S., Sture, S., 2007. Lunar surface: dust dynamics and regolith mechanics. Rev. Geophys. 45, RG2006.

Colwell, J. E., Robertson, S., Horányi, M., Wang, X., Poppe, A., Wheeler, P., 2009. Lunar Dust Levitation. J. Aerospace Eng. 22, 2-9.

Czechowski, A., Mann, I., 2003. Penetration of interstellar dust grains into the heliosphere. J. Geophys. Res. 108 (A10), 8038.

Delsemme, A. H., 1973. GAS AND DUST IN COMETS. Space Sci. Rev. 15, 89.

Dietzel, H., Neukum, G., Rauser, P., 1972. Micrometeoroid simulation studies on metal targets. J. Geophys. Res. 77, 1375–1395.

Dietzel, H., Eichhorn, G., Fechtig, H., Grün, E., Hoffmann, H. -J., Kissel, J., 1973. The HEOS 2 and Helios micrometeoroid experiments. J. Phys. (E) Scientific Instrum. 6, 209–217.

Duncan, N., Sternovsky, Z., Grün, E., Auer, S., Horányi, M., Drake, K., Xie, J., Lawrence, G., Hansen, D., Le, H., 2011. The Electrostatic Lunar Dust Analyzer (ELDA) for the detection and trajectory measurement of slow-moving dust particles from the lunar surface. Planet. Space Sci. 59, 1446–1454.

Flanagan, T. M., Goree, J., 2006. Dust release from surfaces exposed to plasma. Phys. Plasmas 13, 123504.

Frisch, P. C., Dorschner, J. M., Geiss, J., Mayo Greenberg, J., Grün, E., Landgraf, M., Hoppe, P., Jones, A. P., Krätschmer, W., Linde, T. J., Morfill, G. E., Reach, W., Slavin, J. D., Svestka, J., Witt, A. N., Zank, G. P., 1999. Astrophys. J. 525, 492.

Graps, A. L., Grün, E., Svedhem, H., Krüger, H., Horányi, M., Heck, A., Lammers, S., 2000. Io as a source of the jovian dust streams. Nature 405, 48.

Grogan, K., Dermott, S. F., Gustafson, B. Å. S., 1996. An estimation of the interstellar contribution to the zodiacal thermal emission. Astrophys. J. 472, 812.

Grün, E., Zook, H. A., 1980. Dynamics of micrometeoroids. In: Halliday I., McIntosh B.A. (eds.) Solid Particles in the Solar System. Proc. IAU Symp. 90, Reidel, Dordrecht, 293.

Grün, E., Fechtig, H., Hanner, M. S., Kissel, J., Lindblad, B.-A., Linkert, D., Maas, D., Morfill, G. E., Zook, H. A., 1992a. The Galileo dust detector. Space Sci. Rev. 60, 317–340.

Grün, E., Fechtig, H., Giese, R. H., Kissel, J., Linkert, D., Maas, D., McDonnell, J. A. M., Morfill, G. E., Schwehm, G., Zook, H. A., 1992b. The Ulysses dust experiment. Astron. Astrophys. Suppl. Ser. 92, 411–423.

Grün, E., Zook, H. A., Baguhl, M., Balogh, A., Bame, S. J., Fechtig, H., Forsyth, R., Hanner, M. S., Horányi, M., Kissel, J., Lindblad, B. A., Linkert, D., Linkert, G., Mann, I., Mcdonnel, J., Morfill, G., Phillips, J., Polanskey, C., Schwehm, G., Siddique, N., Staubach, P., Svestka, J., Taylor, A., 1993. Discovery of Jovian dust streams and interstellar grains by the Ulysses spacecraft. Nature 362, 428–430.

Grün, E., Gustafson, B., Mann, I., Baguhl, M., Morfill, G. E., Staubach, P., Taylor, A., Zook, H. A., 1994. Interstellar dust in the helioshere. Astron. Astrophys. 286, 915.

Grün, E., Kempf, S., Krüger, H., LandgraF, M., Srama, R., 2001. Dust astronomy: a new approach to the study of interstellar dust. In B. Warmbein, ed., Proceedings of the Meteoroids 2001 Conference, 6 - 10 August 2001, Kiruna, Sweden, ESA SP-495, 651–662, ESA Publications Division, Noordwijk.

Grün, E., Horányi, M., Sternovsky, Z., 2011. The Lunar dust environment. Planet. Space Sci. 59, 1672–1680.

Grün, E., Sternovsky, Z., Horanyi, M., Hoxie, V., Robertson, S., Xie, J., Auer, S., Landgraf, M., Postberg, F., Price, M.C., Srama, R., Starkey, N. A., Hillier, J.A., Franchi, I. A., Tsou, P., Westphal, A., Gainsforth, Z., 2012. Active Cosmic Dust Collector. Plan. Space Sci. 60, 261–273.

Gurnett, D. A., Ansher, J. A., Kurth, W. S., Granroth, L. J., 1997. Micron-sized dust particles detected in the outer solar system by the Voyager 1 and 2 plasma wave instruments. Geophys. Res. Lett. 24, 3125.

Hamilton, D., Burns, J., 1993. Ejection of dust from Jupiter's gossamer ring. Nature 364, 695.

Hamilton, D. P., Grün, E., Baguhl, M., 1996. In: Physics, Chemistry, and Dynamics of Interplanetary Dust (ASP Conf. Series, vol. 104), ed. B. A. A. S. Gustafson, M. S. Hanner (ASP, San Francisco), 31–34, proc. IAU Coll. No. 150.

Hartzell, C. M., Scheeres, C. J., 2011. The role of cohesive forces in particle launching on the Moon and asteroids. Planet. Space Sci., 59, 1758.

Hastings, E. C., 1964. The Explorer XVI micrometeoroid satellite. Supplement III, preliminary results for period May 27, 1963 through July 22, 1963. NASA TM X-949.

Hillier, J. K., Green, S. F., Mcbride, N., Schwanethal, J. P., Postberg, F., Srama, R., Kempf, S., Moragas-Klostermeyer, G., Mcdonnell, J. A. M., Grün, E., 2007. The composition of Saturn's E ring. Mon. Not. Roy. Astron. Soc. 377, 1588–1596.

Hoffmann, F. -J., Fechtig, H., Grün, E., Kissel, J., 1975. Temporal fluctuations and anisotropy of the micrometeoroid flux in the Earth-Moon system. Planet. Space Sci. 23, 985–991.

Holzer, T. E., 1989. Interaction between the solar-wind and the interstellar-medium. Annu. Rev. Astron. Astr. 27, 199.

Horányi, M., Burns, J., Hamilton, D., 1992. The dynamics of Saturn's E ring particles. Icarus 97, 248.

Horányi, M., 1996. Charged dust dynamics in the solar system. Ann. Rev. Astron. Astrophys. 34, 383–418.

Horányi, M., 2000. Dust streams from Jupiter and Saturn. Phys. of Plasmas 7, 3847–3850.

Horányi, M., Hoxie, V., James, D., Poppe A., Bryant, C., Grogan, B., Lamprecht, B., Mack, J., Bagenal, F., Batiste, S., Bunch, N., Chanthawanich, T., Christensen, F., Colgan, M., Dunn, T., Drake, G., Fernandez, A., Finley, T., Holland, G., Jenkins, A., Krauss, C., Krauss, E., Krauss, O., Lankton, M., Mitchell, C., Neeland, M., Reese, T., Rash, K., Tate, G., Vaudrin, C., Westfall, J., 2007. The Student Dust Counter on the New Horizons Mission. Space Sci. Rev. 140, 387–402.

Horányi, M., Sternovsky, Z., Grün, E., Srama, R., Lankton, M., Gathright, D., 2009. The Lunar Dust EXperiment (LDEX) on the Lunar Atmosphere and Dust Environment Explorer (LADEE) Mission. Lunar and Planetary Institute Science Conference Abstracts 40, 1741.

Humes, D. H., 1980. Results of Pioneer 10 and 11 Meteoroid Experiments: Interplanetary and near-Saturn. J. Geophys. Res. 85, 5841.

Humes, D. H., O'neal, R. L., KinardI, W. H., Alvarez, J. M., 1980. Impact of Saturn ring particles on Pioneer 11. Science 207, 443.

Igenbergs, E., Hüdepohl, A., Uesugi, K., Hayashi, T., Svedhem, H., Iglseder, H., Koller, G., Glasmachers, A., Grün, E., Schwehm, G., Mizutani, H., Yamamoto, T., Fujimura, A., Ishii, N., Araki, H., Yamakoshi, K., Nogami, K., 1991. The Munich dust counter—A cosmic dust experiment on board of the MUSES—A mission of Japan. In Origin and evolution of interplanetary dust, eds. A. C. Levasseur-Regourd *et al.*, (Kluwer Academic Publishers) 45–48.

Jackson, A. A., Zook, H. A., 1989. A Solar System dust ring with the Earth as its shepherd. Nature 337, 629.

Jones, G. H., Roussos, E., Krupp, N., Beckmann, U., Coates, A. J., Crary, F., Dandouras, I., Dikarev, V., Dougherty, M. K., Garnier, P., Hansen, C. J., Hendrix, A. R., Hospodarsky, G. B., Johnson, R. E., Kempf, S., Khurana, K. K., Krimigis, S. M., Krüger, H., Kurth, W. S., Lagg, A., McAndrews, H. J., Mitchell, D. G., Paranicas, C., Postberg, F., Russell, C. T., Saur, J., Seiß, M., Spahn, F., Srama, R., Strobel, D. F., Tokar, R., Wahlund, J.-E., Wilson, R. J., Woch, J., Young, D., 2008. The Dust Halo of Saturn's Largest Icy Moon, Rhea. Science 319, 1380.

Kassel, P. C., Jr. 1973. Characteristics of capacitor-type micrometeoroid flux detectors when impacted with simulated micrometeoroids. Technical Note D-7359, NASA, Washington.

Kempf, S., Srama, R., Altobelli, N., Auer, S., Tschernjawski, V., Bradley, J., Burton, M. E., Helfert, S., Johnson, T. V., Krüger, H., Moragas-Klostermeyer, G., Grün, E., 2004. Cassini between Earth and asteroid belt: first in-situ charge measurements of interplanetary grains. Icarus 171, 317.

Kempf, S., Srama, R., Horányi, M., Burton, M., Helfert, S., Moragasklostermeyer, G., Roy, M., Grün, E., 2005. High-velocity streams of dust originating from Saturn. Nature 433, 289–291.

Kissel, J., 1986. The Giotto particulate impact analyser. ESA-SP 1077, 67–83.

Krivov, A. V., Kimura, H., Mann, I., 1998. Dynamics of Dust near the Sun. Icarus 134, 311.

Krüger, H., Krivov, A. V., Hamilton, D. P., Grün, E., 1999. Detection of an impact-generated dust cloud around Ganymede. Nature 399, 558–560.

Krüger, H., Krivov, A. V., Grün, E., 2000. A dust cloud of Ganymede maintained by hypervelocity impacts of interplanetary micrometeoroids. Planet. Space Sci. 48, 1471–1475.

Krüger, H., Krivov, A. V., Sremcevic, M., Grün, E., 2003. Impact-generated dust clouds surrounding the Galilean moons. Icarus 164, 170–187.

Krüger, H., Landgraf, M., Altobelli, N., Grün, E., 2007. Interstellar Dust in the Solar System. Space Sci. Rev. 130, 401–408.

Kurat, G., Koeberl, C., Presper, T., Brandstatter, F., Maurette, M., 1994. Petrology and Geochemistry of Antarctic Micrometeorites. Geochim. and Cosmochimica Acta 58, 3879.

Landgraf, M., Augustsson, K., Grün, E., Gustafson, B. Å. S., 1999. Deflection of the Local Interstellar Dust Flow by Solar Radiation Pressure. Science 286, 2, 319.

Landgraf, M., 2000. Modeling the motion and distribution of interstellar dust inside the heliosphere. J. Geophys. Res. 105(A5), 10, 303.

Landgraf, M., Krüger, H., Altobelli, N., Grün, E., 2003. Penetration of the heliosphere by the interstellar dust stream during solar maximum. J. Geophys. Res. 108, 5.

Leinert, C., Grün, E., 1990. Interplanetary Dust. Physics and Chemistry in Space (R. Schwenn and E. Marsch eds.). Springer-Verlag. 204–275.

Leinert, C., Bowyer, S., Haikala, L. K., Hanner, M. S., Hauser, M. G., Levasseur-Regourd, A. -Ch., Mann, I., Mattila, K., Reach, W. T., Schlosser, W., Staude, H. J., Toller, G. N., Weiland, J. L., Weinberg, J. L., A.N. Witt, A. N., 1998.The 1997 reference of diffuse night sky brightness. Astron. Astrophys. Suppl. Ser. 127, 1-99.

Levasseur-Regourd, A. C., 1996. Optical and Thermal Properties of Zodiacal Dust. Physics, Chemistry and Dynamics of Interplanetary Dust, ASP Conference series 104, 301.

Love, S. G., Joswiak, D., Brownlee, D. E., 1994. Densities of Stratospheric Micrometeorites. Icarus 111, 227.

Mann, I., Kimura, H., 2000. Interstellar dust properties derived from mass density, mass distribution, and flux rates in the heliosphere. J. Geophys. Res. 105 (A5), 10, 317.

Mann, I., Czechowski, A., Grzedzielski, S., 2004. Dust measurements at the edge of the solar system. Adv. Space Res. 34, 179.

Mann, I., Köhler, M., Kimur, H., Czechowski, A., Minato, T., 2006. Dust in the solar system and in extra-solar planetary systems. Astron. Astrophys. Rev. 13(3), 159.

Mann, I., Czechowski, A., Meyer-Vernet, N., Zaslavsky, A., Lamy, H., 2010. Dust in the interplanetary medium. Plasma Phys. Control. Fusion 52, 124012.

Maurette, M., Olinger, C., Michel-Levy, M. C., Kurat, G., Pourchet, M., Brandstätter, F., Bourot-Denise, M., 1991. A collection of diverse micrometeorites recovered from 100 tonnes of Antarctic blue ice. Nature 351, 44.

McCoy, J. E., Criswell, D. R., 1974. Evidence for a high latitude distribution of lunar dust. In: Proceedings of the Fifth Lunar Science Conference, 2991.

McCoy, J. E., 1976. Photometric studies of light scattering above the lunar terminator from Apollo solar corona photography. In: Proceedings of the Seventh Lunar Science Conference, 1087–1112.

Morabito, L. A., Synnott, S. P., Kupferman, P. N., Collins, S. A., 1979. Discovery of currently active extraterrestrial volcanism. Science 204, 972.

Morfill, G. E., Grün, E., 1979. The motion of charged dust particles in interplanetary space —1. The zodiacal dust cloud. Planet. Space Sci. 27, 1269–1282.

Mukai T., 1985. On the Solar dust ring(s). In: Giese R.H., Lamy P., (eds.) Properties and Interactions of Interplanetary Dust. D. Reidel Publishing Company, 59.

Mukai T., 1996. Sublimation of Interplanetary Dust. In: Gustafson B. Å. S., Hanner M.S., (eds.) Physics, Chemistry, and Dynamics of Interplanetary Dust. ASP Conf. Series vol. 104, Kluwer, Dordrecht, 453.

Naumann, R. J., Jex, D. W., Johnson, C. L., 1969. Calibration of Pegasus and Explorer XXIII detector panels. NASA Technical Report R-321.

Nitter, T., Havnes, O., 1992. Dynamics of dust in a plasma sheath and injection of dust into the plasma sheath above moon and asteroidal surfaces. Earth, Moon, and Planets 56, 7–34.

Nitter, T., Havnes, O., Melandsø, F., 1998. Levitation and dynamics of charged dust in the photoelectron sheath above surfaces in space. J. Geophys. Res. 103, 6605–6620.

Poppe, A., Horányi, M., 2010. Simulations of the photoelectron sheath and dust levitation on the lunar surface. J. Geophys. Res. 115, A08106.

Poppe, A., Halekas, J. S., Horányi, M., 2011. Negative potentials above the dayside lunar surface in the terrestrial plasma sheet: evidence of non-monotonic potentials. Geophys. Res. Lett. 38, L02103.

Salpeter, E. E., 1974. Dying stars and reborn dust. Rev. Mod. Phys. 46, 433.

Schwehm, G., Rohde, M., 1977. Dynamical effects on circumsolar dust grains. J. Geophys. 42, 727–735.

Sheridan, T. E., Goree, J., Chiu, Y. T., Rairden, R. L., Kiessling, J. A., 1992. Observation of dust shedding from material bodies in a plasma. J. Geophys. Res. 97, 2935.

Sickafoose, A. A., Colwell, J. E., Horányi, M., Robertson, S., 2002. Experimental levitation of dust grains in a plasma sheath. J. Geophys. Res. 107, 1408.

Simpson, J. A., Tuzzolino, A. J., 1985. Polarized polymer films as electronic pulse detectors of cosmic dust particles. Nucl. Instr. and Meth. A236, 187–202.

Simpson, J. A., Tuzzolino, A. J., 1989. Cosmic dust investigations II. Instruments for measurement of particle trajectory, velocity and mass. Nucl. Instr. and Meth. A279, 625–639.

Singer, S. F., Stanley, J. E., Kassel, P. C., 1985. The LDEF interplanetary dust experiment. In Properties and Interactions of Interplanetary Dust, eds. R. H. Giese and P. Lamy (Dordrecht: Reidel), 117–120.

Spahn, F., Schmidt, J., Albers, N., Hörning, M., Makuch, M., Seiβ, M., Kempf, S., Srama, R., Dikarev, V., Helfert, S., Moragas-Klostermeyer, G., Krivov, A., Sremčević, M., Tuzzolino, A. J., Economou, T., Grün, E., 2006. Cassini Dust Measurements at Enceladus and Implications for the Origin of the E Ring. Science 311, 1416.

Srama, R., Srowig, A., Rachev, M., Grün, E., Kempf, S., Moragas-Klostermeyer, G., Srowig, A., Conlon, T., Harris D., Auer, S., Glasmachers, A., Helfert, S., Linnemann, H., Tschernjawski, V., 2004. DEVELOPMENT OF AN ADVANCED DUST TELESCOPE. Earth, Moon, and Planets 95, 211–220.

Srama, R., Woiwode, W., Postberg, F., Armes, S. P., Fujii, S., Dupin, D., Ormond-Prout, J., Sternovsky, Z., Kempf, S., Moragas-Klostermeyer, G., Mocker, A., Grün, E., 2009. Mass spectrometry of hyper-velocity impacts of organic micrograins. Rapid Commun. Mass Spectrom 23, 3895–3906.

Srowig, A., 2004. Ph.D. dissertation (Heidelberg, Germany).

Sternovsky, Z., Horányi, M., Robertson, S., 2001. Charging of dust particles on surfaces. J. Vac. Sci. Technol. 19 (5), 2533.

Sternovsky, Z., Robertson, S., Sickafoose, A., Colwell, J., Horányi, M., 2002. Contact charging of lunar and Martian dust simulants. J. Geophys. Res. 107, 5105.

Sternovsky, Z., Amyx, K., Bano, G., Landgraf. M., Horanyi, M., Knappmiller. S., Robertson. S., Grün, E., Srama, R., Auer, S., 2007. Large area mass analyzer instrument for the chemical analysis of interstellar dust particles. Rev. Sci. Instrum. 78, 01450.

Sternovsky, Z., Grün, E., Drake, K., Xie, J., Horanyi, M., Srama, R., Kempf, S., Postberg, F., Mocker, A., Auer, S., Krüger, H., 2011. Novel instrument for Dust Astronomy: Dust Telescope. Aerospace Conference, 2011 IEEE, 1–8.

Takechi, S., Nogami, K., Miyachi, T., Fujii, M., Hasebe, N., Iwai, T., Sasaki, S., Ohashi, H., Shibata, H., Grün, E., Srama, R., Okada, N., 2009. Laboratory calibration measurements of a piezoelectric lead zirconate titanate cosmic dust detector at low velocities. Adv. Space Res. 43, 905–909.

Timmermann, R., Grün, E., 1991. Plasma emission from high velocity impacts of microparticles onto water ice. In: Origin and Evolution of Interplanetary Dust, eds. A. C. Levasseur-Regourd *et al*., (Kluwer), 375–378.

Walch, B., Horányi, M., Robertson, S., 1994. Measurement of the charging of individual dust grains in a plasma. IEEE Trans. Plasma Sci. 22, 97–102.

Wallis, M. K., Hassan, M. A. H., 1985. Heating and frictional drag on the heliospheric gas by the solar-wind. A&A 151, 435.

Wang, BQ., 1991. Time evolution of interstellar dust and far-infrared luminosity of disk galaxies, Astrophys. J. 374, 456.

Wang, X., Colwell, J., Horányi, M., Robertson, S., 2007. Charge of dust on surfaces in plasma. IEEE Trans. Plasma Sci. 35 (2), 271–279.

Wang, X., Horányi, M., Robertson, S., 2009. Experiments on dust transport in plasma to investigate the origin of the lunar horizon glow. J. Geophys. Res. 114, A05103.

Wang, X., Horányi, M., Robertson, S., 2010. Investigation of dust transport on the lunar surface in a laboratory plasma with an electron beam. J. Geophys. Res. 115, A11102.

Wang, X., Horányi, M., Robertson, S., 2011a. Dust transport on a surface in plasma. IEEE Trans. Plasma Sci. 39, 2730-2731.

Wang, X., Horányi, M., Robertson, S., 2011b. Dust transport near electron beam impact and shadow boundaries. Planet. Space Sci. 59, 1791.

Weaver, H. A., Gibson, W. C., Tapley, M. B., Young, L. A., Stern, S. A., 2008. Overview of the New Horizons Science Payload. Space Sci. Rev. 140, 75–91.

Witte, M., Banaszkiewicz, H., Rosenbauer, H., 1996. Recent results on the parameters of the interstellar helium from the ULYSSES/GAS experiment. Space Sci. Rev. 78, 289–296.

Zolensky, M. E., Barrett, R. A., Hörz, F., 1994. The use of silica aerogel to collect interplanetary dust in space. LPI Tech. Rpt. 94-05, 94–98.

Zook, H. A., Berg, O. E., 1975. A SOURCE FOR HYPERBOLIC COSMIC DUST PARTICLES. Planet. Space Sci. 23, 183–203.

Zook, H. A., Lange, G., Grün, E., Fechtig, H., 1984. Lunar primary and secondary microcraters and the micrometeoroid flux. Lunar Planet. Sci. XV, 965–966.

Zook, H. A., McCoy, E., 1991. Large scale lunar horizon glow and a high altitude lunar dust exosphere. Geophys. Res. Lett. 18, 2117.

Zook, H., Grün, E., Baguhl, M., Hamilton, D., Linkert, G., Liou, J. C., Forsyth, R., Phillips, J., 1996. Solar wind magnetic field bending of Jovian dust trajectories. Science 274, 1501–1503.

Appendix A

Publications

A.1 Published Papers:

- **J. Xie**, Z. Sternovsky, E. Grün, S. Auer, N. Duncan, K. Drake, H. Le, M. Horanyi, and R. Srama. Dust trajectory sensor: Accuracy and data analysis. Rev. Sci. Instrum. 82, 105104 (2011).
- P. Northway, S. Auer, K. Drake, M. Horanyi, A. Mocker, T. Munsat, A. Shu, Z. Sternovsky, E. Thomas and **J. Xie**. Characteristics of a new dust coordinate sensor. Meas. Sci. Technol. 23, 105902 (2012).
- E. Grün, Z. Sternovsky, M. Horanyi, V. Hoxie, S. Robertson, **J. Xie**, S. Auer, M. Landgraf, F. Postberg, M. C. Price, R. Srama, N. A. Starkey, J. A. Hillier, I. A. Franchi, P. Tsou, A. Westphal, and Z. Gainsforth. Active Cosmic Dust Collector. Plan. Space Sci. 60, 261 (2012).
- N. Duncan, Z. Sternovsky, E. Grün, S. Auer, M. Horanyi, K. Drake, **J. Xie**, G. Lawrence, D. Hansen, and H. Le. The Electrostatic Lunar Dust Analyzer (ELDA) for the detection and trajectory measurement of slow-moving dust particles from the lunar surface. Planet. Space Sci. 59, 1446 (2011).
- Z. Sternovsky, E. Grün, K. Drake, **J. Xie**, M. Horanyi, R. Srama, S. Kempf, F. Postberg, A. Mocker, S. Auer, H. Krüger, Novel Instrument for Dust Astronomy: Dust Telescope. Aerospace Conference, 2011 IEEE.

A.2 Papers in Review

- **J. Xie**, Z. Sternovsky, S. Auer, K. Drake, E. Grün, M. Horanyi, H. Le, and R. Srama. Laboratory testing and data analysis of the Electrostatic Lunar Dust Analyzer (ELDA) instrument. Planet. Space Sci.